UNIVERSITY OF TWENTE.

Design, Fabrication and Characterization of an Electrochemical Microfluidic Chip for Drug Screening

Master Thesis Electrical Engineering

Liwei Ma
S1283642

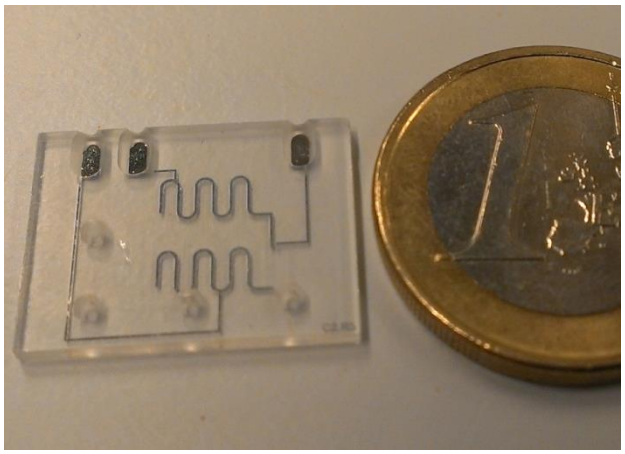

BIOS Lab-on-a-Chip Group

Faculty of Electrical Engineering, Mathematics and Computer Science

Members of the committee:

Dr. ir. W. Olthuis

Dr. ir. M. Odijk

Ir. F. T. G. van den Brink

Prof. dr. ir. A. van den Berg

Dr. ir. R. Tiggelaar

BIOS Lab on a Chip group

September 2014

Acknowledgement

After eight months (January—September 2014) of work in BIOS group, my master thesis project comes to the very end. During this period of time, I have a really good time working in the group. I always find interesting things to do on my project. I enjoy the moment when I finished the design of the chip and made them in the cleanroom by my hand. The feeling of have an idea and make it come true always make me excited. However, the results will never turn so well without the kindly help and encouragement of the following people.

I am very appreciate of Dr. Wouter Olthuis for giving me the opportunity to work on this interesting topic in which I experienced all the challenging phases as a researcher and an engineer. I enjoy every meeting and discussion we had during the project in which I learned how to do research in a systematical manner and tackle the detailed problems. I also learned a lot of knowledge about electrochemistry.

I am very grateful to Dr. Mathieu Odijk who gives me a lot of theoretical guidance on the design of this electrochemical microfluidic chip, as well as many helpful methods to conduct the experiments and interpret the measurements. The design of these nice chips will never accomplished without all the super ideas inspired by him. Moreover, the comments and suggestions he made on the report and the illustration graphs all made the results of my work nicely presented and readable. Especially thankful to that when he is far away in US and has a very busy schedule, he still has been working on revising my report and giving me guidance on the work.

Many thanks to my daily supervisor Floris van den Brink who is very patient to me during the whole period of my work. He guided me on almost all the work I did during the eight months including: how to draw chip layout, how to use simulation software, how to work in the cleanroom, how to conduct the experiments and use the measurement setups, as well as revising on my report. I am not a very careful person. Sometimes I made mistakes and mess it up, he helps me to find the problems and help me to do the work again. Thanks a lot for the careful revising he made on my report, from reshaping the structure to finding very tiny grammar mistakes.

I am also very grateful to Johan Bomer who help me a lot in making the cleanroom process flow and guide me to do many cleanroom work, as well as help me to solve many problems I met in the fabrication of the chips. Without his help, I would have made a lot of mistakes and would not finish the chip fabrication in a very efficient way.

I would like to thank all other committee members Prof. Dr. Albert van den Berg, the chairman of BIOS group, and Dr. Roald Tiggelaar from Mesoscale Chemical Systems group for reading my master thesis and giving me nice suggestions.

I would also like to thank all the members in BIOS group who are always very kind and helpful to me. Besides the hardworking experience in the group, all the leisure activities, barbecue, drinking, cakes, dinners will be a good memory of me.

Special thanks to all my friends I met in Enschede. I had a lot of good time during the past two years with your company. No matter what difficulties I face in my life, you are always there to give me a hand.

Finally, I would like to thank my beloved parents who are always there to support and encourage me even thousands kilometers away in China. I feel myself so lucky because you are always proud of every small achievement I made, and respect every choice I made.

Liwei Ma

September, 2014

Summary

The goal of this project is to design an electrochemical microfluidic chip, fabricate the chip which integrated either with platinum electrode or boron-doped diamond (BDD) electrodes, as well as characterize the electrochemical conversion efficiency of the chip. The application of this chip is in drug screening. The work is based on the former work of Dr. M Odijk and F. T.G van den Brink.

A short introduction of the research goals and the application of the project, as well the outline of the thesis are given in chapter 1. In chapter 2, the basic theory about electrochemistry and some common used measurement techniques are introduced, followed by the fundamentals in microfluidics and a comparison of different kinds of micromixers. The electrode materials – platinum and boron-doped diamond (BDD) – are introduced and compared at last.

With the presented theory, the electrochemical microfluidic chip is designed which consists of an electrochemical flow cell for mimicking phase I drug metabolism, a 3D split-recombine mixer at downstream of the electrochemical cell to study phase II reactions, microfilters to prevent channel blockage, and flow resistors to maintain equal flow speed of the working electrode and the counter electrode in chapter 3. The electrochemical flow cell is designed in three different manners with frit channel system of different geometry connecting the working electrode and the counter electrode. The performance of the 3D split-recombine mixer is simulated in COMSOL Multiphysics.

In chapter 4, the fabrication process of platinum and BDD chips are described, followed by a introduction of the measurement setups and protocols used in the electrochemical measurement and UV/vis conversion efficiency measurements.

In chapter 5, the fabrication results are presented and analyzed, compared with the design of the chip. In the following part, the electrochemical measurements and conversion efficiency results of the electrochemical cell in three different manners are presented and compared with each other, as well as with the design in chapter 2. A brief summary of the performance of the mixer in fluorescence microscopy measurements did by Linda van der Hout is also given to compare with the simulation results.

At last, all the work did in this project is concluded in chapter 6, with some recommendations for the future research.

Parameters

Table: Parameters used in the report.

Symbol	Description	Dimension	Value
ρ	Fluid density	kg/m^3	1000
μ	Dynamic viscosity	$kg/(s \cdot m)$	
η	viscosity	$Pa \cdot s$	8.9×10^{-4}
$\boldsymbol{v}$	Flow velocity	m/s	
$\boldsymbol{D}$	Diffusion coefficient	m^2/s	4×10^{-11} 6.7×10^{-10}
$\boldsymbol{v_{max}}$	Maximum flow velocity	m/s	
$\boldsymbol{v_x}$	Flow velocity in x direction	m/s	
P	Pressure	Pa	
$\boldsymbol{F}$	Body force	N	
Q	Volumetric flow velocity	$\mu L/min$	
$t_{r,min}$	Minimum residence time	sec	
$t_{r,av}$	Average residence time	sec	
$z_{diff,min}$	Minimum diffusion distance	m	
y_{diff}	Diffusion distance	m	
R	Hydrolic resistance	Ω	
R	Electrical resistance	Ω	
c	Concentration	mol/m^3	
A_w	Atomic weight		
J	Current density	A/m^2	
κ	Conductivity	S/m	
l	Channel length	m	
h	Channel height	m	
w	Channel width	m	
$\boldsymbol{u}$	Dynamic velocity		
$\boldsymbol{n}$	Normal vector		
n	Number of electrons		
i	Current	A	
E	Potential	V	
E	Absorbance		
ε	Extinction coefficient		
L	Extinction wavelegnth	nm	

Contents

1. Introduction

1.1 Research goals

The goal of this master project is to design, fabricate and test an electrochemical microfluidic chip. It is part of the PhD project of F.T.G van den Brink which is called 'Miniaturized electrochemical cells for on-line use with liquid chromatography and mass spectrometry for drug screening and proteomics' and is also a continuation of the work of Dr. M.Odijk. The miniaturized electrochemical cell can act as a complementary method of drug metabolic of in vitro test. On the other hand, on-chip electrochemistry integrated with other LC/MS can also be used for protein digestion, separation and analyzing the subsequent peptide by mass spectrometry.

In the work of Dr. M.Odijk, he designed a miniaturized three-electrode electrochemical cell which achieved total conversion of fast reaction ions at high flow rates with small chip volume. In the work of F.T.G van den Brink, he further integrated a microfluidic mixer to the chip to study phase 2 metabolism of drug compounds, as well as a ESI needle to the outlet of the chip for ionization of the molecules before detected in MS. This chip was made of plastic and integrated with carbon electrode. It has dimensions of 6 cm length and 1.5 cm width. The first goal of this project is re-designing the chip based on a much smaller footprint (2 cm $\times$ 1.5 cm). Both the electrodes will be rearranged and the mixer will be redesigned to fit in this small chip. Moreover, a new electrode material--boron-doped diamond (BDD)--is intended for the fabrication of the electrodes because of its prominent characteristics, such as wide potential window, less fouling, high conductivity, high hardness, compared with platinum electrodes.

In summary, three research goals are formulated in this project:

1. Design and simulate an electrochemical microfluidic chip for drug metabolism and proteomics, as well as a micromixer on the chip for controlling the microreactions.
2. Fabricate both chips integrated with platinum electrodes and boron-doped diamond (BDD) electrodes. Investigate possible techniques for BDD cleanroom fabrication.
3. Characterize the conversion efficiency of the chip via electrochemical and optical methods.

1.2 Application of the projects

On-chip electrochemistry mainly has two applications: drug-screening and proteomics.

1) Drug screening

Drug screening is a crucial stage in research of new drug candidates, in which large numbers of molecules are tested with the goal of identifying the most promising candidate. Usually, large amount of promising drug candidates are tested in animal models, but only very few compounds are selected for further clinical trials. The use of animal in drug screening is very time consuming and expensive and often leads to suffering of the used animals[1]. In order to reduce the use of animal test in drug-screening, on-chip electrochemistry stands out as an promising approach to mimic the metabolism of drugs in vitro to reduce animal use in the preclinical part of drug-screening[2].

Drug metabolism usually consists of two phases-phase 1 and phase 2. Phase 1 reaction includes oxidation, reduction or hydrolysis which convert a parent drug to more polar (water soluble) metabolites by unmasking or inserting a polar function group (-OH, -SH,-NH_2), often in the liver[3]. Toxic metabolites may also be generated in phase-1 which is the main concern in drug-screening research. Phase 2 metabolism, also called conjugation reactions, includes glucuronidation, acetylation, and sulfation, which usually involve covalent bonding of the drug or phase 1 metabolite to other polar compounds[4].

An important enzyme family taking part in the drug metabolism process in human body is cytochrome P450 (CYP450) which is responsible for the oxidative metabolism in phase 1 of the majority of the drugs in current clinical use[5, 6]. Usually, liver cell extracts are used in vitro test to mimic the in vivo reaction catalyzed by CYP450[7]. However, the metabolic products may adhere to the cell membrane in the liver cell extracts to make them undetectable. Another in vitro method to induce oxidation reactions is to use direct electrochemical oxidation, in which most oxidation reactions catalyzed by CYP450 are also observed, except for epoxidation, alcohol, and aldehyde oxidation reactions. Direct electrochemical oxidation of drug candidates can be used as a complementary of CYP450 oxidation reaction. The method used in the on-chip electrochemistry cell of this project is direct electrochemistry oxidation which is faster and less costly than the use of liver cell extracts.

2) Proteomics

Proteomics is the science to study the proteins produced by an organism. In proteomics, proteins are cleaved into peptides and subsequently analyzed by mass spectrometry (MS). It relies on specific cleavage of proteins which is usually conducted by enzymatic digestion. Trypsin is the most commonly used enzyme in protein cleavage. Direct electrochemical oxidation of peptides can works as an alternative method for protein cleavage. It allows specific cleavage of the peptide bonds next to tyrosine or tryptophan residues[8].Direct electrochemical cleavage will increase the speed of analysis and can be coupled on-line to a liquid chromatography(LC)-MS system[9].

1.3 Thesis outline

In the following chapters, the works done for this project will be discussed in detail. In chapter 2, relevant theory on electrochemistry and microfluidics, as well as the properties of boron-doped diamond as electrode material will be introduced. In chapter 3, the design and simulation of different components on the electrochemical microfluidic chip is discussed. The experimental procedure of chip fabrication and measurement set up and protocol for characterizing the electrochemical cell and mixer are described in chapter 4. The result of the fabrication process and measurements will be presented in chapter 5. Conclusion and recommendation for future works will be discussed in chapter 6.

2. Theory

In this chapter theory related to the design of the electrochemical microfluidic chip will be introduced. First, some fundamentals of electrochemistry which is considered in designing the electrochemical cell are explained. Different measurement techniques which will be used in the experimentation are discussed. Then the basic theory on microfluidics is introduced for the design of a micromixer on chip. At last, properties of platinum and boron-doped diamond which will be used as the electrode materials are discussed.

2.1 Fundamentals of electrochemistry

Electrochemistry is a branch of chemistry which studies the interrelation of electrical and chemical effects. Electric current pass through a chemical solution can cause chemical changes while the chemical reactions produce electrical energy on the other hand. Electrochemistry has a wide range of applications including electroanalytical sensors, electroplating of metals, waste water treatment, etc. It is also an important tool to electrochemically oxidize the drug and cleavage proteins which are main concern of this project. In the following subchapters, the basic concepts and principles in electrochemistry will be briefly introduced.

2.1.1 Electrochemical cell and reactions

A typical electrochemical cell with three electrodes is shown in Figure 2-1. A working electrode (WE), a counter electrode (CE) and a reference electrode (RE) are immersed in a solution containing ions (electrolyte). The three electrodes are connected via electro wiring to a potentiostat which applies voltage between the working electrode and the reference electrode while measuring the current flow between the working electrode and the counter electrode.

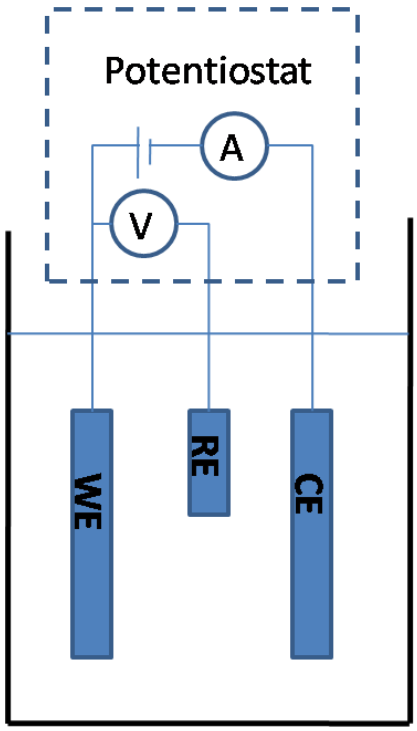

Figure 2-1: Scheme of a three- electrode electrochemical system.

Two half-reactions take place at the surface of the working electrode and the counter electrode which make up of the overall chemical reaction in the cell. The two opposite half-reactions in which ions in the electrolyte donate or accept electrons are called oxidation reaction and reduction reaction, respectively. The half-reactions at the surfaces of the electrodes can be denoted by equation:

$$O + n \cdot e^{-} \rightleftarrows R \qquad (1)$$

Whether an oxidation or reduction reaction can take place at the electrode-electrolyte interface is determined by the relative energy of the electrons within the working electrode compared with the energy of the ion in the electrolyte. By controlling the potential of the working electrode, the reaction at the surface of the electrode can be controlled as shown in Figure2-2. For instance, when more negative potentials are applied to the working electrode, the energy of the electron inside the working electrode is raised ($W = q \cdot V$). If the energy reach a level higher than the vacant electronic states on ions in the electrolyte, a flow of electrons from electrodes to solution will occur which is the reduction reaction. On the other hand, the energy of the electrons in the working electrode can be lowered by imposing a more positive potential. At certain point, electrons on ions in the electrolyte will transfer to the electrode when the energy level of electrons in the working electrode is lower than the occupied electronic states on ions.

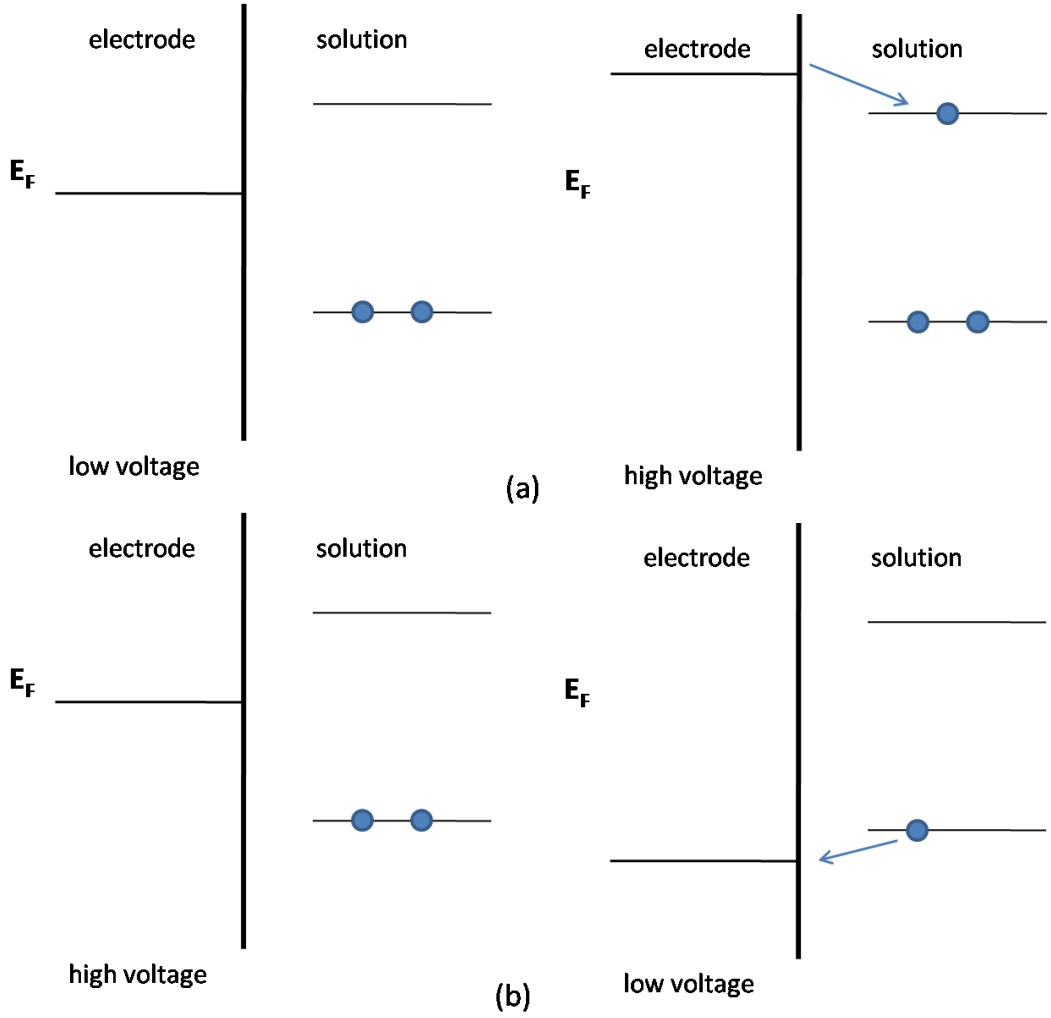

Figure 2-2: Representation of (a) reduction and (b) oxidation process of a species.

2.1.2 Faradaic processes at the electrodes

The reactions discussed above, in which charges are transferred across the metal-solution interface is called Faradaic processes since such reactions are governed by Faraday's law. Electron transfer at the interface causes oxidation or reduction to occur. Either oxidation or reduction reactions at the electrodes are composed of a series of steps. The current in the electrochemical cell (or electrode reaction rate) is governed by four processes in general (Figure 2-3):

a. Electron transfer at the electrode surface.
b. Mass transfer of the species from bulk solution to the electrode surface.
c. Chemical reactions preceding or following the electron transfer (e.g. protonation, dimerization, catalytic decomposition).
d. Adsorption, desorption or crystallization at electrode surface.

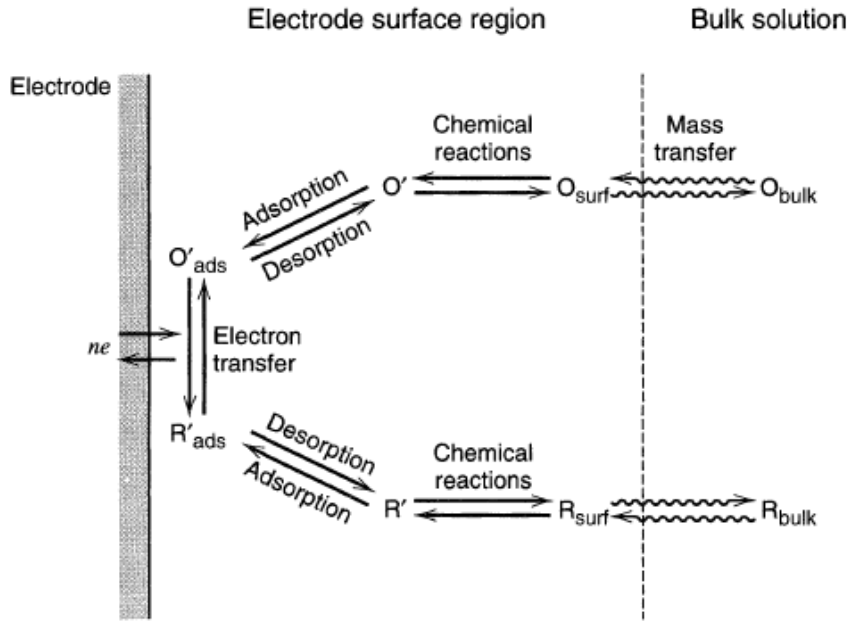

Figure 2-3: Different steps of a typical electrochemical reaction[10].

In most cases, the slowest step in an electrochemical reaction determines the overall reaction rate. Not all of the above steps involves in an electrochemical reactions. Usually only mass transport and charge transfer are involved in a simple reaction.

2.1.3 Kinetics of electron transfer

For electron transfer reactions, the current flowing in either reductive or oxidative steps can be described by the following expressions[11]:

$$i_O = nFAk_{ox}c_R \quad (2)$$

$$i_R = -nFAk_{red}c_O \quad (3)$$

Where n is the number of electrons involved in the redox reaction, A is the electrode area, F is Faraday's constant, c_R and c_O are the surface concentrations of reductive reactant and oxidative reactant, the rate constant of the electron transfer of oxidation and reduction are k_{ox} and k_{red} ,

respectively. The rate constant defines the rate at which the reaction will take place, and can be described by:

$$k_{ox} = k_s \cdot e^{-\alpha \cdot F \cdot (E_{appl} - E^0)/(R \cdot T)} \quad (4)$$

$$k_{red} = k_s \cdot e^{(1-\alpha) \cdot F \cdot (E_{appl} - E^0)/(R \cdot T)} \quad (5)$$

In which k_s is the standard rate constant and α the transfer coefficient, R the gas constant, T the temperature, E^0 the formal potential of a redox couple and E_{appl} the applied potential. This equation shows that the rate constant for the electron transfer steps are proportional to the exponential of the applied voltage. Thus, reaction rate at the electrode surface can be changed simply by changing the applied voltage.

Besides the kinetics of the electron transfer which controls the electrochemical reaction, the rate of mass transfer also controls the overall reaction in many circumstances.

2.1.4 Mass transfer

Mass transfer is another crucial step which can affect or even dominate the overall reaction rate in an electrochemical reaction. When the electrode area (A) is fixed, the reaction at the electrode surface will be controlled by the rate constant k and the surface concentration of the reactant (C^{surf}). If the cell has a large rate constant, any reactant close to the interface is immediately converted into products. Then the currents will be controlled by the amount of reactant reaching the interface from the bulk solution. There are three forms of mass transport which can influence an electrochemical reaction: diffusion, convection, and migration.

Diffusion occurs in all solutions and is caused by the concentration gradient of the reactant. Because the conversion only occurs at the surface of the electrode, the reactant concentration at electrode will be lower than that in bulk solution which leads to continuous transport of ions to the electrode. On the other hand, a higher product concentration near the electrode with respect to the bulk solution will facilitate the product to be transported away. Migration refers to the movement of the ions under the influence of an electric field, while convection is caused by stirring or hydrodynamic transport of the medium.

2.1.5 Ohmic drop

As shown in chapter 2.1.1, the working electrode potential is measured with respect to reference electrode. In an electrochemical cell, current flows in electrolyte by the transport of charged ions. Suppose the resistance of the electrolyte between two electrodes is R_{el}, the potential drop on the electrolyte due to this resistance will be:

$$E_{od} = i \cdot R_{el} \quad (6)$$

which is called ohmic drop. Due to this effect, the measured working electrode potential will change as the current changes, which is an undesirable effect and will influence the accuracy of the measurement. Since the ohmic drop changes in time, it is not easy to compensate this effect. Thus, in the design of the electrochemical cell of this chip, some design strategies are used to minimize the effect of ohmic drop. In an electrochemical cell, different types of charge carriers can contribute to the current. The equivalent conductivity κ (Ω/m) is defined by:

$$\kappa = F \sum_{j=1}^{m} |z_j| \cdot \mu_j \cdot C_j \quad (7)$$

Where μ_j is the mobility, z_j the charge and C_j the concentration of the ion j. Thus, the conductance of a fluidic channel with cross-section area A and length l can be calculated by:

$$G = \kappa \frac{A}{l} \quad (8)$$

Accordingly, ohmic drop can be reduced either by increasing the concentration of electrolyte, the cross-sectional area of the channel, or reduce the distance between working electrode and reference electrode.

2.1.6 Measurement techniques

The electrochemical cell is usually connected to an instrument called potentiostat for the measurement. It controls the voltage between the working electrode and reference electrode, then measures the current flow through the cell. A wide variety of measurement methods can be realized with a potentiostat. In this report, only chronoamperometry (CA), cyclic voltammetry (CV), differential pulse voltammetry (DPV), impedance spectroscopy are used in the characterization of the chip performance.

1) Chronoamperometry

In chronoamperometry, the potential of the working electrode is stepped from a value at which no faradaic reaction occurs to a potential at which the faradaic reaction occurs, while the current is measured as a function of time[12]. The measured current is described by the Cottrell equation:

$$i(t) = n \cdot F \cdot A \cdot C \sqrt{\frac{D}{\pi \cdot t}} \quad (9)$$

where C is the concentration of the ion in the bulk solution.This current-time response reflects the change in the concentration gradient near the electrode surface. Due to the depletion of ions at the electrode surface, a high concentration gradient forms between the bulk solution and the surface. The current rises instantaneously after the change in voltage. As the time goes by, this depletion region expands, the concentration gradient drops. Then the current begin to drop as a function of time as consequence. For a short time period (t <50 ms), an additional background charging current is also contributes to the measured current[12]. Illustration of a chronoamperometry measurement is shown in Figure 2-4.

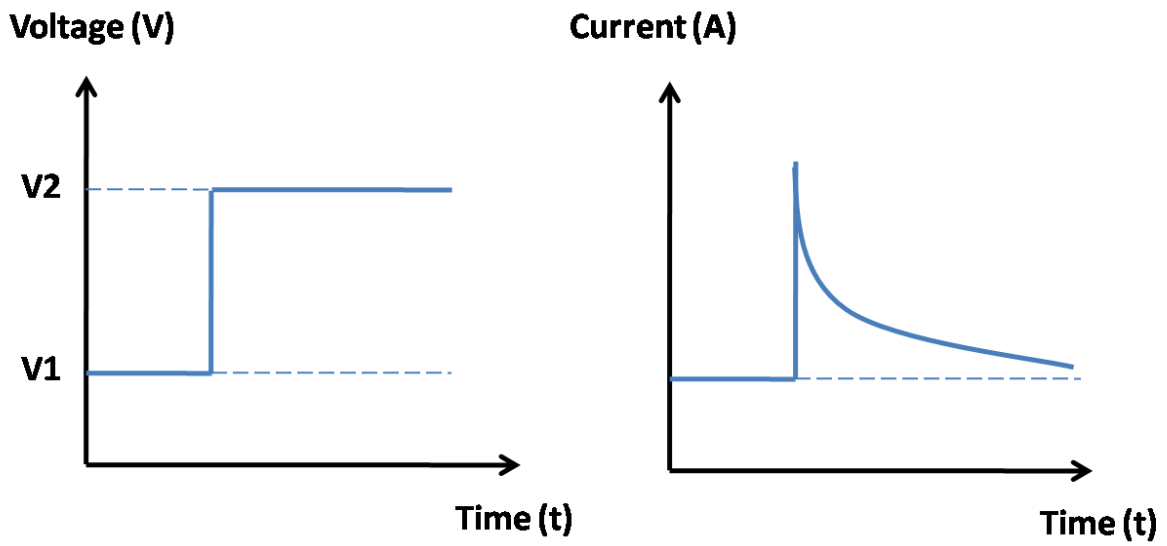

Figure2-4: Scheme of the chronoamperometry measurement result: voltage versus time (left) and current versus voltage (right).

2) Cyclic voltammetry

Unlike chronoamperometry, the voltage is scanned between a lower limit and an upper limit at fixed rate in cyclic voltammetry. When the voltage reaches one limit, the scan is reversed and the voltage is swept back to the other limit, as shown in Figure 2-5 (left). The current is measured as a function of potential which is indicated by Figure 2-5 (right) for a reversible single redox couple.

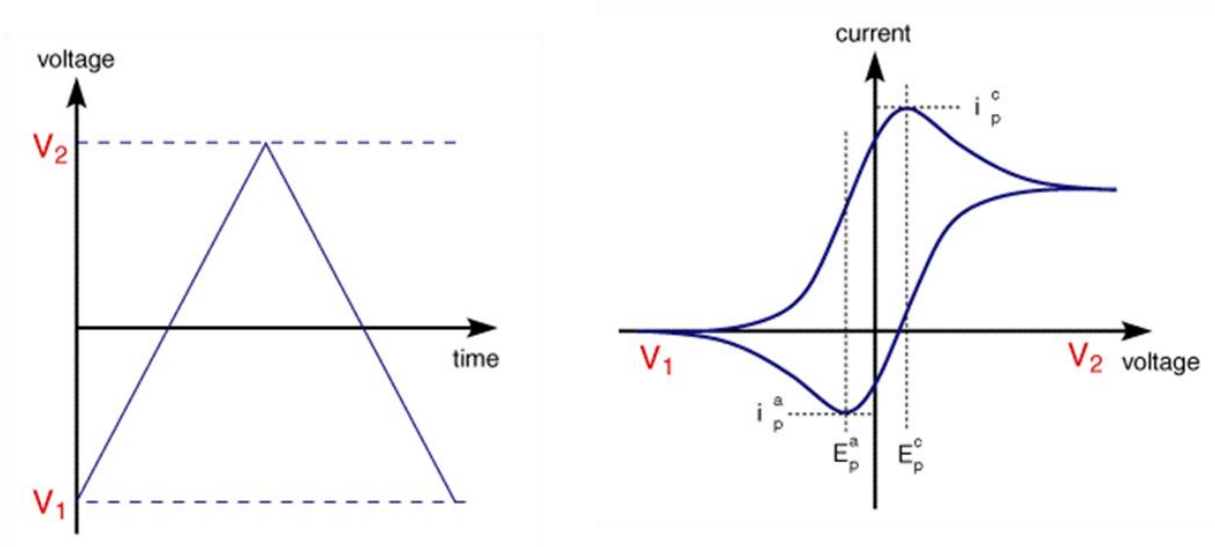

Figure 2-5: Cyclic voltammetry measurement. The left figure shows the voltage as a function of time, while the right figure shows current as a function of voltage [13].

At the start of the scan, when a low voltage is applied, the reaction rates (or current) are determined by the charge transfer between the electrode and the solution. The current will increase as the voltage increases. At a certain point when the overpotential is sufficiently high, an ion depletion layer is formed between the electrode surface and the bulk solution. The reaction rates (or current) are now limited by mass transfer. The current begin to drop because the flux of reactant to the

electrode is not fast enough to satisfy the charges needed for the reaction. After the voltage scan to the high voltage limit, the scan direction starts to reverse. At a certain point, a reduction reaction will happen which is indicated by the negative current in Figure 2-5. Similarly, the reaction rate will first determined by the charge transfer, followed by the depletion of ions at electrode surface. The voltage scan direction then changes to positive again after the voltage reach the lower limit.

3) Differential pulse voltammetry

In differential pulse voltammetry, the potential wave form consists of small pulses of constant amplitude superimposed upon a staircase wave form as shown in Figure 2-6. Two current samples are taken during each pulse period. One is measured immediately before the pulse, the second is taken just before the potential drop. The current difference between the two measurements is plotted as a function of potential.

At beginning of the experiment, when the baseline potential is much more positive than the redox potential, no faradaic reaction in response to the pulse, thus the difference current measured is approximate to zero. At potential around the redox potential, the difference current reaches a maximum, and decreases to zero as the current becomes diffusion rate determined. This technique discriminate faradaic current from capacitive current. The current response of differential pulse voltammetry is a symmetric peak. The height of the current peak is directly related to the concentration of the electroactive species in the solution.

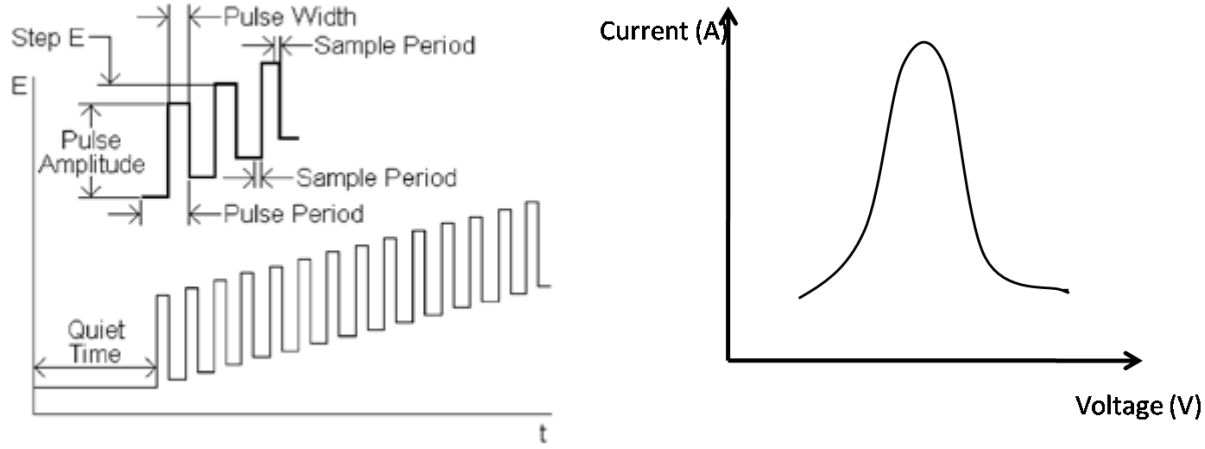

Figure 2-6: Differential pulse voltammetry measurement: applied potential as a function of time (left)[11], measured current as a function of voltage (right).

2.2 Basics of microfluidics

Electrochemistry on chip has a lot of advantages by taking use of microfluidic channels. As mentioned in chapter 2.1.4, mass transfer is one of the rate determine steps in electrochemical reactions. The diameters of the channels are in micrometers which minimizes the diffusion time of the ions, leading to fast reaction and high conversion efficiency of the cell[14]. The small volume of the channel makes it possible to use small amounts of reactants which reduces the cost and the harm to the environment[15]. In addition, the electrochemical microfluidic chip is highly integrated. Different component like sampling, pre-treatment, separation and detection are combined in one microchip. Microelectronic sensors can also be integrated to the chip. Thus, the reaction can be precisely

controlled by the external voltage and flow speed[16]. In this sub-chapter, basic theory about microfluidics will be introduced.

2.2.1 Flow behavior in microfluidic domain

Microfluidic device can be identified by the fact that at least one dimension of the channels is around several hundred micrometers (μm) or less. The volume of the microchannel is usually several nano liters (nL). The flow behavior in microfluidic system differs from the flow behavior in macroscale.

As the length scale of the fluidic channel decreases, surface forces applied to the flow become dominant. Flow behavior in microchannels is commonly characterized by the Reynolds number Re. The Reynolds number is a dimensionless number which represents the relative importance of inertial to viscous dissipation:

$$Re = \frac{d\rho v}{\eta} \quad (10)$$

Where v is the average flow speed, d is the characteristic length scale of the channel, ρ is the density of the liquid, and $\eta$is the dynamic viscosity of the liquid. It is the ratio of the work invested in kinetic energy by accelerating the liquid, and the energy that is continuously dissipated by friction with its surrounding liquid or the wall. For Re much less than 2000, viscous forces dominate, and the flow is laminar. When Re is above 2000, the flow becomes dominated by inertial forces, which produce instability leading to turbulence.

Since the length scale in microchannel is usually small than 500μm, the Reynolds number is typically below 10. The flow in microchannels is laminar as viscous forces dominate in the system. Mixing of parallel streams in the channel only occur by diffusion across the interface of two streams without turbulent mixing.

2.2.2 Mixing principle

Because the flow in microfluidic channels is laminar, mixing of different flow is only by diffusion. The mixing time is determined by the diffusion length:

$$t = \frac{l^2}{2D} \quad (11)$$

Where l is the diffusion length, D is the diffusion coefficiency.On the other hand, rapid mixing is essential in many microfluidic systems for chemical, biological and medical analysis, like drug discovery, sequencing or synthesis of nucleic acids that require mixing of reactants for initiation [17]. Thus, micromixers are often integrated in a microfluidic system or work as stand-alone devices.

Micromixers can be categorized as passive micromixers and active micromixers. Active mixers use external field like electrical field or magnetic field to generate disturbance in the flow. Passive micromixers do not require external energy, only relies on molecular diffusion and chaotic advection. Compared to passive mixers, the structures of active mixers are often complicated and require energy input applied by external fields, such as electrical field and acoustic field. Thus, the more simple and stable passive micromixers are more favorable to be integrated in microfluidic systems. The mixer designed for this project is also a passive mixer which will be discussed in chapter 3.

For laminar streams in microchannels, mixing by diffusion is due to the concentration gradient perpendicular to the flow direction. A typical mixer in which the streams mix by diffusion is a T-shape mixer, as shown in figure 7.In order to decrease the mixing time, the laminar flow in microchannels is usually manipulated by increasing the contact surface between the different fluids and decreasing the diffusion path between them. For the T-shape mixer, it means an extremely long and narrow channel is required. In order to achieve this purpose, the main flow stream can be split into $n$substreams, then join into one stream as laminae which is a parallel lamination micromixer as shown in Figure 2-7. The more substreams it is divided, the faster mixing it can achieve.

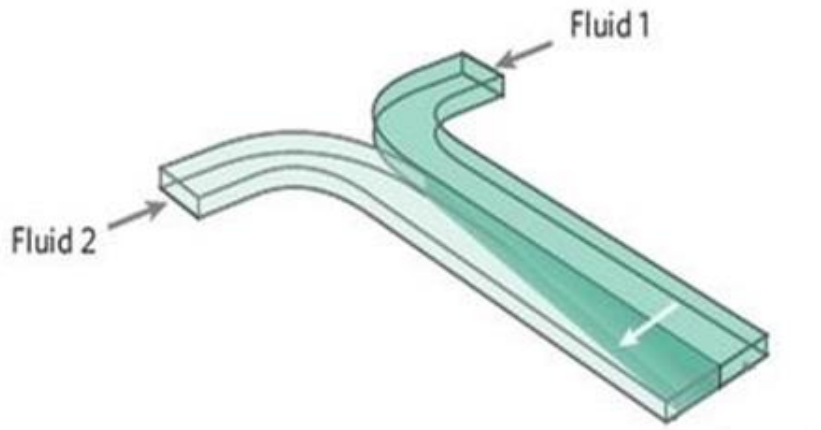

Figure 2-7: Illustration of the working principle of a simple T-shape mixer[18].

Similar to parallel lamination micromixers, another kind of mixer which can reduce the mixing path of the streams is a split-recombine mixer. As shown in Figure 2-8, streams from two inlets are first joined horizontally, then split into two streams again. In the next stage they join together vertically. After n splitting and joining stages, $2n$ laminae layer will be formed which leads to n^2 times faster mixing[17].

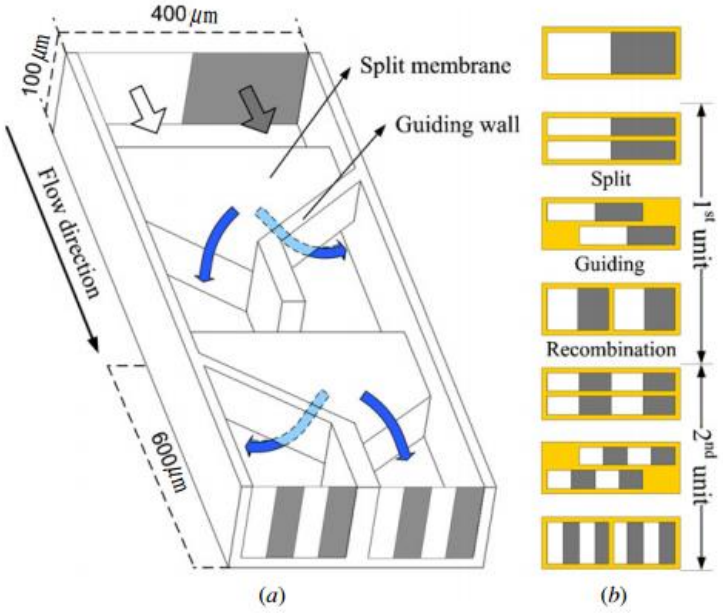

Figure 2-8: Schematic view of a split-recombine mixer(a) and corresponding cross-sectional view of the flow (b)[19].

Besides diffusion, chaotic advection is usually used in micromixers to improve mixing significantly. For a passive mixer, some special geometries are used to generate chaotic advection, like splitting, stretching, folding and breaking of the flow[20].For flows at a high Reynolds number, chaotic advection is obtained by inserting obstacles structures either in the channel (Figure 2-9b)[21] or on the channel wall (Figure 2-9a)[22].Zig-zag microchannel is also used to generate chaotic advection due to the recirculation produced around the corner of the channel (Figure 2-9c). For flows at lower Reynolds number, simple zig-zag micromixer cannot achieve a highly efficient mixing, a 3D serpentine mixing channel can be used as an alternative as shown in Figure 10.

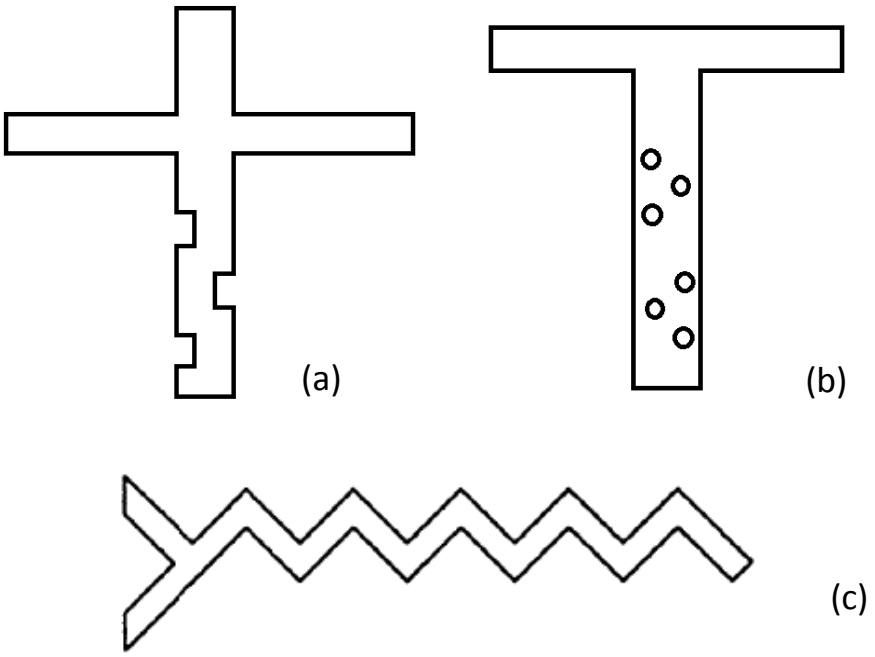

Figure2-9: Planar designs for mixing with chaotic advection at high Reynolds numbers: (a) obstacles in the channel, (b) obstacles on wall, and (c) a zig-zag shaped channel.

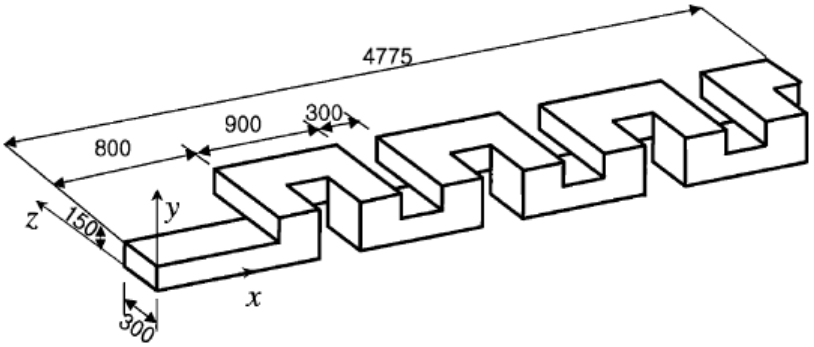

Figure 2-10: Scheme of a three-dimensional serpentine mixer (**μm**)[23].

2.3 Electrode materials

The working electrode is the electrode of interest in an electrochemical cell, because the electron transfers of redox couples occur at the interface between the electrode and the solution. For a good measurement of the targeted reaction behavior in an electrochemical cell, a fast and reproducible charge transfer is favorable. The material of the working electrode is crucial to electrochemical

measurement. Several important criteria are usually considered when selecting the material. First of all, the electrode material should not take part in the chemical reactions in the solution[24]. Secondly, the solvent electrolysis window should be as wide as possible. When the electrode works beyond its potential window, redox reactions with the electrode materials will contribute to the faradaic current which leads to inaccurate measurements. Thirdly, electrode fouling is unwanted because it hampers the direct determination of the reactant and reduce the electrode sensitivity[25]. Other considerations include the cost of the material, the easiness of fabrication, the ease of surface renewal, and toxicity.

Platinum is one of the most commonly used electrode materials because of its electrochemically inertness in most electrolyte and easiness of fabrication. However, the hydrogen adsorbed at the surface of platinum can be reduced to hydrogen gas at negative potentials which obscures the analytical signal of the electrolyte[26].

Diamond has become a promising electrode material because of its extraordinary properties. It has high hardness, high thermal conductivity and high charge carrier mobilities. It is intrinsically an insulator with a band gap of 5.5 eV, but can acquire electrical conductivity by doping of acceptors like boron. The conductivity of boron-doped diamond (BDD) electrodes depends on its doping level. Usually, BDD electrodes have resistance between 5 and 100 $m\Omega$ in the doping level between 500 ppm to 10,000 ppm[27].

Boron-doped diamond electrode has very high overpotential for both oxygen and hydrogen evolution in aqueous electrolytes which leads to the highest potential window(approximately 3.5V) in aqueous electrolyte compared to other commonly used electrode materials, such as platinum, gold, glassy carbon[28, 29]. Cyclic voltammograms of a platinum and a BDD electrode in 0.2 M H_2SO_4 in the region of hydrogen and oxygen evolution are plotted in Figure 2-11. Boron-doped diamond also has other advantages like very low capacitance and low adsorption of contaminant[30].

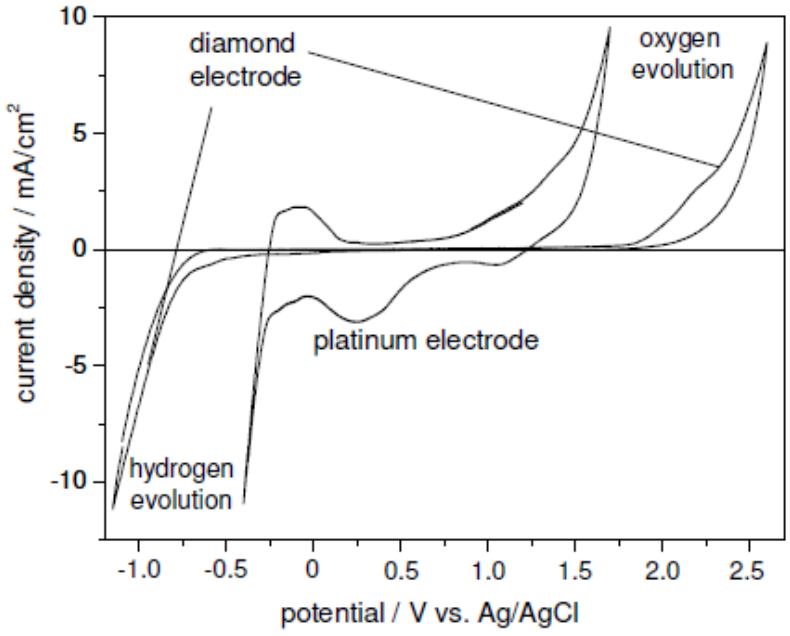

Figure2-11: Cyclic voltammogram of a platinum and a diamond electrode in 0.2 M H_2SO_4, v=100Mv/sec.[31]

The surface termination group of BDD contributes greatly to its physical and chemical properties as electrode. Diamond consists of sp^3 hybridized carbon which means that approximately one carbon atom in a thousand is replaced by an atom of boron. However, there are some sp^2 zones on the surface of BDD which lead to significant fractions of the electrode surface being non-conductive. This will lower the detection limits and sensitivity to target analytes[32].

On the other hand, BDD thin film produced by chemical vapor deposition (CVD) possesses a hydrogen terminated surface which is due to the hydrogen containing atmosphere during the production process. These hydrogen-terminated groups make the surface of BDD electrode hydrophobic and are very stable in air at least for months[28]. The hydrogen-terminated surface can be changed to oxygen-terminated surface which is hydrophilic during anodic oxidation treatment in aqueous electrolytes. Anodic oxidation can also destroy sp^2 carbon impurities on the surface.

3. Design and Simulation

3.1 The chip overview

The goal of designing this miniaturized electrochemical microfluidic chip is to realize both on-chip electrochemical conversion of drugs and protein digestion. The first design consideration is to fit all the required functional components in the fixed dimension of the chip. The dimensions of the chip are defined by the custom-made chip holder which is $2\times1.5cm^2$. The real work area which can fit the fluidic components is even smaller (approximately $1.6\times 1\ cm^2$) because of nanoport through holes and electrical contact pads through holes (Figure 3-1).

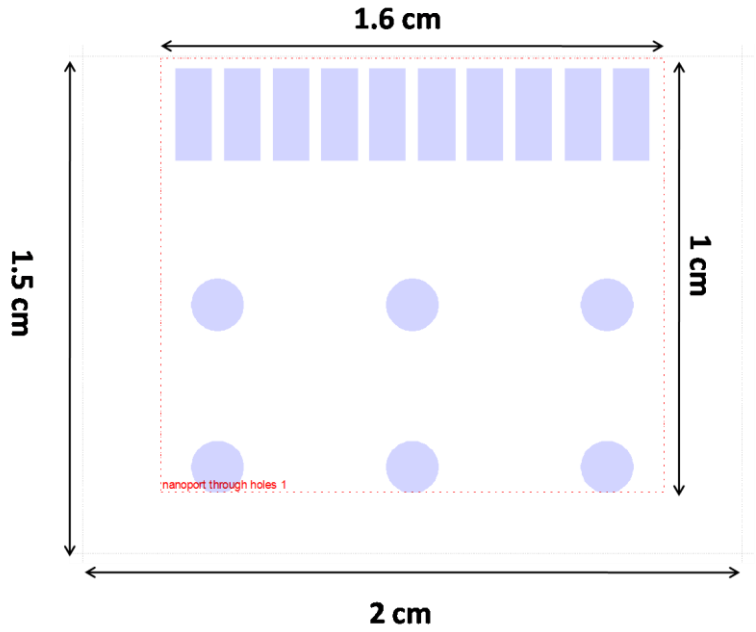

Figure 3-1: Dimensions of the chip in which $\mathbf{2\times1.5\ cm^2}$ is the chip area, $\mathbf{1.6\times1cm^2}$ is the work area defined by nanoport and electrical contact pads through holes.

The chip is intended to mimic both phase I and phase II of *in-vivo* drug metabolism. The microfluidic channels containing the electrodes are used to mimic phase I reactions in which the drugs are oxidized at the liquid-electrode interface. The electrochemical cell contains a three-electrode system. The pseudo-reference electrode is put on the bottom of the inlet channel. Downstream the inlet channel splits into two channels which contain working electrode (WE) and counter electrodes (CE), respectively, on the bottom of the channels. A mixer is integrated downstream of the working electrode channel with a second inlet to add reactants for conjugation reactions.

Other complementary fluidic components are also integrated in the chip for better control of the flow and reactions. Two microfilters consisting of arrays of micropillars are integrated near the channel inlet to prevent the particles and debris from blocking the channels. A flow resistor is added near the channel outlet of the WE channel to ensure an equal flow through both working and counter electrode channels. A frit channel system is designed to connect the WE and CE channels to reduce the ohmic drop between them, as well as to achieve an uniform current density over working

electrode. The overview of the chip and the fluidic components consist the chip are shown in Figure 3-2. All these design elements will be discussed in the following subchapters.

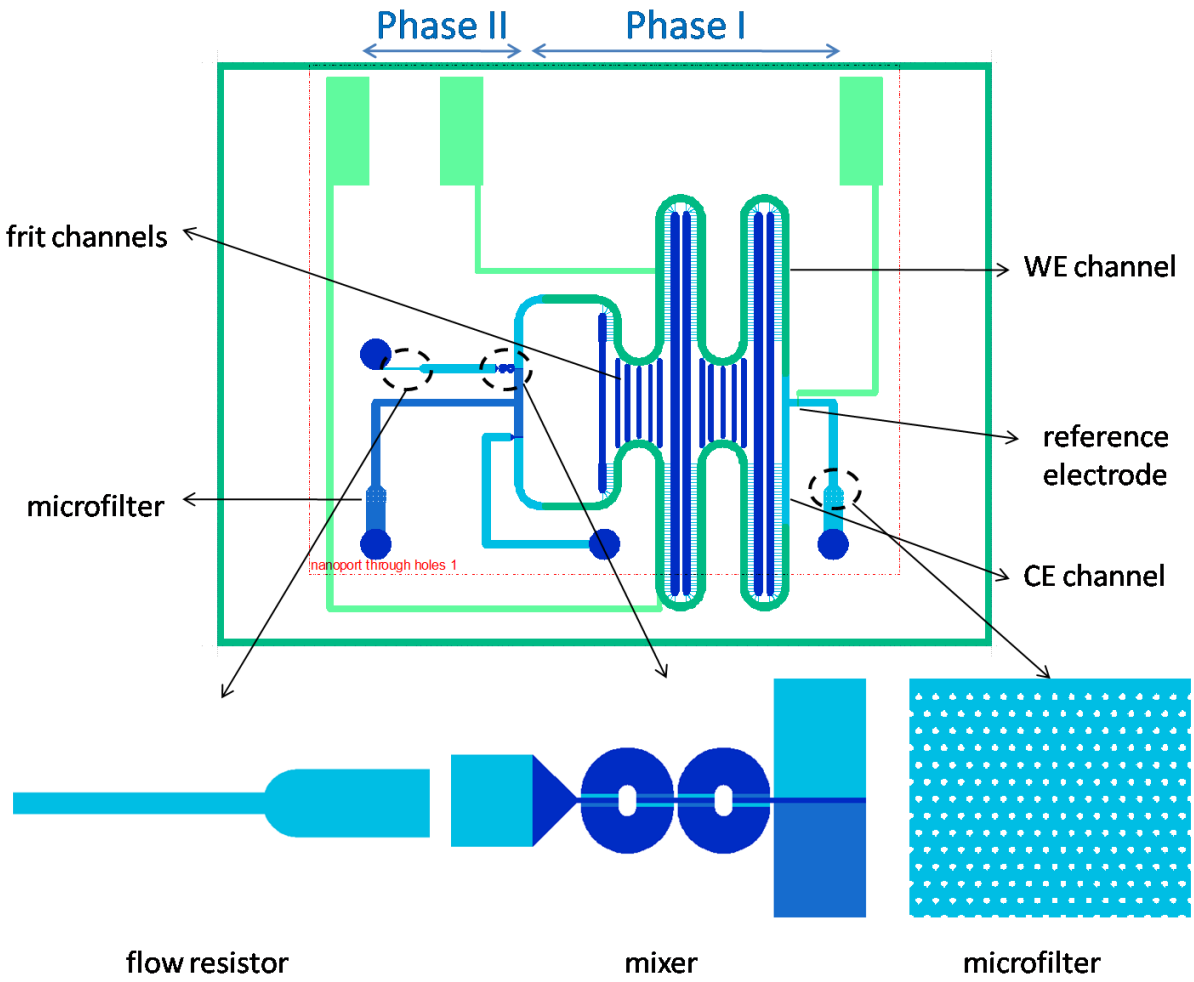

Figure 3-2: Illustration of the overview of the electrochemical microfluidic chip and different components.

3.2 Electrochemical cell

The most critical part of this device is the electrochemical cell containing the three-electrode system where phase I in drug metabolism – oxidation – takes place. The working principle of the electrochemical system was described in Chapter 2. Calculations of the dimensions of the electrochemical cell in this part are based on the PhD thesis of Mathieu Odijk [33]. The designing goal of this part of chip is to realize a total conversion of the inserted chemical species of interest. Two main factors which determine the conversion efficiency of the electrochemical cell are the dimensions of the cell and the volumetric flow velocity.

The Navier-Stokes equation for incompressible flow can be written as[34]:

$$\rho\left(\frac{\partial\vec{v}}{\partial t}+\vec{v}\cdot\nabla\vec{v}\right)=-\nabla P+\mu\nabla^2\vec{v}+\boldsymbol{F} \qquad (12)$$

Where ρ is the fluid density, μ the dynamic viscosity, $\vec{v}$ is the flow velocity, P is the pressure, $\boldsymbol{F}$ is the body forces acting on the fluid. Because of the small channel dimensions (in μm range) and the slow

volume flow velocity (several μL/min), the flow in the channel is assumed to be laminar. In the flow direction of laminar flow where no convective acceleration exists, the Navier-Stokes equation can be simplified as:

$$\mu \frac{\partial^2 v_x(z)}{\partial z^2} = -\nabla P \quad (13)$$

In which v_x is the flow velocity in the flow direction (x) (Figure 3-3).

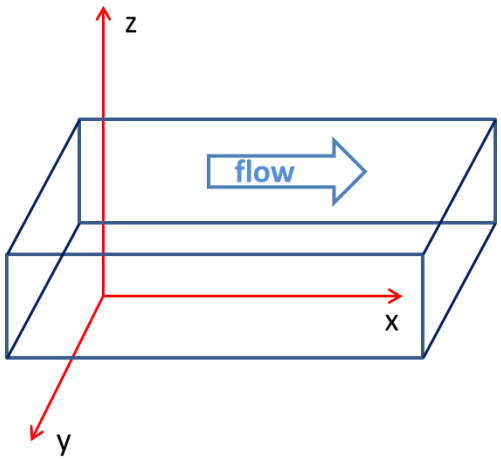

Figure 3-3: The axis system of the channel going to be used in the calculation.

In this design, the electrodes will be incorporated in the bottom of the microchannels. In order to ensure a total conversion of the chemicals, a large working electrode area is preferred. Assuming the length (l) of the working electrode is much larger than the width (w), which is in turn much larger than the height of the microchannel (h). As a result, the velocity flow profile in the flow direction of the channel can be derived as[33, 34]:

$$v_x(z) = v_{max}(1 - 4\frac{z^2}{h^2}) \quad (14)$$

In which v_{max} is the maximum flow velocity in the channel. The volumetric flow velocity (Q) in the channel equals the integral of v_x along the channel height multiplied by the channel width w:

$$Q = w\int_{-h/2}^{h/2} v_x\, dz = \frac{2}{3}whv_{max} \quad (15)$$

Thus, the minimum residence time ($t_{r,min}$) of an ion inside the channel is equal to:

$$t_{r,min} = \frac{l}{v_{max}} = \frac{2whl}{3Q} \quad (16)$$

In order to fully convert the ions flowing through the microchannels, the channel height (h) should be equal to or smaller than the minimum diffusion distance ($z_{diff,min}$) which is the diffusion distance of ions in the z-direction within the minimum residence time. The relation of channel height (h), minimum diffusion distance ($z_{diff,min}$), and minimum residence time ($t_{r,min}$) can be described by the following equation:

$$h \leq z_{diff,min} = \sqrt{2Dt_{r,min}} \quad (17)$$

Where D is the diffusion coefficient. Due to the materials and process used for making the chip, the channel height above working electrode is fixed as 5 μm. Thus, the channel length (l) as a function of channel width (w) and volumetric flow velocity (Q) can be derived from Equation (5) and (6):

$$l \geq \frac{3hQ}{4Dw} \quad \textbf{(18)}$$

Besides the conversion efficiency of the electrochemical cell, the maximum channel pressure the chip can stand is another design consideration. In order to prevent problems with fluidic interconnects and channel breakage, the pressure drop over the EC channel should be smaller than 10 bar. In Equation (7), length l only refers to the length of the channel containing the working electrode. Therefore the pressure difference over this part of channel is considered in the following derivations. The pressure difference over the whole channel is slightly larger.

The hydraulic channel resistance of a rectangular cross-section channel is equal to [34]:

$$R = \frac{P}{Q} = \frac{12\eta l}{wh^3} \quad \textbf{(19)}$$

Thus, the pressure difference (P) over the part of the channel containing the working electrode will be:

$$P = QR = \frac{12\eta lQ}{wh^3} \geq \frac{9\eta Q^2}{Dw^2h^2} \quad \textbf{(20)}$$

The viscosity of the liquid is chosen to be the value of water (η=8.9×10^{-4}Pa · s). A small diffusion coefficient (e.g a protein) is used (D=4×10^{-11}m^2/s) and volume flow velocity of 1 μL/min is used in the calculation. According to Equation (7) and (9), the minimum channel length (l_{min}) containing the working electrode and the corresponding minimum pressure difference (P_{min}) can be calculated. The results are shown in Figure 3-4.

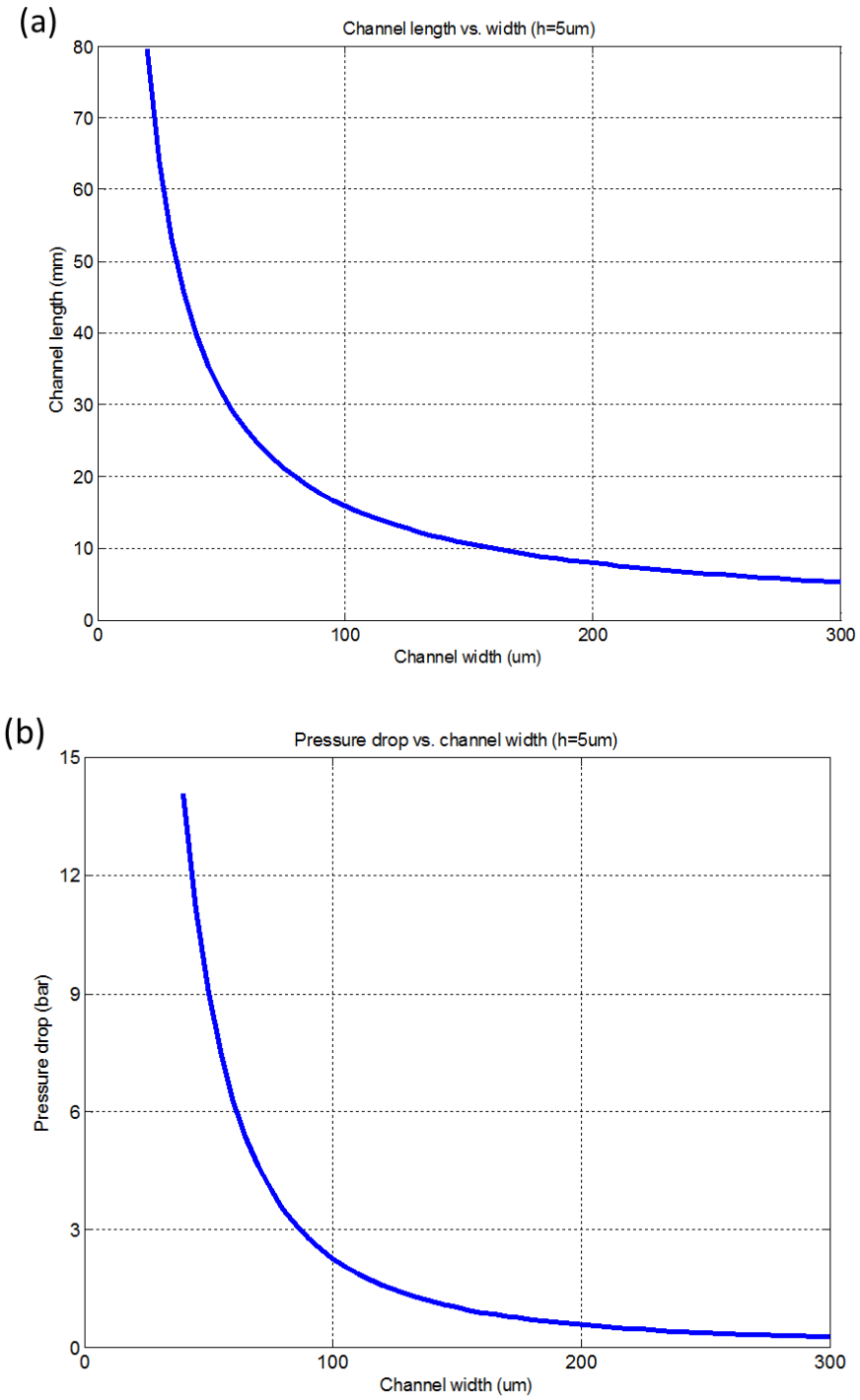

Figure 3-4: Channel length (a) and pressure drop (b) as a function of channel width.

From the plotted graph, l_{min} and P_{min} are decreasing for larger channel widths (Figure 3-4(b)). Considering the dimensions and footprint of the chip holder (work area restricted by through holes), the channel width is chosen as 200 μm. When the volume flow velocity is chosen to be 1 $\mu L/min$, l_{min} is approximately 8 mm according to Figure 3-4(a). The selected length is chosen to be 30 mm which is approximately four times of this minimum length for the critical scenario. Thus, the ions which diffuse four times slower can still be conserved. The pressure difference over the channel part

containing the working electrode is 2.18 bar, which is in the safety range. The maximum volume flow velocity (Q) allowed by the channel is 4 $\mu L/min$ for pressure difference below 10 bar.

Moreover, the average residence time of the ions in the electrochemical cell is also considered. The average residence time can be expressed as following[35]:

$$t_{r,av} = \frac{whl}{Q} \quad (21)$$

When the flow velocity is 1 $\mu L/min$, the average residence time of ions in a channel of 200 μm wide, 5 μm high, and 30 mm is 1.2 seconds. Thus, the drugs flow through the channel can be conserved in seconds.

Considering the geometry of the chip, the electrochemical channels containing working electrode and counter electrode are arranged within the working area in a meander shape in three different patterns as shown in Figure 3-5. The working electrode and counter electrode are put in separate channels to prevent mixing of reaction products generated at both electrodes[2]. Two of the designs contain anti-paralleled WE and CE channels, while the third design has parallel WE and CE channels. The length of the working electrode and counter electrode are comparable in all three designs. The different arrangements of the WE and CE channels are aimed for the characterization of the frit channels, in order to find the most effective design to achieve the lowest resistance between the WE and CE, even current density and ease of fabrication. The pseudo-reference electrode is put in the inlet channel near the working electrode to reduce ohmic drop (Figure 3-6).

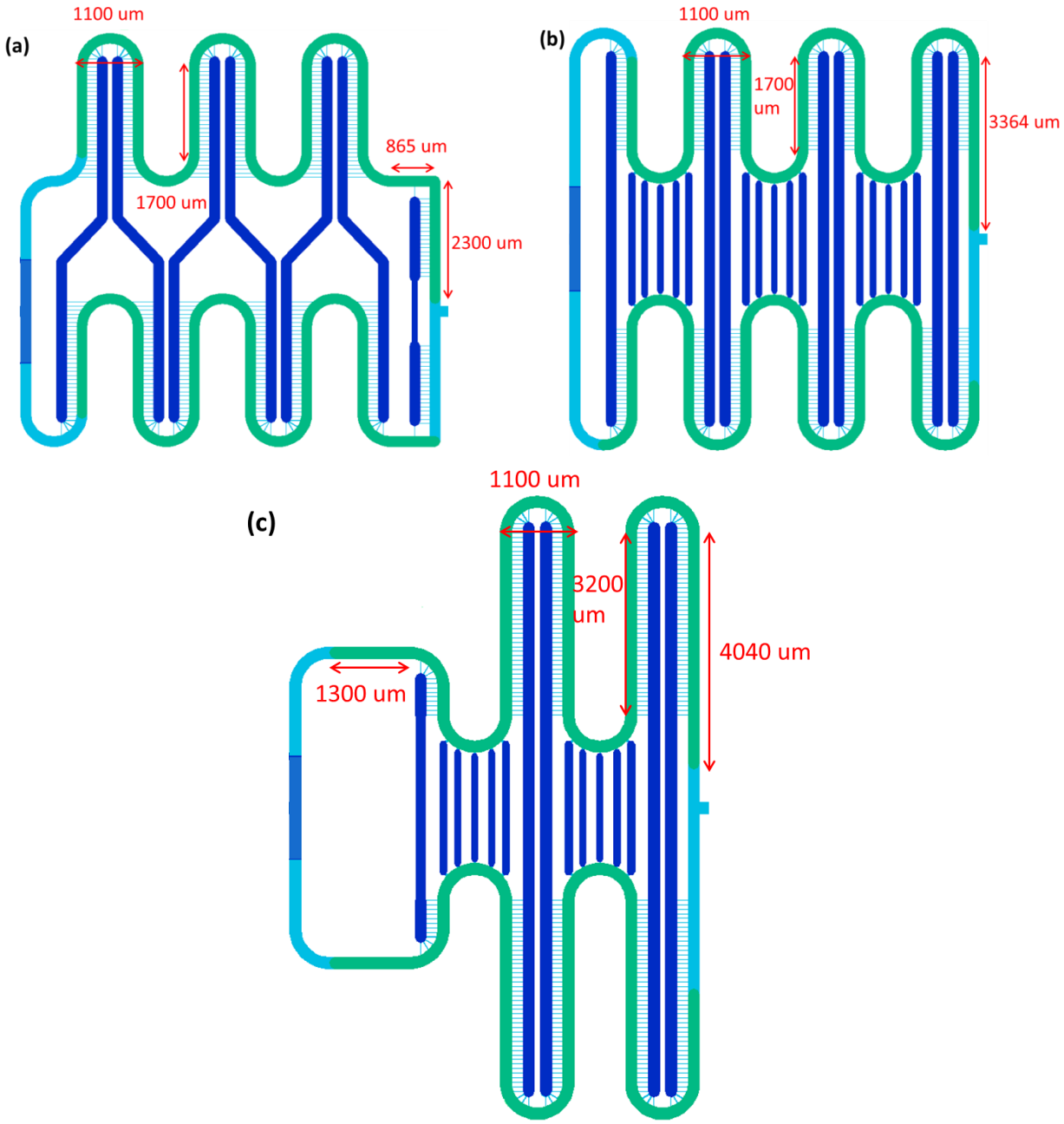

Figure3-5: Geometry of three different electrode arrangements on chip.

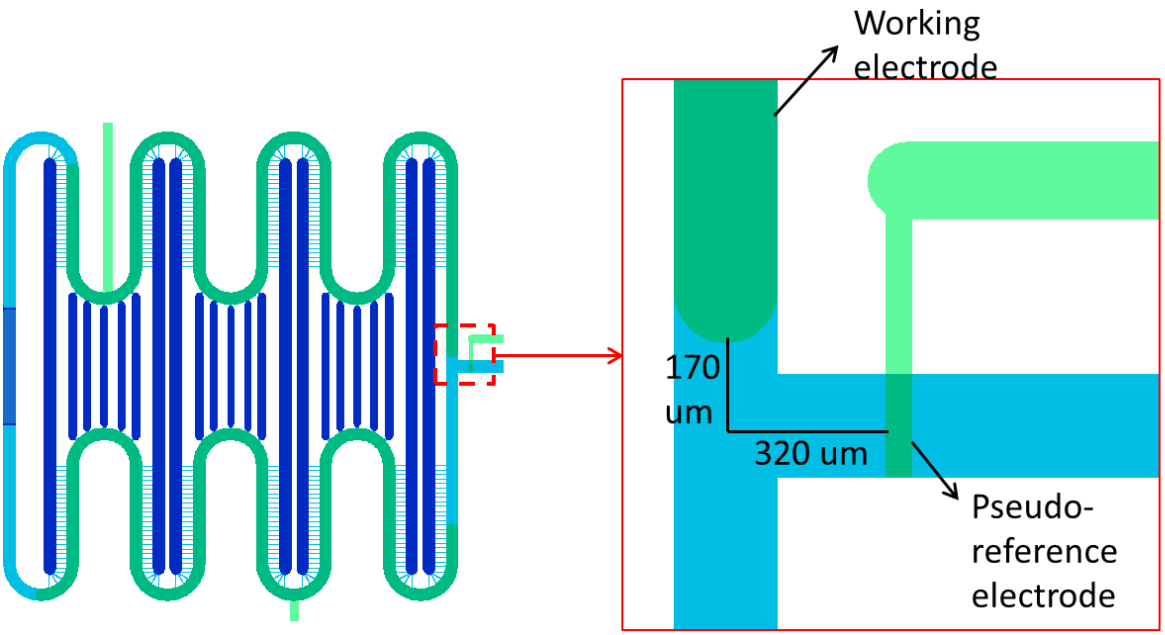

Figure3-6: Scheme of the position of reference electrode and working electrode.

3.3 Mixer

A mixer is designed downstream of the working electrode channel for adding of reactants to imitate phase II reactions in drug metabolism, in which compounds oxidized in the phase I reaction can conjugate to more polar compounds as introduced in chapter 2.

3.3.1 Design considerations

As introduced in chapter 2, due to the small channel diameter and usually low flow speed in microchannels, the fluids in microchannels are laminar flow, where different streams only mix by diffusion. The simplest example is a T-shape mixer as shown in chapter 2, in which two streams meet in one channel and flows side by side in a laminar fashion, while the ions diffuse from high concentration area to low concentration area. In order to reach a total mixing of all the ions in both streams, the ions need to diffuse at least half of the channel width within the minimum residence time ($t_{r,min}$). Thus, the diffusion length (y_{diff}) of the ions in the channel should be equal to or larger than half of the channel width ($w/2$):

$$y_{diff} \geq \frac{w}{2} \qquad (22)$$

Thus, the simplest way to reduce the mixing path is to make a narrow mixing channel and increase the interface of the two streams by increasing channel height (h). On the other hand, the maximum pressure difference in the channel should be considered as in the EC channel design. The total pressure difference (P) should not exceed 10 bar to prevent fluidic leakage.

The T-shape mixer leads to a significant long and narrow capillary to get complete mixing of the two streams, which will increase the pressure difference across the mixer. Due to the extremely small chip area of which the WE and CE channels have already taken most part, the simple T-shape mixer will not work for this chip design.

The chip can be fabricated using two layers for fluidic channels by bonding a SU8 channel layer to a glass channel layer. The detailed fabrication process will be discussed in chapter 4. Thus, two channel layers can be utilized to design a 3D mixer. A split-recombine mixer which takes advantage of two channel layers is designed. The mixer consists of two mixing units in which flow splitting, recombination and rearrangement steps are combined.

3.3.2 Design concept

Figure 3-7 shows the procedure to mix two fluids in the mixer. The two different streams flow separately either in the bottom channel or in the top channel in counter directions before they meet each other. At the interface of the two channel layers, the two streams meet each other and start to mix. The convergent stream then flow into the first mixing unit and are separated vertically to the counter directions. As soon as the convergent flow goes into the mixing unit, the interface of the two fluids will be greatly enlarged. The divided fluids which are in the one-layer height channels ($h = 5\ \mu m$) are then rearranged and are conducted into the two-layer height mixing chamber ($h = 10\ \mu m$) for further mixing. After the two fluids flow through the mixing chamber, they will be reshaped into one-layer channel and recombined at the interface of the two channel layers, flowing out the first mixing unit into the second mixing unit.

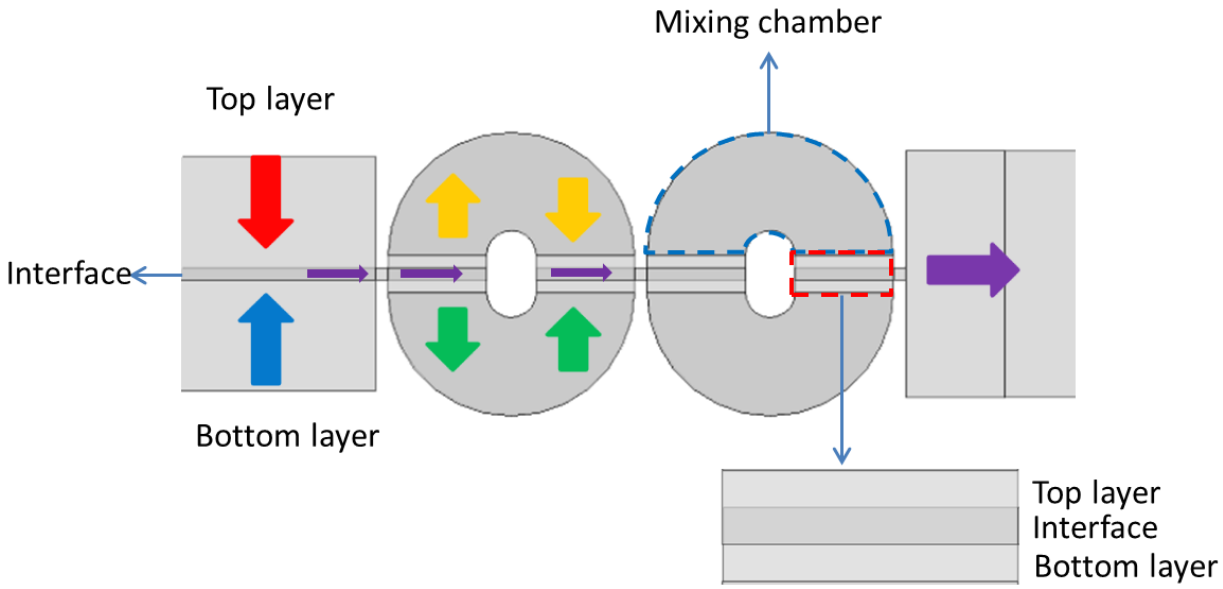

Figure 3-7: Illustration of the mixing procedure in the two-layer split-recombine mixer. Red: Liquid 1; blue: Liquid 2; yellow, green, purple: mixture of Liquid 1 and Liquid 2.

3.3.3 Device modeling and simulation

(1) Define Geometry

The geometry of one mixing unit is shown in Figure 8. The mixer has two inlets and one outlet (Figure 8(a)), and consists of two mixing units. The width of the two inlet channels is $200\mu m$. The width of the interface of the two inlet channels is $10\ \mu m$. The interface of the two inlet channels is connected with the first mixing unit with a convergent cubic which has dimensions of $10\ \mu m \times 10\ \mu m \times 10\ \mu m$. The same convergent cubic also placed at the connect part of the two mixing units and between the

second mixing unit and the outlet of the mixer. Each mixing unit has an entrance of 10 μm $\times$ 10 μm cross-section that splits into two channels of 5 μm $\times$ 80μm cross section and 10 μm length either in the top channel layer or the bottom channel layer in the perpendicular direction of the entrance (Figure 3-8(b)). Each of the channels is connected with a two-layer mixing chamber. At the other end of the two-layer mixing chamber, they are connected to the exit of the unit with a same but mirrored structure as at the entrance.

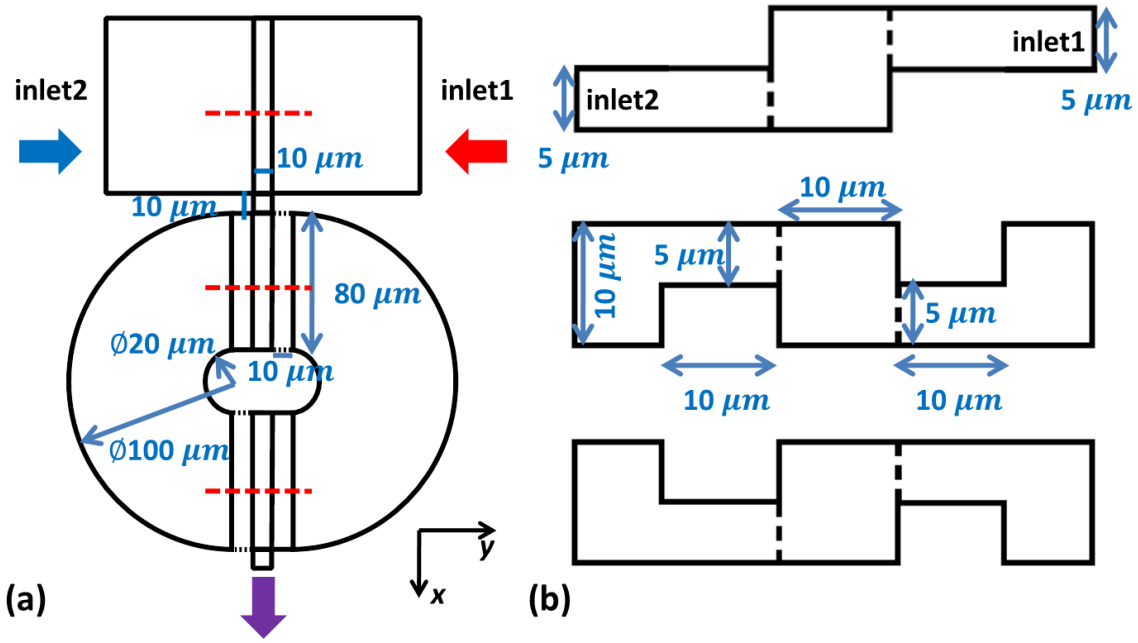

Figure 3-8: Geometry of one mixing unit of the split-recombine mixer.

(2) Domain equations:

In order to study the mixing performance of the mixer, the design is modeled and simulated in the computational fluidic dynamic (CFD) module in the program COMSOL® Multiphysics 4. First, the geometry is defined according to the dimensions in Figure 8.

Then the physical phenomena occurring in the specific geometry of the mixer is defined by domain equations which are a set of differential equations. Formulations that describe the behavior of a three-dimensional incompressible Newtonian fluid are used in the domain definition. The equations governing the system including the Navier-Stokes equations which states the conservation of momentum in a fluid[36]:

$$\rho\left(\frac{\partial \boldsymbol{u}}{\partial t} + \boldsymbol{u}\cdot\nabla\boldsymbol{u}\right) = -\nabla P + \mu\nabla^2\boldsymbol{u} + \boldsymbol{F} \qquad (23)$$

Where $\boldsymbol{u}$ is the flow velocity, ρ is the fluid density, P is the pressure, $\boldsymbol{F}$ represents body forces acting on the fluid.

The fluid in the system should also satisfy the mass continuity equation of incompressible flow which states that, in any steady state process, the rate at which mass enters a system must be equal to the rate at which mass leaves the system[36].

$$\rho \nabla \boldsymbol{u} = 0 \quad (24)$$

On the other hand, the Nernst-Planck equation is used to define the motion of chemical species in the fluid. In steady-state flow, the equation can be simplified in the following form[37].

$$-\nabla \cdot (-D\nabla c + \boldsymbol{u}c) = \frac{\partial c}{\partial t} \quad (25)$$

Where c is the species concentration for mass transfer, D is the diffusion coefficient, $\boldsymbol{u}$ is the dynamic velocity of the flow. $\frac{\partial c}{\partial t}$ represents the reaction rate of the species. $-D\nabla c$ is the diffusive flux, and $\boldsymbol{u}c$ is the convective flux.

The constants used in the simulation are listed in Table 3-1. The diffusion coefficient of GSH is used which is $6.7 \times 10^{-10}\ m^2/s$. If the design of the mixer is efficient under this small diffusion coefficient, the fluid containing ions with larger diffusion coefficient will have better mixing efficiency. The densities of the two fluids are chosen the same as the density of water ($1000 kg/m^3$). The viscosities of the fluids are also chosen the same as the viscosity of water ($8.9\times 10^{-4} Pa \cdot s$). The volume flow velocity (Q) at both inlets are assumed to be 0.5 $\mu L/min$, so that the value at the mixer inlet will be 1 $\mu L/min$. The initial concentration of ions at inlet 1 is assumed to be 1 mol/mL, while at inlet 2 it is assumed to be 0.

Table 3-1: Constants used in the simulation

Constant	Value
D	$6.7 \times 10^{-10}\ m^2/s$
ρ	$1000\ kg/m^3$
η	$8.9 \times 10^{-4}\ Pa \cdot s$
Q	$0.5\ \mu L/min$
c	$1000\ mol/m^3$

(3) Boundary conditions:

Besides defining the fluid properties of the system, the boundary conditions at the interface of flow and the wall of the mixer as well as at the inlets and outlet are also defined in order to solve the domain equations.

a. Fluid flow boundary

Wall boundary condition: The default boundary condition for a stationary solid wall is no slip which means the fluid at the wall is not moving[38].

$$\boldsymbol{u} = 0 \quad (26)$$

Inlet: The normal inflow velocity is specified as

$$\boldsymbol{u} = \boldsymbol{n}U_0 \quad (27)$$

where $\boldsymbol{n}$ is the normal vector perpendicular to the boundary, U_0 is the velocity magnitude.

Outlet: The fluid flow condition at the outlet is assumed to be no viscous stress under given pressure[39]

$$[\mu(\nabla \boldsymbol{u} + (\nabla \boldsymbol{u})^T)] = 0, p = p_0 \quad \textbf{(28)}$$

b. The chemical species transport

Inflow: The concentration of species at one of the inlets is specified to be $c = c_0$, while at the other inlet is $c = 0$.

Wall boundary condition: Boundary conditions along the solid wall are governed by the flux of species from the bulk solution onto the wall. It is assumed no mass flows in or out of this boundary in the simulation.

$$\boldsymbol{n} \cdot (c\boldsymbol{u} - D\nabla c) = 0 \quad \textbf{(29)}$$

Outflow: At outlet, it is assumed no concentration gradient across the boundary:

$$\boldsymbol{n} \cdot \nabla c = 0 \quad \textbf{(30)}$$

(4) Mesh definition:

The domain equations are solved via finite element meshing in COMSOL Multiphysics. The Mesh feature enables the discretization of the geometry model into small units of simple shapes, or elements. Then the software is able to write a set of equations describing the solution to the governing equation. For a 3D geometry, like the mixer design in this report, the geometry will be discretized into free tetrahedral elements. Those meshing elements are used to represent the solution field of the domain equations. The solution is computed at the node points and is interpolated throughout the element to recover the total solution field. As the number of elements in the model increases, they represent the geometry more accurately, the solution will be more accurate, but it will take more computational resources.

According to the geometry of the designed mixer, the most critical size is 5 μm which is the height of one channel layer. A finer meshing is conducted before the computation. The maximum element size is the most important parameter. It should be small enough to ensure a sufficient mesh of the critical structures, but not too small to take too much computation time. The maximum element size used in the simulation is 2 μm. The minimum element size is 0.259 μm.

3.3.4 Result and discussion

1) Mixing performance

Two different fluids which possess the same viscosity as water are used in the simulation. Inlet 1 is assumed a species concentration of 0, while Inlet 2 has a species concentration of $1 mol/L$. The performance of the mixer is illustrated qualitatively through the concentration field. Figure 3-9 shows the mixing process via the concentration field on the surface of the mixer along with the cross-sectional views of the concentration profile. The dark blue color of fluid 1 represents concentration 0 in the figure, while the dark red color of fluid 2 represents concentration of 1 mol/L. The green color area in between represents the mixing region. The concentration profile of different cross section planes along the flow are plotted to investigate the mixing performance more quantitatively at

different positions of the mixer. The mixed region defined here is the area with concentrations between 0.4 to 0.6 mol/L which is enclosed by dotted lines on the cross-sections.

As illustrated by Figure 3-9, at the interface of the two fluidic layers, two fluids overlapped vertically and form a diagonal flow profile which is due to the force between the two fluids that rotates the interface. This phenomenon will extent the interface area of the two fluids. At plane 1 ($y = 205\ \mu m$) where two fluids just meet each other and flow into the convergent cubic, the mixed region is only a thin layer of approximately 2 μm along the diagonal. In the downstream when the fluids go into the first mixing unit, it is separated again into two streams. The cross-section is enlarged when the fluids enter the 80 μm wide mixing chamber where the interface of the two fluids are greatly expanded ($x = 15\ \mu m$ and $y = 310\ \mu m$). At the end of the mixing unit, the two streams recombined and form a new diagonal flow profile. When the fluids go into the second convergent cubic ($y = 415\ \mu m$), the mixed region has enlarged to $7\mu m$.

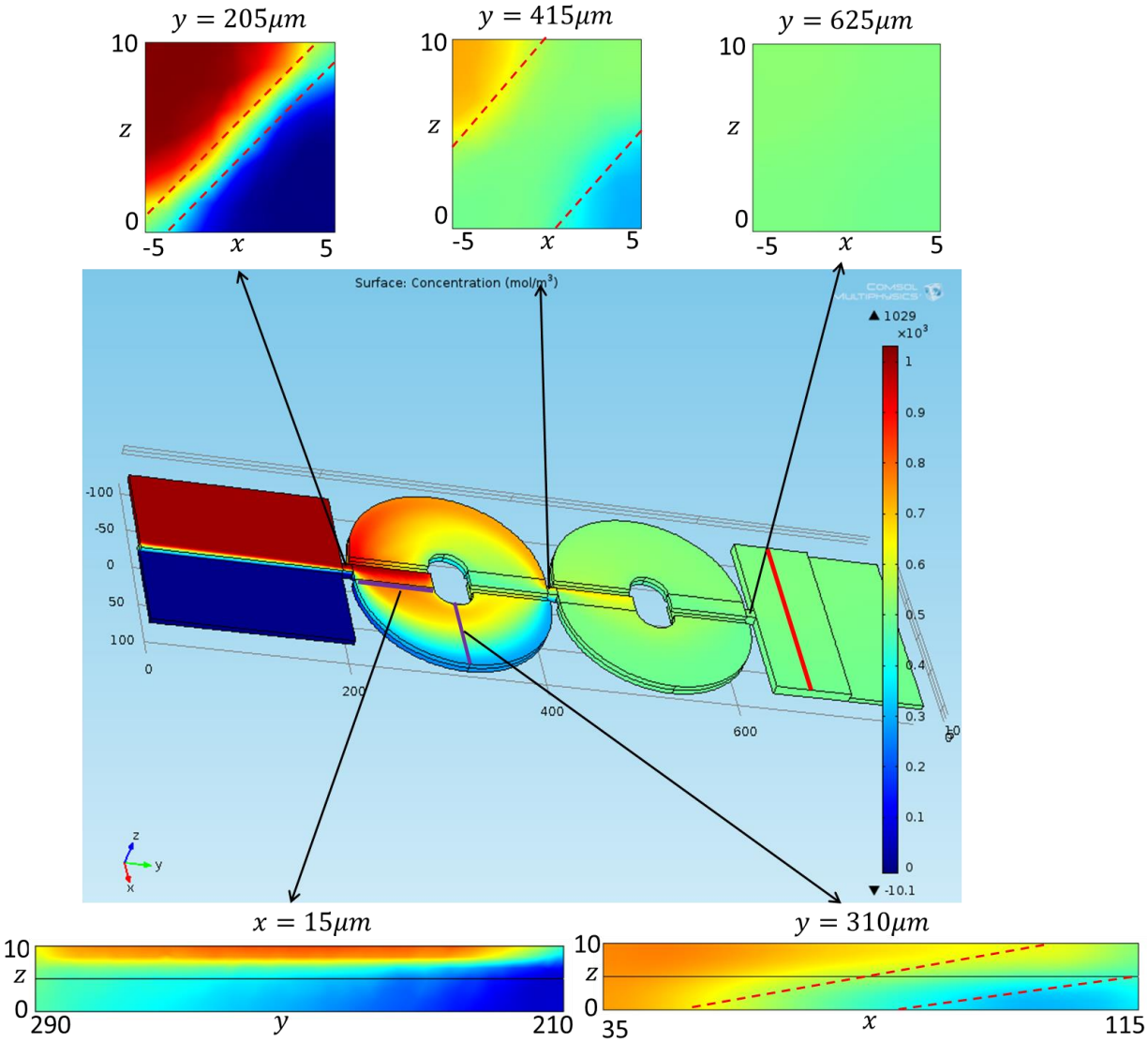

Figure 3-9: Concentration field of the mixer along with cross-sectional views of the concentration field at $\mathbf{y = 205\mu m}$, $\boldsymbol{x = 15\mu m}$, $\boldsymbol{y = 310\mu m}$, $\mathbf{y = 415\mu m}$, and $\boldsymbol{y = 625\mu m}$. Red line: $\boldsymbol{y = 670\ \mu m}$.

To evaluate the performance of the mixer, the mixing efficiency can be calculated by[40]:

$$\text{mixing efficiency} = \left(1 - \frac{\int_0^w |c_i - c_\infty| dx}{\int_0^w |c_0 - c_\infty| dx}\right) \times 100\% \quad (31)$$

Where c_i is the concentration distribution across the transverse direction of a cut plane of the channel, c_∞ is the concentration of complete mixing which is 500 mol/m^3 across the channel width, c_0 is the initial concentration at the inlet.

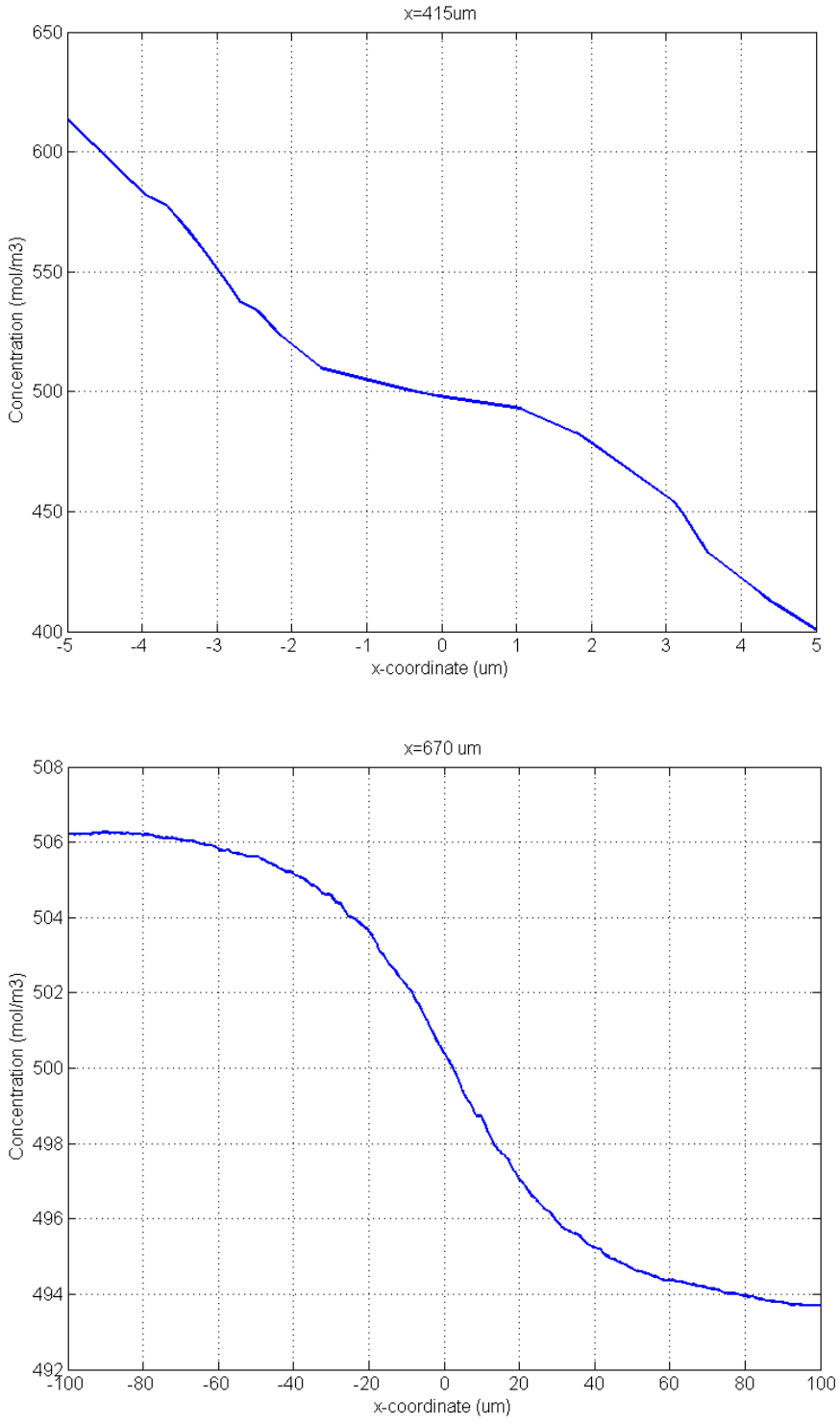

Figure 3-10: Concentration of the species from inlet 1 at different x-coordinates at the cross-section of $\boldsymbol{y = 450\ \mu m}$(top) and $\mathbf{y = 670\mu m}$ (bottom).

Concentrations measured across the cross-sections at $y = 415\ \mu m$ and $y = 670\ \mu m$ are plotted in Figure 3-10. The low resolution in the top figure is due to the limited number of mesh elements. The mixing efficiencies at different cross-sections of the mixer are evaluated using the data from Figure 3-10. The fluids achieved a mixing efficiency of 88.8% after they went through one mixing unit ($y = 415\ \mu m$), while the mixing efficiency is as high as 99% after the flow go through the second mixing unit ($y = 670\ \mu m$).This mixer does effectively reduce the mixing length. After the flow goes through two mixing units, it reaches a almost complete mixing, with a small footprint of only $230\ \mu m \times 470\ \mu m$.

3.4 Frit channels

3.4.1 Electrical domain

In a published paper of M. Odijk, he has already prove that a frit channel system added between WE and CE channels can conduct the current from faradaic reactions that are taking place at the electrodes[2]. In this paper, a group of parallel frit channels of equal dimensions are designed to connect the working electrode channel and the counter electrode. These frit channels offer many parallel paths between the working and the counter electrode which will result in less current flow through the channel between the working electrode and the reference electrode, as a result, reduce the ohmic drop. On the other hand, this frit channel system can help to realize an even distribution of current density from the working electrode to the counter electrode flowing through the electrolyte[2]. According to the theory of electroplating[41], the reaction rate at the surface of the electrode has a relation with the current density J:

$$r = \eta \cdot \frac{A_w \cdot J}{\rho \cdot F \cdot n} \quad (32)$$

Where A_w is the atomic weight of the reactant, n is the number of electrons involved in the reaction, F is Faraday's constant, ρ is the density of the reactant, η is the conversion efficiency. Thus, an even distribution of current density will ensure an equal reaction rate at different positions of the electrode. If the equivalent electrical resistance of the channel is made the same, the current density distribution of each frit channel will be the same. Thus, the parallel frit channels will reduce hot spots on the electrode and increase the part of electrode surface which participate in the reactions.

The meander pattern of the WE and CE channel increases the difficulty of designing the frit channel system. The parallel frit channels with the same dimensions will not achieve equal resistance everywhere on the electrodes in this design. In this new design, the frit channel system consists of main frit channels to reduce the ohmic drop as well as small branch frit channels to realize even flow distribution. In the following report, Design 2 will be used as an example to illustrate the design considerations (Figure 3-11).

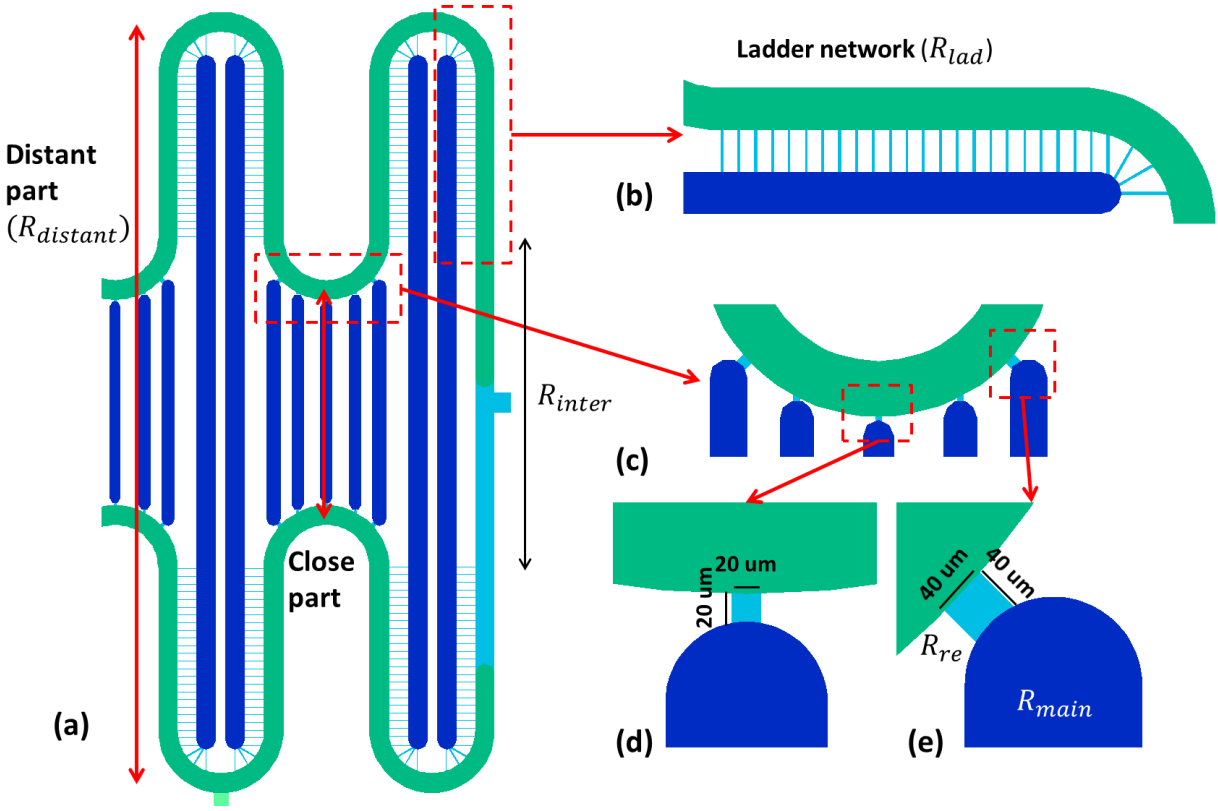

Figure 3-11: Layout of frit channels connecting different part of the electrode channels. Green: electrode channels; Dark blue: main frit channels of 10 **µm** height; Light blue: 5 **µm** high branch frit channels(b) and flow resistor at the connecting part of EC channel and main frit channels (c and d).

The WE channel and the CE channel in Design 2 are anti-parallel placed. In order to greatly reduce the resistance between working electrode and counter electrode, it is good that the main frit channels have a large cross-sectional area. Thus, the height of the main frit channels is 10 μm which makes use of two fluidic layers. A pair of main frit channels of 200 μm width are placed between the most distant part of WE and CE channels. Each of the main frit channels is connected to the electrode channels via many parallel branch frit channels for even current distribution. The potential difference between the working electrode and the counter electrode is equal over the entire electrode length. If the potential difference over the main frit channel is also equal, the current flow through every branch frit channels will be the same. According to the equation of electrical resistance:

$$R = \frac{1}{\kappa}\frac{l}{wh} \qquad (33)$$

where κ is the conductivity. The dimensions of each branch frit channel are calculated to be 5 μm height, 10 μm width, 100 μm length. The interval between two adjacent branch frit channels is 80μm. The equivalent electric circuit of this part of fluidic channel can be derived as a ladder network as shown in Figure 3-12. The resistance of each branch frit channel is one hundred times of the resistance between two frit channels. Thus, the main frit channel is in approximate equal potential, which means $E_1 \approx E_2 \approx E_n$ in Figure 3-12(c).

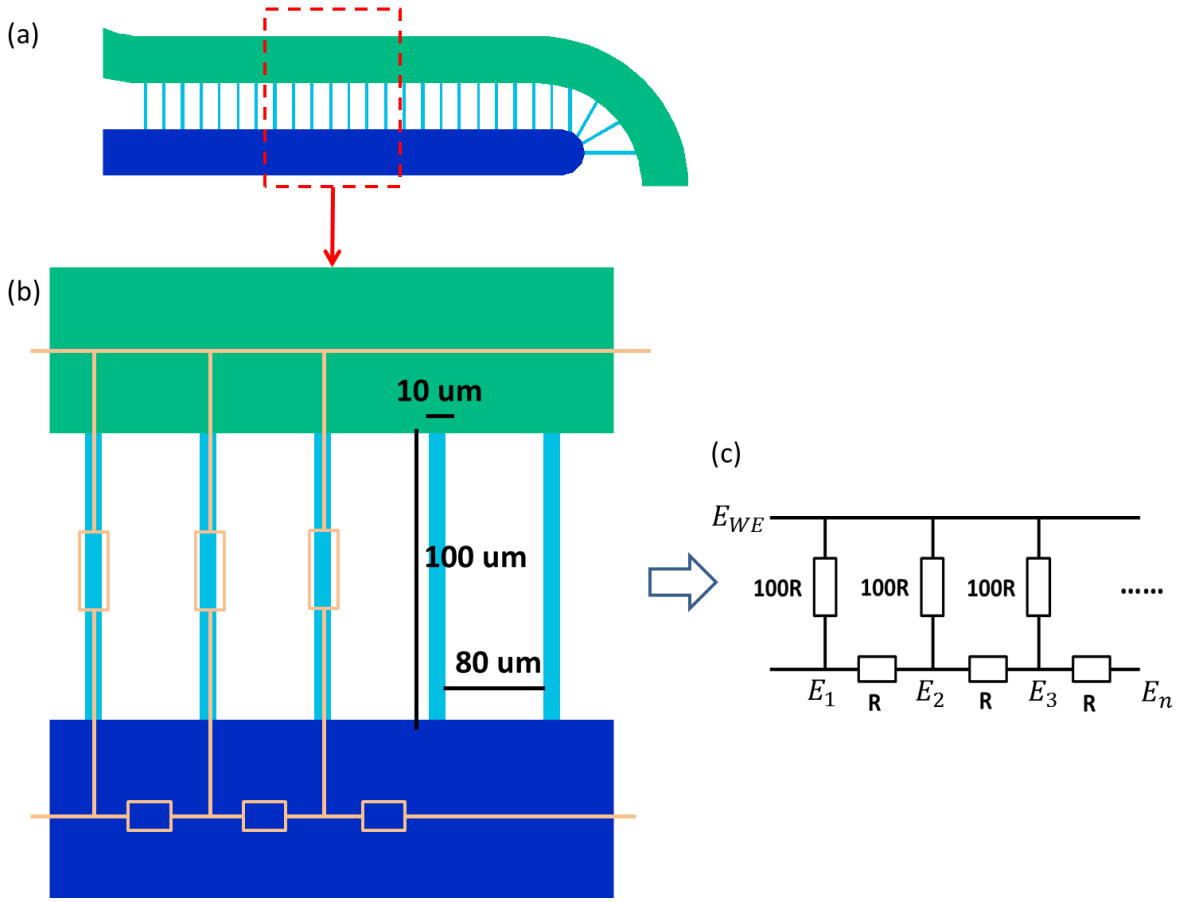

Figure 3-12: Illustration of the ladder frit channel network and its equivalent electric circuit.

The total resistance of the frit channels connecting the most distant part of WE and CE channel is equal to the sum of the resistance of two ladder frit channel networks (R_{la}) and the resistance of the intermediate part of the main frit channel (R_{in}) between the two ladder networks (Figure 3-11).

$$R_{distant} = 2R_{la} + R_{inter} \quad (34)$$

3.4.2 Hydraulic domain

The electric resistance of the frit channels connecting the closest part of the two electrode channels (Figure 3-11) should be equal to the resistance in Equation (34). Since the length of each frit channel is fixed by the geometry of EC channels, the width of each frit channel is adjusted accordingly.

However, the hydraulic resistance of each frit channel should be high enough to prevent a flow between the working electrode channel and the counter electrode channel. According to Equation:

$$R = \frac{12\eta l}{wh^3} \quad (35)$$

The height of the channel plays a significant role in determining the hydraulic resistance. The two layer extremely wide main frit channels cannot directly connect the working electrode channel and the counter electrode channel because of the possible flow between them. For the main frit channel between the distant part of the EC channels, the thin and shallow branch frit channels will act as flow resistor between the main frit channel and the electrode channels. For the frit channel connecting

the closest part of the electrode channels, a one-layer high flow resistor with a small cross-sectional area which will exponentially increase the hydraulic resistance is added at the connecting part of the main frit channel and the electrode channel as shown in Figure 3-11. The electric resistance of each frit channel connecting the closest part of the two electrode channels is equal to the sum of the resistance of the main frit channel (R_{main}) and the resistance of two flow resistors (R_{re}):

$$R_{close} = R_{main} + 2R_{re} \quad (36)$$

The dimension of each flow resistor is either $20\mu m \times 20\mu m \times 5\mu m$ or $40\mu m \times 40\mu m \times 5\mu m$ as shown in Figure 3-11. The resistance of each flow resistor is the same. If $R_{close} = R_{distant}$, the width of each frit channel at the closest part of the two EC channels can be calculated.

The last thing should be considered in designing the frit channels is the ion diffusion time between two electrode channels through the frit channel. The products generated at one electrode diffuse to the other electrode channel during the working time of the chip, which is an undesired effect. Assuming there is no convection in the frit channels, the diffusion time of species as a function of frit channel length is shown in Equation:

$$t = \frac{x^2}{2D} \quad (37)$$

The shortest frit channel of the three chip design is the closest main frit channel on Chip 3 (Figure 3-5(c)) which is 1940 μm, corresponding to a diffusion time of 46 min (D=6.7 × $10^{-10} m^2/s$).Thus, the working time of the chips should be considered in later experiments.

3.5 Other fluidic components

3.5.1 Flow control

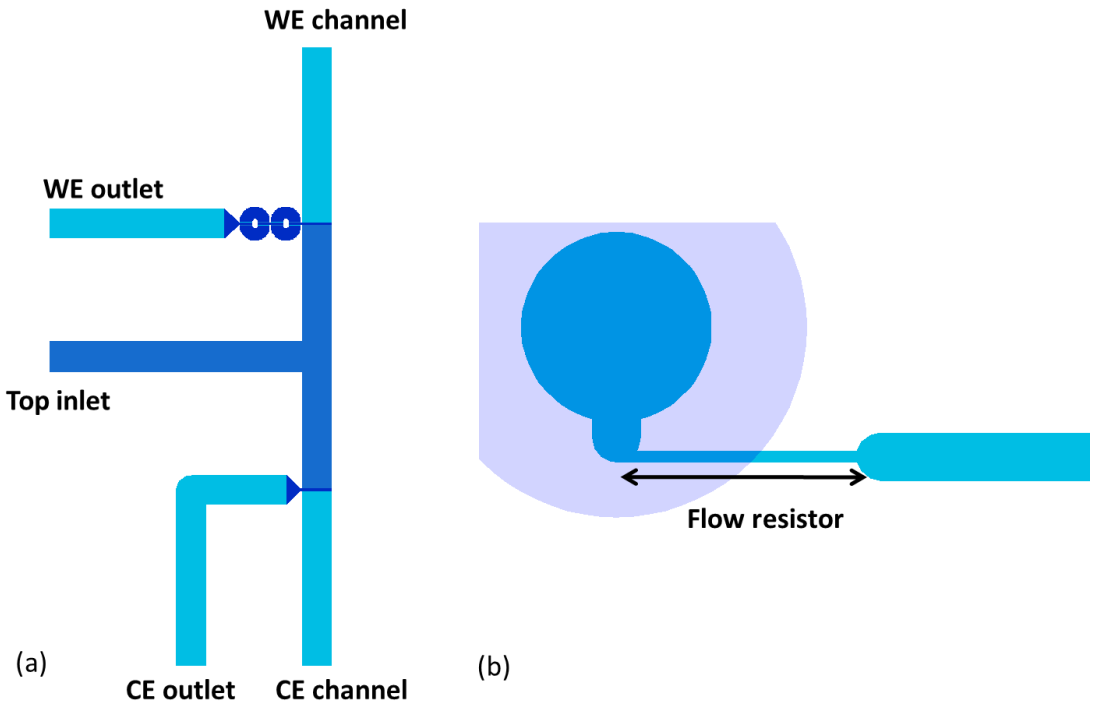

Figure 3-13: Design strategies for controlling the flow rate on chip. A: Top inlet is connected to both WE and CE channels; B: Flow resistor near the outlet of the WE channel used to control the flow velocity.

Equal flow over both working electrode and counter electrode is important for the electrochemical reactions. Two design strategies are used to realize this goal. The inlet at the top fluidic is connected to the downstream of both WE (right before the mixer) and CE channel to ensure equal pressure in the channels (Figure 3-13(a)). Additionally, a flow resistor is added near the outlet of WE channel to achieve equal flow resistance of both channels as shown in Figure 3-13 (b).

3.5.2 Flow filtering

In order to prevent dust and debris flow into the channels and block them, arrays of micropillars are designed near the channel inlet as shown in Figure 3-14. The diameter of each individual pillar, as well as the distance between two adjacent pillars is 5μm which is the most critical dimension in the geometry of the chip.

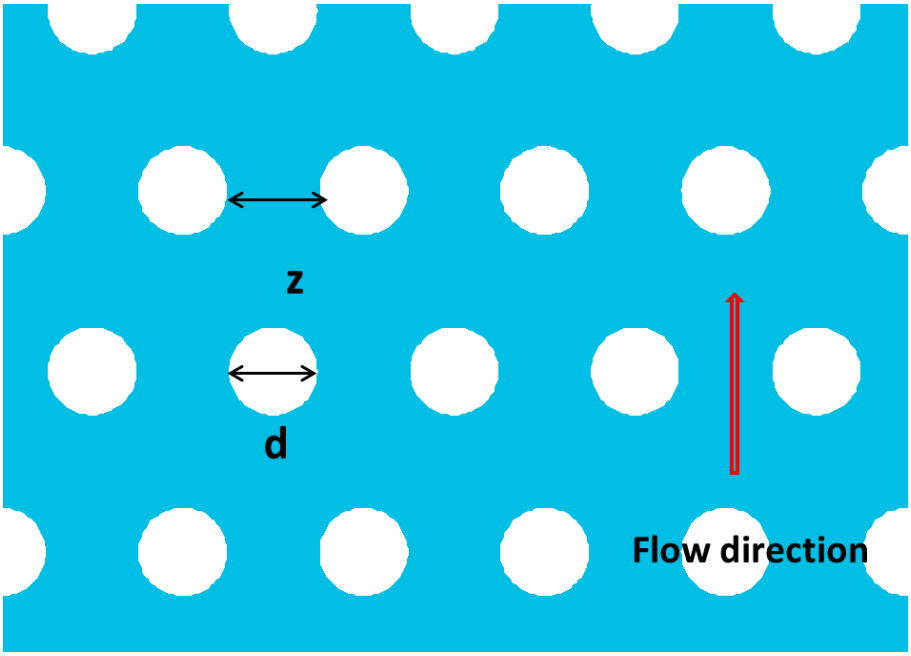

Figure 3-14: Array of micropillars at both channel inlets used to prevent channel blockage.

4. Experimental

In this chapter, the fabrication process of the chips designed in chapter 3 will be presented. Both fabrication processes of the chips are shown: one with integrated platinum electrodes and one with boron-doped diamond electrodes. Secondly, the measurement setup and the protocol of the electrochemical conversion of the chip are introduced. More details on e.g. the characterization of the micromixer and the full process document can be found in the appendix.

4.1 Device fabrication

4.1.1 Process of the chip with platinum electrode

Two glass wafers will be used in fabricating the Pt-electrode chip. An 1100 μm thick, 100 mm diameter glass wafer (Borofloat33) is used to fabricate the top channel layer. The powderblasted holes for electrical contact and fluidic connections are made on the backside of the top wafer. A 550 μm thick, 100 mm diameter glass wafer from the same supplier is used to fabricate the bottom channel layer with platinum (Pt) electrodes. At last, the two wafers will be bond together and diced to make the final device. Detailed fabrication process flow is included in appendix [C]

1) Top wafer

First, the top wafer (Figure 4-1 (a)) is cleaned by 99% HNO_3 to remove potential organic contaminants. Then the wafer is etched in 25% KOH at 75 ℃ for 10 seconds for better adhesion of photoresist. After that, the wafer is put in ultrasonic demi water and cleaned by 99% HNO_3 eventually to remove the residues. Then it is baked at 120 ℃ to remove the moisture on it.

In the next step, hexamethyldisilazane(HMDS) as a primer is spin coated on the front side of the wafer to promote the adhesion of photoresist to the wafer. 3.5 μm thick photoresist (Ti 35 ES, negative) is applied and patterned afterwards (Figure 4-1(b)). The reason to choose this negative photoresist is its high thermal and chemical stability which make it an optimal candidate for plasma etching under harsh conditions[42]. After the first round of UV exposure with mask (Figure 4-1(c)), the wafer is relaxed in room temperature for 20 minutes and goes through a reversal bake round to cross-link and stabilize the exposed area of the photoresist. Then the wafer goes through a flood exposure which is without the mask. It makes the resist which was not exposed in the first exposure step soluble in developer Figure 4-1(d) shows the photoresist pattern after UV exposure and developing.

After finishing the development step, the top channel layer is etched by reactive ion etching (RIE) as shown in Figure 4-1(e). Highly anisotropic structures can be realized by plasma etching because of the directional ion bombardment in the plasma reactor[43].Thus, RIE can realize vertical channel walls and accurate reproduction of the photoresist pattern. The critical dimensions of the mixer (minimum channel width of 10μm) and the micropillars (5 μm diameter and distance between two adjacent pillars) make this etching technique an ideal one. The 5 μm depth channels are etched in 150 sccm He, 20 sccm C_4F_8, and 15 sccm CH_4 gas mixture. C_4F_8 and CH_4 will react with wafer materials and form a passivation layer on the side wall of the channel to prevent further etching of the wall to get anisotropic structure[44]. After RIE, the wafer is put into Piranha solution (H_2SO_4+H_2O_2 (3:1)

volume %) at 95 ℃ for 30 minutes to remove the passivation film and remaining photoresist (Figure 4-1(f)).

The powderblast holes are made at the back side of the wafer. BF410 foil (negative) is used to pattern the powderblast holes image on the wafer. Two layers of foils are applied on the back side of the wafer by a roller (Figure 4-1 (g)). Next, the foils are laminated onto the wafer at 110 ℃ in a laminator. The front side is protected by a layer of dicing foil. After the foils are properly laminated (without bubbles beneath), the backside of the wafer is exposed in UV for 20 seconds (Figure 4-1(h)). After the exposure, the wafer is developed in Na_2CO_3 solution and rinsed afterwards (Figure 4-1(i)). After the development, the wafer is dried and powderblasted with Al_2O_3 particles (Figure 4-1(j)). The foils are removed and the wafer is cleaned in ultrasonic aceton (Figure 4-1(k)).

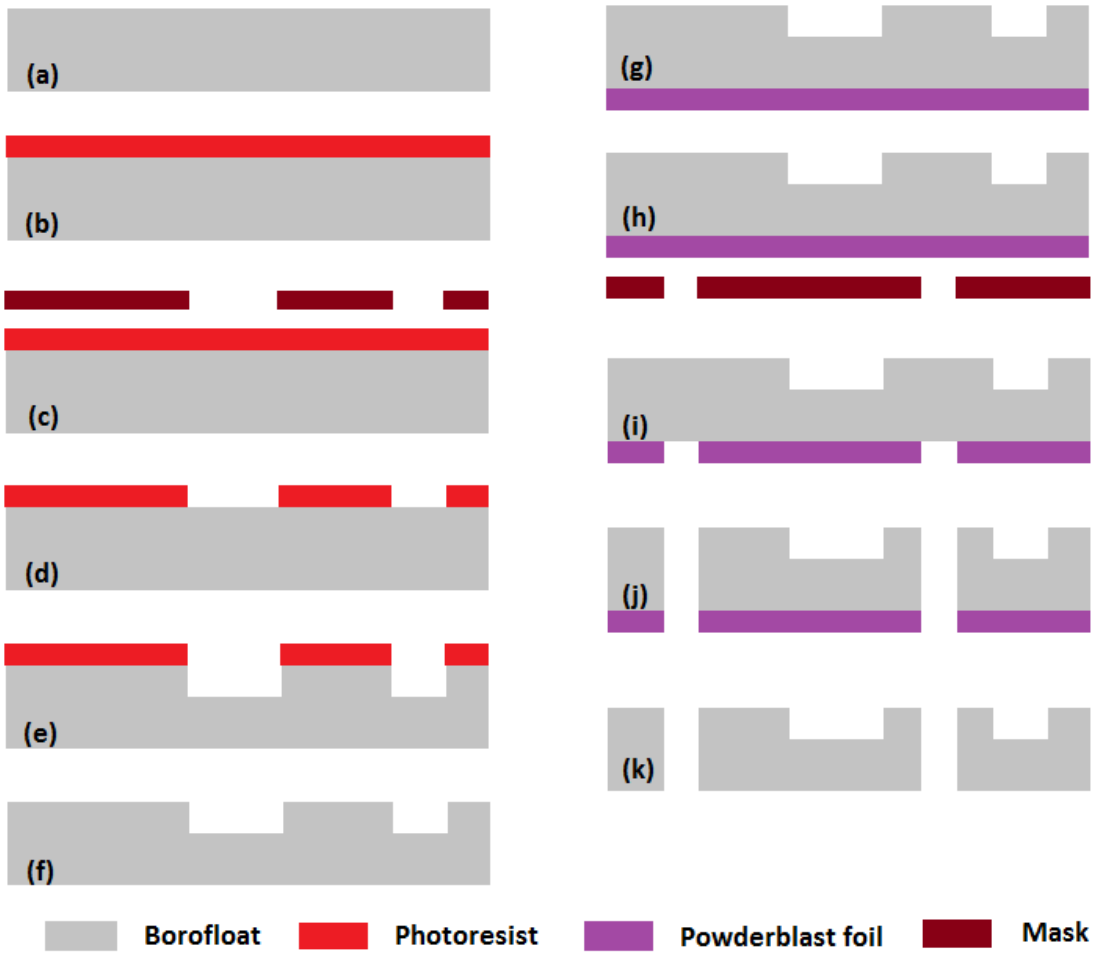

Figure 4-1: Fabrication process for the top glass wafer. Fig. a) bare wafer, b) application of photoresist, c+d) lithography and development, e+f) RIE etching and resist strip, g) lamination of BF410 at backside, h+i) lithography and development, j+k) powderblasting and foil removal.

2) Bottom wafer

Secondly, the bottom glass wafer is processed to sputter the platinum electrodes and make the bottom SU8 channel layer. SU8 is an epoxy based negative photoresist which are widely used in fabrication of microfluidic systems[45]. It is highly sensitive to UV light and suitable to make high aspect ratio and stable microstructures[46]. It is also a good material to be used in adhesive bonding

for joining different substrate types with a high bond strength at low process temperature[47]. After the cleaning procedure, 0.35 μm negative photoresist (Ti 35 ES) is applied on top of the wafer (Figure 4-2(a)). The following lithography step is the same as for the top glass wafer which are shown in Figure 4-2(b) and Figure 4-2(c). The wafer is cleaned after development in UV/Ozone for 5 minutes to remove resist residues. Afterwards, a shallow trench of approximately 150 nm deep is etched in BHF (1:7) to enclose the electrodes (Figure 4-2(d)). 10 nm titanium is first sputtered onto the wafer before sputtering a layer of 140 nm platinum for good adhesion of the electrodes (Figure 4-2(e)). The sputtered wafer is treated in aceton solution for about one hour and rinsed with aceton and isopropanol to lift off the photoresist and excess metal on it. Only the metal in the shallow trenches is left which is shown in Figure 4-2(f).

In the following step, a SU8 channel layer will be made on top of the wafer. The wafer is first cleaned in 99% HNO_3 and etched in 25% KOH (75 ℃) solution which is the same as used for the top glass wafer before applying photoresist. After the dehydration bake, 5 μm thick SU8-5 solution is spin-coated on top (Figure 4-2(g)). The wafer is then soft baked before exposure. SU8 is not soft baked under a constant temperature. The baking temperature first increases to 90 ℃ (50 ℃ for 1 minute, 65 ℃ for 1 minute, 90 ℃ for 1 minute), then ramped down to room temperature at a slow speed. After UV exposure (Figure 4-2(h)), the wafer is baked again under incremental increased temperatures and ramp down to room temperature to strengthen the photoresist. At last, SU8 is developed by propylene glycol monomethyl ether acetate (RER 600) in a spray developer (Figure 4-2(i)).

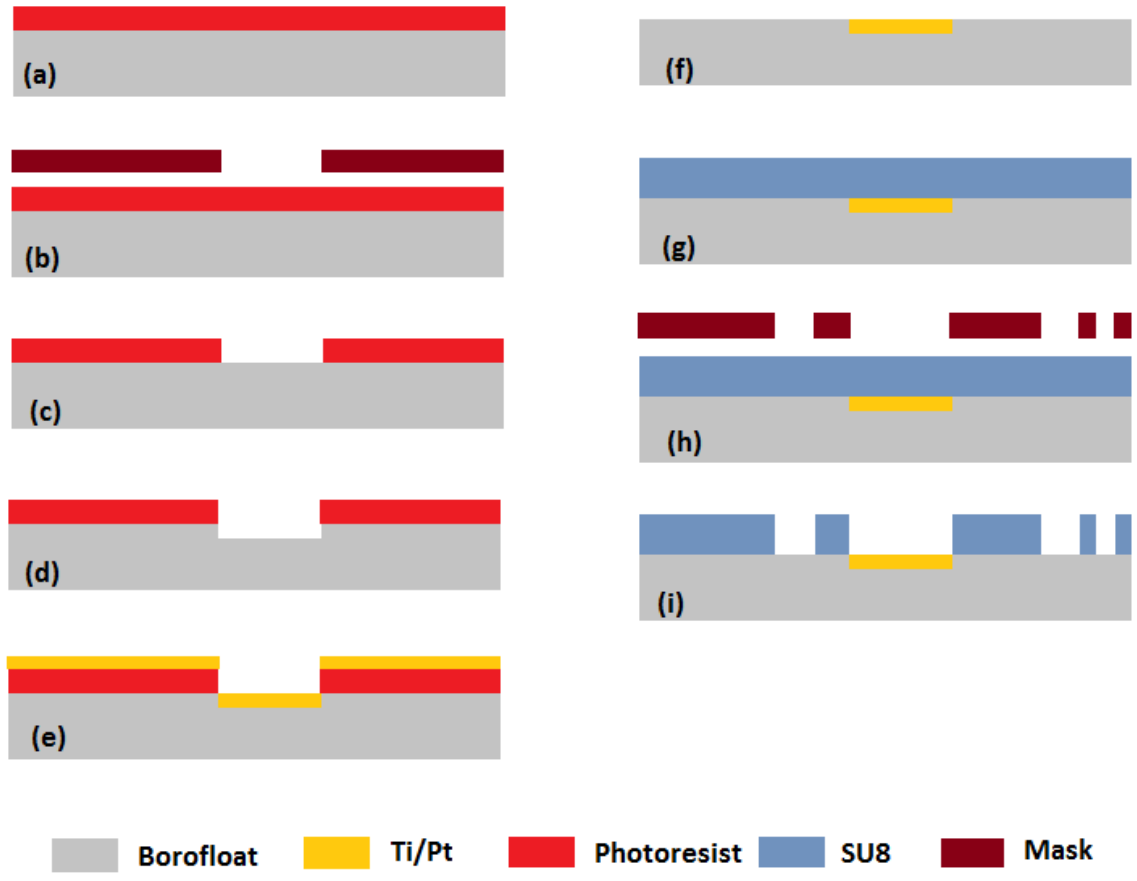

Figure 4-2: Fabrication process for the bottom glass wafer. Fig. a) application of photoresist, b+c) lithography and development, d) BHF etching, e) titanium sputtering, f) lift-off, g) application of SU8, h+i) lithography and

development.

3) Glass- SU8 bonding

The bonding process should be done immediately after SU8 channel formation to make sure the bonding is of good quality. Before bonding, the top glass wafer is cleaned in 99% HNO_3 and etched in 25% KOH (25℃) for good adhesion. After a dehydration bake, the top wafer and bottom wafer are put into a bond chuck, aligned in the EVG620. The chuck together with the two wafers are then put into an anodic bonder (EVG501) where the two wafers are pre-bonded at high temperature. The wafers in the anodic bonder are heated to 100℃. Then a 1000N force is applied to the wafers for 10 minutes. Next, the temperature is lowered to 60℃ while the gas in the system is vent out. The bonded wafers are then put in a press for one hour under 500 kg force and at 180 ℃ above the polymerization temperature[48] are applied for adhesive bonding. In the last step, the bonded wafers are diced into fifteen 15×20 mm chips. The cross-sectional view of the bonded wafer is shown in Figure 4-3.

Figure 4-3: Cross-sectional view of the wafers after bonding.

4.1.2 Process of the chip with boron-doped diamond electrode

A boron-doped diamond-on-silicon (BDD-on-Si) wafer is purchased from a supplier (NeoCoat®) which will be used to fabricate the bottom electrode layer (Figure 4(a)). The substrate is a 0.5 mm thick and 100 mm diameter silicon wafer. A 200 nm silicon dioxide layer and a 700 nm silicon nitride layer are deposited on the wafer as insulating layers. A diamond layer doped with boron particles is coated on top of the insulating layers, with a thickness between 450 and 500 nm. The doping level is 8000 ppm, corresponds to a resistivity of 10 $\mathrm{m\Omega \cdot cm}$. An 1100 mm thick glass wafer is used to fabricate the top channel layer.

First, the BDD wafer is cleaned in 99% HNO_3 solution and baked at 120 ℃ for dehydration. Then, a 3.5 μm thick positive photoresist (Olin Oir 907-35) is spin coated on top of the wafer (Figure 4-4(b)). After the lithography steps (Figure 4-4(c) and (d)), the diamond layer is shaped by reactive ion etching (RIE) in oxygen plasma where the electrode part under photoresist is kept, while the other part is etched away and the silicon nitride layer is exposed outside (Figure 4-4(e)). Oxygen plasma etches both the diamond layer and the photoresist layer, while it stops at the silicon nitride layer. Afterwards, the thickness of the diamond layer and photoresist layer is checked to make sure the part besides the electrode are completely etched, while the electrode part is still intact. The resist is stripped in Piranha solution for half an hour in an ultrasonic cleaner (Figure 4-4(f)). Next,

titanium/gold (Ti/Au) contact pads are made on the diamond electrodes for connecting the three electrodes with electrical wires of measurement set-ups (Figure 4-4(g-i)). The following steps (SU8 channel formation, top glass channel etching, and wafer bonding) will be the same as fabricating the platinum wafer, as shown in Figure 4-4(k-m).

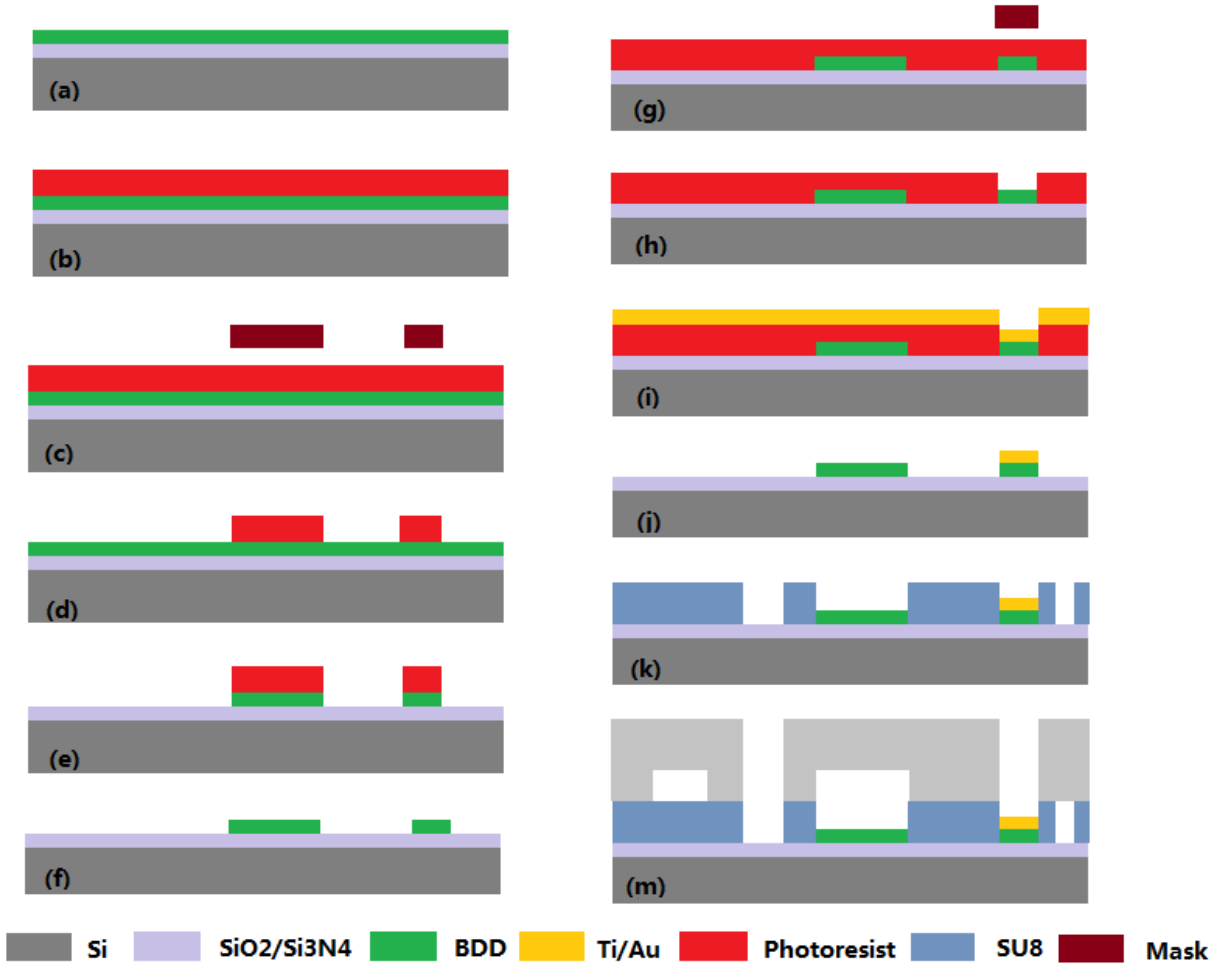

Figure 4-4: Process of the bottom BDD-on-silicon wafer. Fig. a) bare BDD substrate, b) application of photoresist, c+d) lithography and development, e+f) RIE etching and resist strip, e) application of photoresist and lithography, h) development, i) Ti/Au sputtering, j) lift-off, k) application of SU8, m) SU8-glass bonding.

4.2 Electrochemistry Measurements and conversion efficiency study

4.2.1 Setup

The setup used for the electrochemical measurements and the conversion efficiency study is shown in Figure 4-5. Two syringe pumps (Nemesys) which are controlled by a Labview application are used in the measurement. During the measurement, either of them will be connected to inlet 1 of the chip which is upstream the three-electrode system via fused glass capillary (100 μm inner diameter). One syringe contains solution with redox-active species, and a background solution consisting of a supporting electrolyte and buffer solution for measurements, while the other one contains only the background solution for rinsing the setup and for use as a control measurement. Inlet 2 which is intended to add reactants for phase II study is blocked in this measurement and will be used in

testing the function of the mixer in the next subchapter. The outlet of the chip is connected to a waste container. Electrochemical measurements are recorded using a potentiostat (Bio-Logic SP-300).

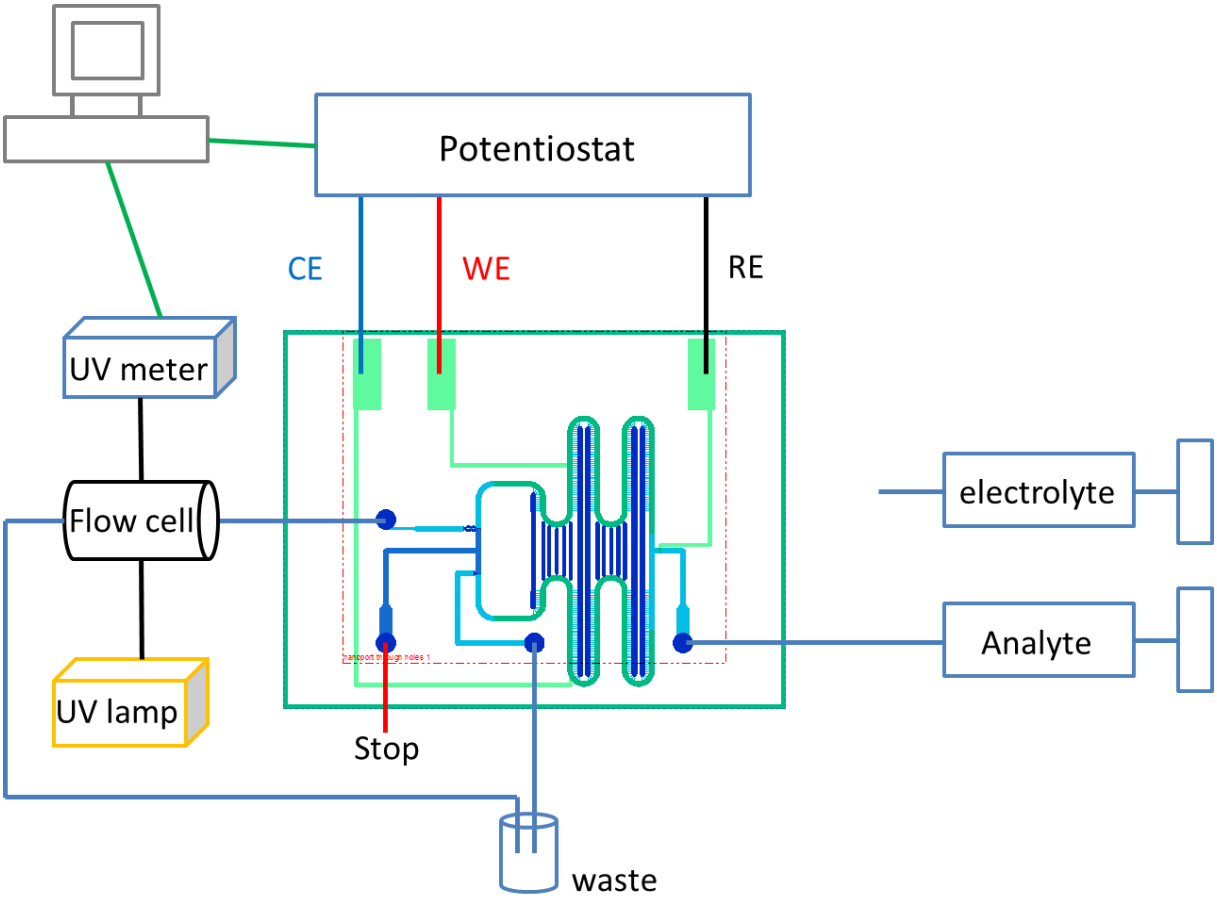

Figure 4-5: Setup used in the electrochemistry and conversion efficiency measurements.

For the UV/vis measurements the outlet of the chip is connected to a flow cell with an optical path length of 10 mm and internal volume of 2.4 μL. UV/visadsorbance measurements are recorded inside this flow cell using a deuterium light source (Ocean Optics, DH 2000) and an UV/vis spectrometer (Ocean Optics, Maya 2000pro). UV/vis measurements are recorded using a Labview application.

4.2.2 Chemicals

Different stock solutions are prepared before the measurements. For the EC measurements, consisting of the techniques - cyclic voltammetry, differential pulse voltammetry and impedance measurement, the used solution contains 1 mM potassiumferricyanide and 1mM potassiumferrocyanide as redox-active species, 0.1 M potassiumnitrate as supporting electrolyte and 10 mM phosphate buffer (pH=7). The solution used for EC-UV/vis measurement contains 0.5 mM potassiumferricyanide, 0.5 mM potassiumferrocyanide, and the same amount of electrolyte and phosphate buffer. UV/vis calibrations are conducted using different solutions containing a range of potassiumferricyanide concentrations from 0.01 mM to 1 mM.

4.2.3 Protocols

First the whole setup including the chip is rinsed with the background solution. After five minutes, the chip is rinsed with the measurement solution for five minutes. Thereafter, the electrochemical measurements start. The protocol for each kind of electrochemical measurement is illustrated as follows.

1) **Cyclic voltammetry:** Cyclic voltammetry measurements are conducted at three different flow speeds which are 0 $\mu L/min$, 0.5 $\mu L/min$, and 2 $\mu L/min$. The flow rate here refers to the rate delivered by the syringe pump which is twice the flow rate in the working electrode channel or the counter electrode channel. During each measurement, the potential is varied between a positive and a negative potential, for instance from -0.4 V to 0.4 V at a specific scan rate. Three different scan rates used in the measurements are 10 mV/s, 30 mV/s, and 100 mV/s.
2) **Differential pulse voltammetry:** Differential pulse voltammogram is recorded at a flow rate of 0 $\mu L/min$. The voltage is scanned from -0.4 V to 0.4 V with pulse heights of 2.5 mV, pulse widths of either 50 ms or 100 ms.
3) **Impedance measurements:** A two-electrode configuration is used for the impedance measurements. Bode plot is recorded between 0.1 Hz and 1MHz using a sine wave of 10 mV amplitude. The impedance values are determined from the resistive plateau at $0°$ phase in the Bode plot.
4) **Conversion efficiency study:** A constant potential of -1V or 1V is applied for several minutes while the deuterium light and spectrometer are working until the spectrum is stable.

4.3 Characterization of the mixer

Fluorescence is used to quantitatively measure the concentration distribution in the mixer. The characterization measurement of the mixer was conducted by Linda van der Hout [49]. For more details, see Linda's bachelor report [49] or appendix [B] for a brief summary.

5. Results and discussion

Due to the limited time available for this project, only the platinum chips were fabricated, up to fully functional devices. In this chapter, the fabrication results of both the platinum and the boron-doped diamond (BDD) chips will be discussed in chapter 5.1. Next, electrochemical characterizations of the platinum chip will be presented, including a study of the conversion efficiency for ferro/ferricyanide in chapter 5.2. At last, the performance of the mixer will be briefly discussed in chapter 5.3.

5.1 Fabrication results

Fabrication performance of some critical process steps will be discussed in this chapter, including etching of top glass channel layer, formation of bottom SU8 channel layer, SU8 to glass bonding, and etching of diamond electrode layer.

5.1.1 Etching of the top glass layer

As described in chapter 4.1.1, the top glass channel layer was etched in He, C_4H_8, and CH_4 plasma on an 1100 mm thick Borofloat glass wafer. The surface profile of the channel layer was checked afterwards to determine the etch rate of glass and photoresist. The etching rate of photoresist is 130nm/min, while the etching rate of glass is varied in the range of 350 to 380 nm/min in reality.

The surface profile of the wafer was measured again. However, the channel depths in different part of the wafer were not identical. For chip design 3,the main frit channels have a large channel width of 100 μm and a low structure density, as shown in Figure 5-1(a). The depth of the channel is identical with the designed parameter which is 5μm. For chips of the other two designs which have high density of structures frit channels (Figure 5-1(b)), the depths of the channels are varied from 4.2 μm to 4.8μm. This is because when the reaction is under diffusion-limited regime, the flow may not be high enough to supply reactants when the structure area increased. Thus,the rate is lower for densely displayed arrays because there is more material to be etched. This area-dependent reaction rate will lead to an etch-depth difference between isolated and array features[43]. On the other hand, this differential channel depth profile is only obvious for chips in the center area of the wafer, while chips near the edge of the wafer show an identical channel depth of 5 μm even for designs with array of densely displayed frit channels. This may be also due to the structure density in the center of the wafer is larger than near the wafer edge.

For the chips with array of shallower frit channels, the total depths of the frit channels (together with bottom SU8 channel layer) varies from 9.2 μm to 9.8μm which are only 2% to 8% deviation from the designed parameters and are not expected to have a significant influence on the performance of the frit channel system.

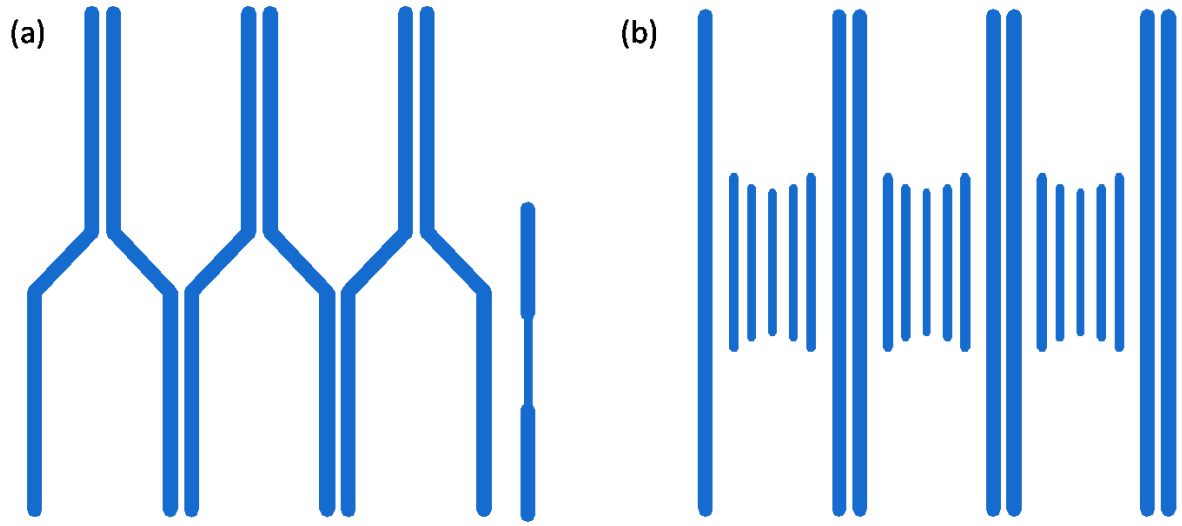

Figure 5-1: Layout of the top layer frit channels of two designs which have (a) low structure density or (b)high structure density.

The etching performance on the micropillars array and the micromixer are of mainly concerned due to their small dimensions. As discussed in chapter 3, the diameter of each individual micropillar is only 5 μm, as well as the space between two adjacent pillars. The minimum structure size of the micromixer is only 10 μm. Figure 5-2 shows the picture of the micropillars array after etching. The individual pillar is truncated cone shape, with the bottom diameter of 6.1 μm and the top diameter of 1.6 μm in average. Figure 5-3 shows the picture of the micromixer, in which the measured channel width is 9.8 μm which is supposed to be 10 μm in the design.These dimensions are all among a reasonable deviation range.

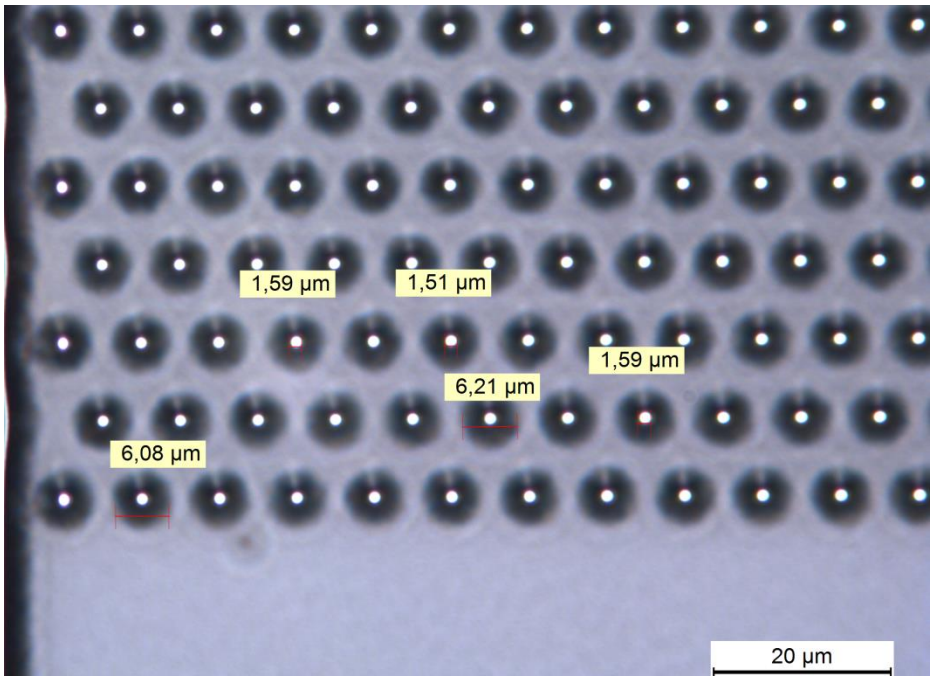

Figure 5-2: Optical micrograph of the micropillars array fabricated by reactive ion etching.

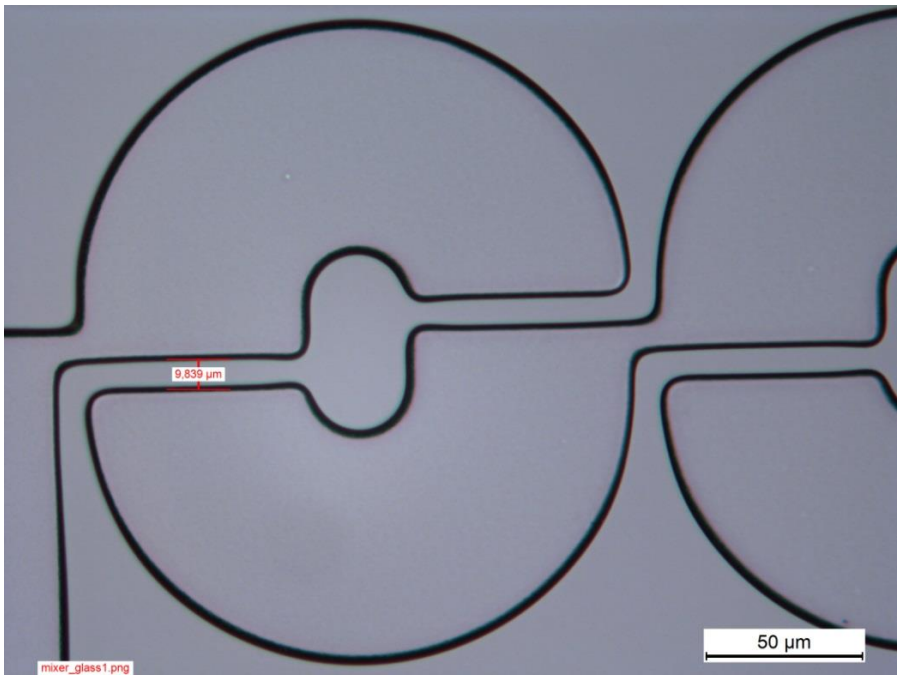

Figure 5-3: Optical micrograph of the glass layer of the micromixer fabricated by reactive ion etching.

5.1.2 SU8 channel layer formation

The bottom channel layer is made of SU8 photoresist which is able to produce high aspect ratio structures. Figure 5-4 shows the micropillars array fabricated after the lithography and development steps. Each individual micropillar has a better aspect ratio than the glass micropillar made by reactive ion etching, with a diameter of 4.1 μm in average.

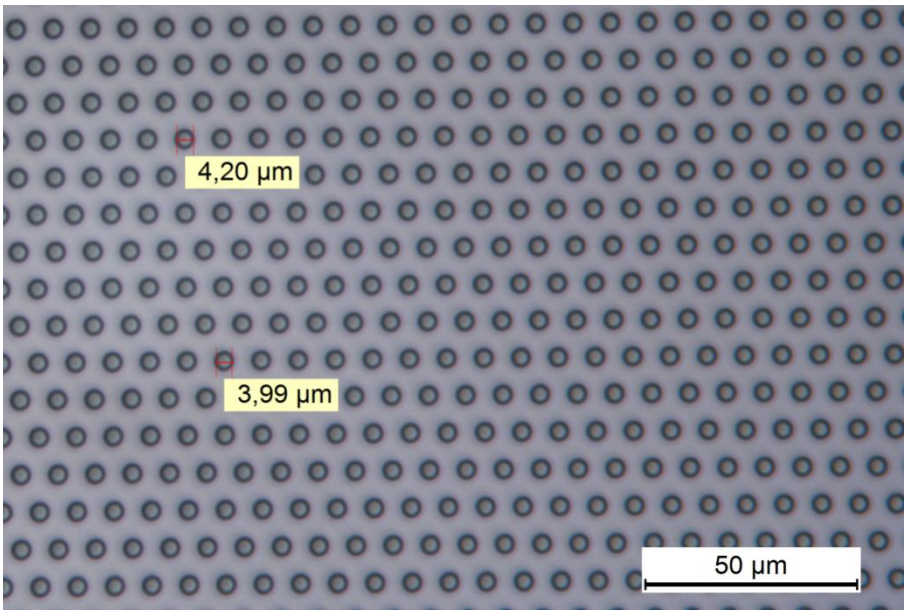

Figure 5-4: Optical micrograph of the micropillars array made of SU8 photoresist.

5.1.3 SU8 to glass bonding

Since the micromixer uses both top and bottom channel layer, and the minimum channel width is only 10 μm, it needs to pay special attention when bonding the two channel layers together, especially during the pre-alignment and transportation of the pre-bonded wafers. The bonding performance is good under 180 ℃ and 500 kg for one hour, no leakage discovered in the later experiments. Figure 5-5 shows the microscope photo of the mixer after bonding, as well as the measurements of some critical dimensions. The width of each of the three channels shown in the photo is designed to be 10 μm as described in chapter 2, while the real channel width are 8.18 μm, 9.65 μm, and 8.39 μm, respectively. The deviations of the dimensions are in an acceptable range.

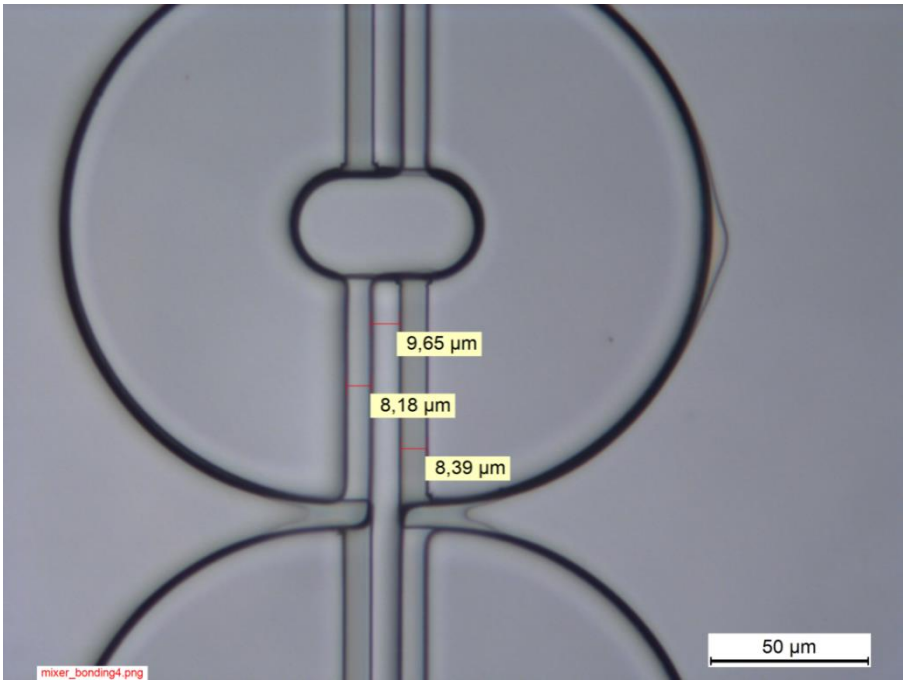

Figure 5-5: Optical micrograph of the mixer after SU8 –glass bonding.

5.1.4 Etching of diamond electrode layer

The BDD electrode after shaped by reactive ion etching is shown in Figure 5-6(a), while one of the gold contact pads is shown in Figure 5-6(b).

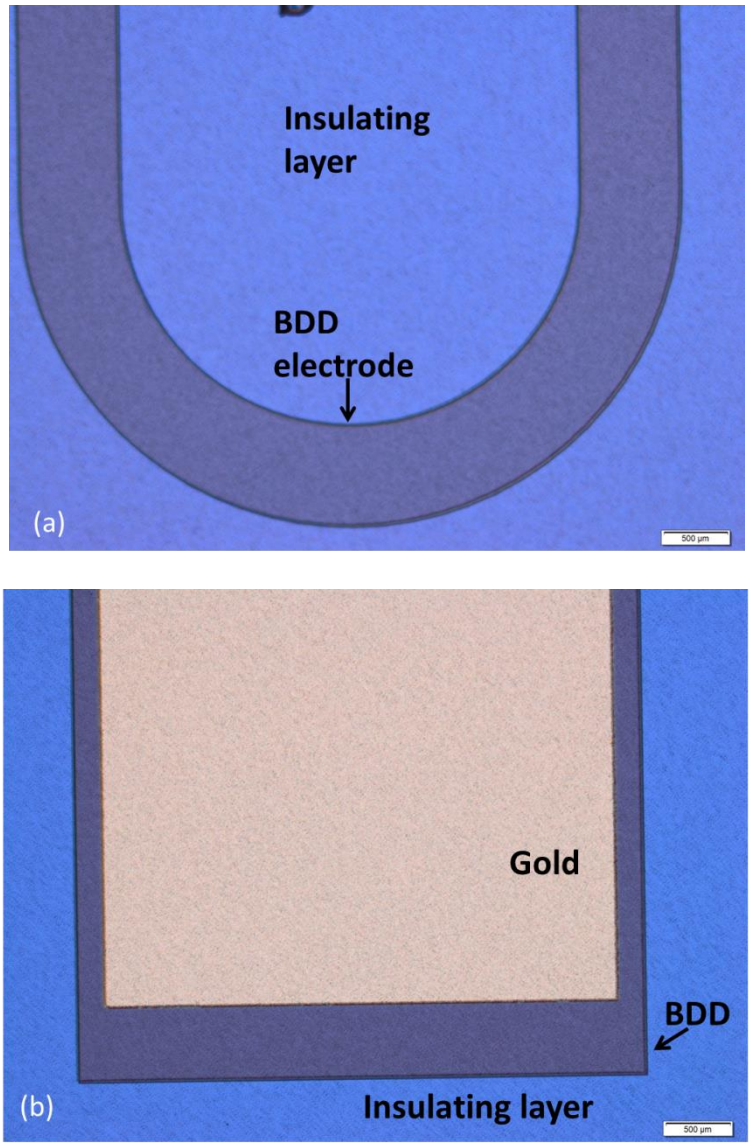

Figure 5-6: Optical micrographs of the BDD wafer after etching. (a)BDD electrode after shaping, (b) Au contact pad deposited on BDD electrode.

In order to make sure the diamond part besides the electrodes is all etched away, while the electrodes part is kept intact, the resistivity of the electrodes and insulating part of all fifteen chips on the same BDD wafer is checked after etching via 2-points probe, resist stripping and sputtering of contact pads. However, the resistivity of the electrodes varies from one side of the wafer to the other side as shown in Figure 5-7, which indicates the etching rate across the wafer is not uniform. The average resistivity of the electrode is $12 m\Omega \cdot cm$which indicates a good retention of boron-doped diamond. The measured resistivity between the working electrode and the counter electrode is in the range of several $k\Omega \cdot cm$ which means a complete removal of the BDD layer. The conductivity of the contact pads is also good because the resistivity measured between the contact pad and the diamond electrode is similar with the resistivity of the diamond electrode.

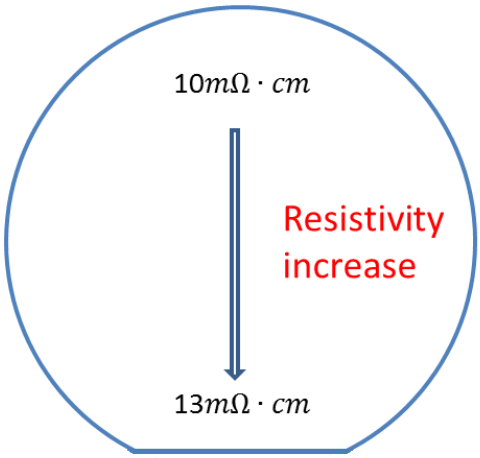

Figure 5-7: Resistivity of the BDD electrode is different across the wafer, with a higher value near the flat side.

5.2 Measurement results of chip with platinum electrodes

All three different designs were tested using the protocols described in chapter 4.2.3. In this chapter, the electrochemical and UV/vis absorbance measurement results of three different chip designs will be discussed.The length of the working electrode in three different designs are comparable. Thus, the difference in the design of the frit channel system is the main factor influencing the measurements.

5.2.1 First chip design

The first chip design with parallel working and counter electrode as shown in Figure 5-8 was tested with 1mM/1mM ferrocyanide/ferricyanide, 0.1M KNO_3, and 10 mM phosphate buffer at flow rates of 0 $\mu L/min$, 0.5 $\mu L/min$, and 2 $\mu L/min$ which is the flow rate at the inlet of the chip. The flow rate over the WE or CE channel is half of the flow rates which are 0 $\mu L/min$, 0.25 $\mu L/min$, and 1 $\mu L/min$, correspondingly. All the flow rates mentioned in the following subsections will be the flow rates over the working electrode.

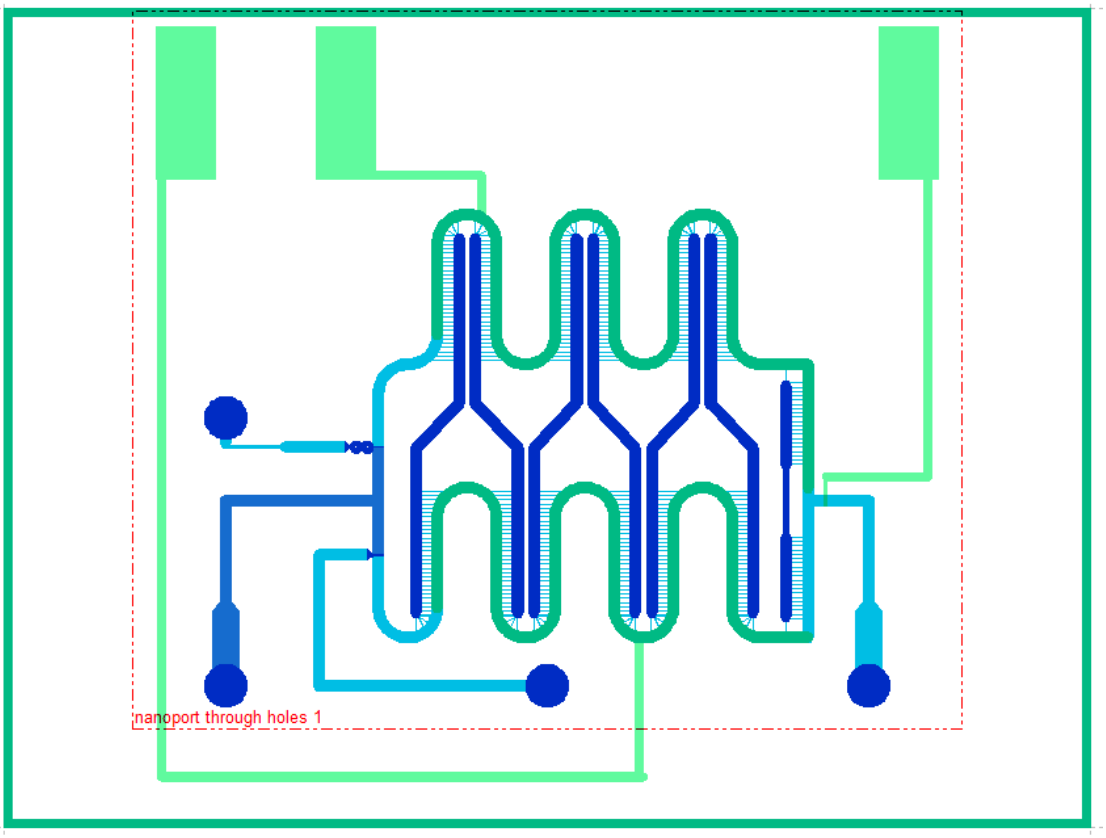

Figure 5-8: Layout of the chip with parallel working electrode and counter electrode. Powderblast holes are not shown for clarity.

Cyclic voltammetry is able to rapidly acquire qualitative information about the thermodynamics of redox processes and the kinetics of electron transfer reactions[50]. Figure 5-9 shows the cyclic voltammograms of the chip at different scan rates(10 mV/s, 30 mV/s, 100 mV/s) without flow. All three cyclic voltammetry graphs show clear oxidation and reduction peaks. As the scan rate increases from 10 mV/s to 100 mV/s, the current increases. This is because at a slow scan rate, it takes longer time to record the cyclic voltammogram. The diffusion layer will grow much wider from the electrode surface to the bulk solution, compared with a fast scan rate. Thus, the flux of the ions to the electrode surface will be smaller which lead to a smaller current, as the current is proportional to the flux towards the electrode surface, according to Fick's first law of diffusion.

$$i = nFAD\frac{\partial C}{\partial x} \quad (38)$$

Where D is the diffusion coefficient, F is Faraday's constant, A is the electrode area, and $\frac{\partial C}{\partial x}$ is the concentration gradient.

On the other hand, the peak separation of oxidation and reduction peak slightly increases as the scan rate increases. Possible reason of this phenomena is that as the current increases, the ohmic drop on the electrolyte resistance between working and reference electrode ($i \cdot R_O$) becomes more significant.

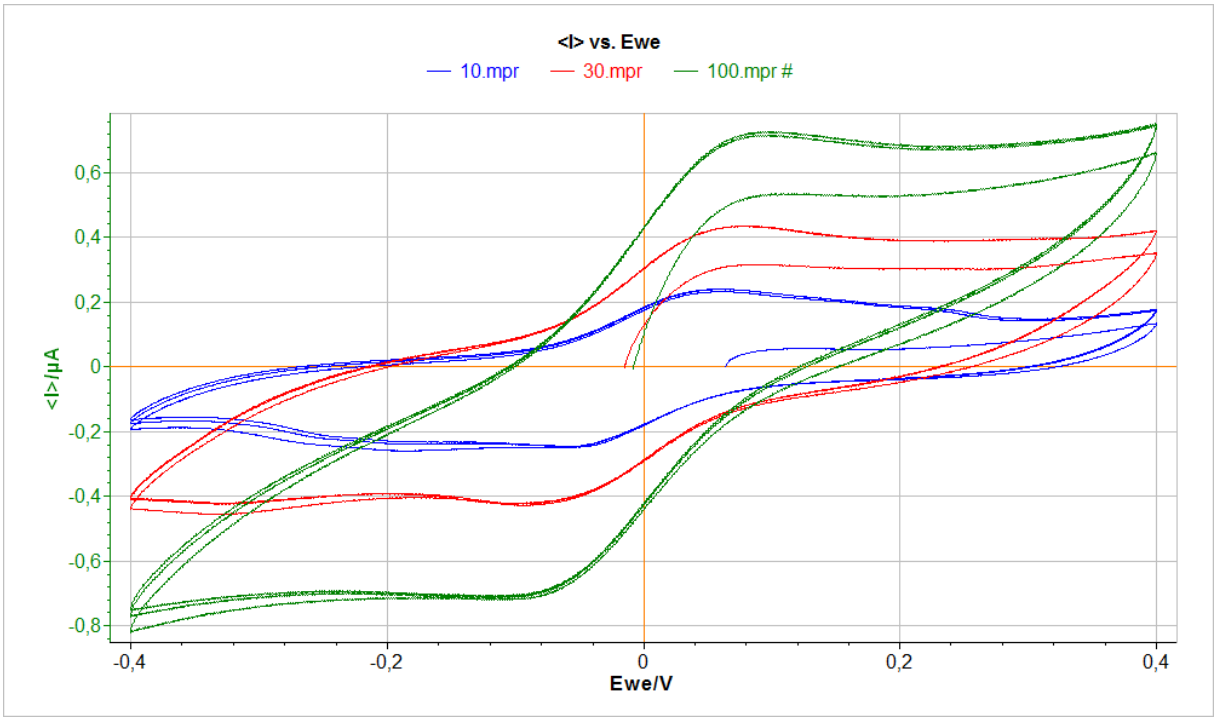

Figure 5-9: Cyclic voltammetry measurement of the chip design with parallel working and counter electrode at a flow rate of 0 $\boldsymbol{\mu L/min}$ at scan rates of 10 mV/s (blue) , 30 mV/s (red), and 100 mV/s (green).

As in Figure 5-9, the chip shows a typical diffusion limited behavior at flow rate of 0. The measured current is entirely due to the ions diffusion towards the working electrode. As the flow speed increases, convection begins to contribute to the current by fostering the supply of new redox species to the electrodes faster. As long as the reaction rate is limited by mass-transport, the measured current will be the sum of diffusion and convection. Thus the peak currents in the cyclic voltammogram increases as the flow rate increases, as shown in Figure 5-10.

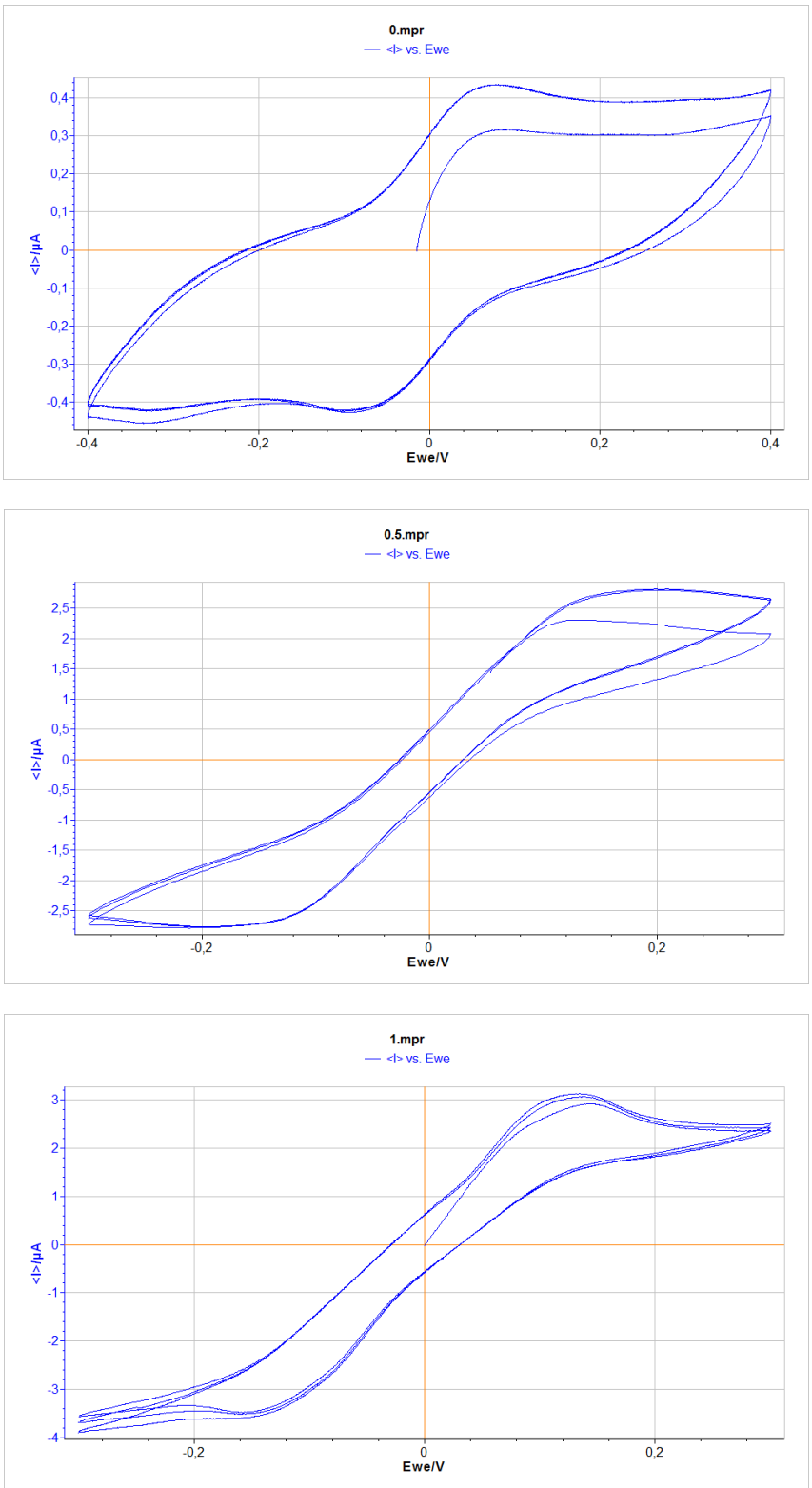

Figure 5-10: Cyclic voltammograms recorded at scan rate of 30 $\boldsymbol{mV/s}$ at different flow rate. Top: no-flow; Middle: 0.25$\boldsymbol{\mu L/min}$; Bottom: 1 $\boldsymbol{\mu L/min}$.

The current in a cyclic voltammogram includes not only faradaic current, but also capacitive current from electrode double-layer charging. Thus, a differential pulse voltammetry (DPV)is also plotted in

which only faradaic current is extracted, as shown in Figure 5-11. The symmetrical peak indicates the reaction in the system is reversible. The shape of the peak current is able to describe the behavior of the electrochemical system which will be compared with the other two designs in the following chapters.

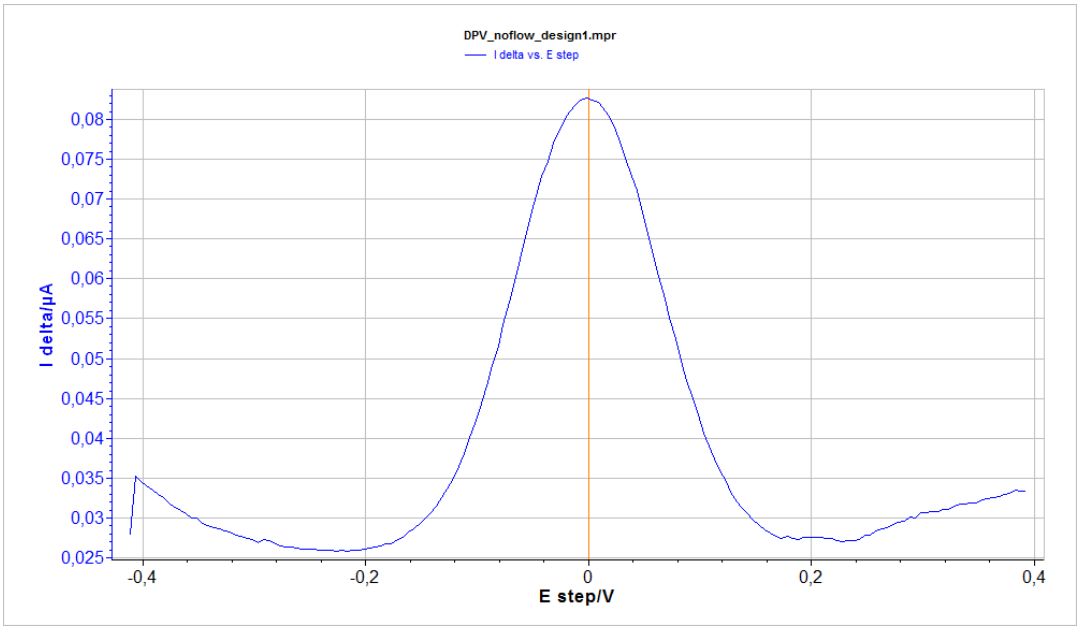

Figure 5-11: Differential pulse voltammetry measurement of chip design 1 with pulses width of 100 ms.

The impedances between the three electrodes are also measured which are shown in appendix [A]. The electrolyte resistance between the working electrode and the counter electrode is 251 $k\Omega$, that between the working electrode and the reference electrode is 891 $k\Omega$, and that between the counter electrode and the reference electrode is 794 $k\Omega$.

Conversion efficiency of the chip is studied with 0.5mM/0.5mM ferrocyanide/ferricyanide, 0.1M KNO_3, and 10 mM phosphate buffer. Ferricyanide shows UV/vis absorbance at 418nm[51]. The amount of ferricyanide in the solution can be measured by measuring the ferricyanide absorbance at this wavelength according to the Beer-Lambert law:

$$E = \varepsilon \cdot c \cdot L \qquad (39)$$

Where E is the absorbance, ε is the extinction coefficient, c is the concentration of ferricyanide, and L is the extinction wavelength, which is 418 nm in this case. Before measuring the conversion efficiency of the chip, the UV/vis absorbance at 418nm is calibrated for different ferricyanide concentrations from 0.01mM to 1mM. The calibration result at flow rate of 1$\mu L/min$ is shown in Figure 5-12.

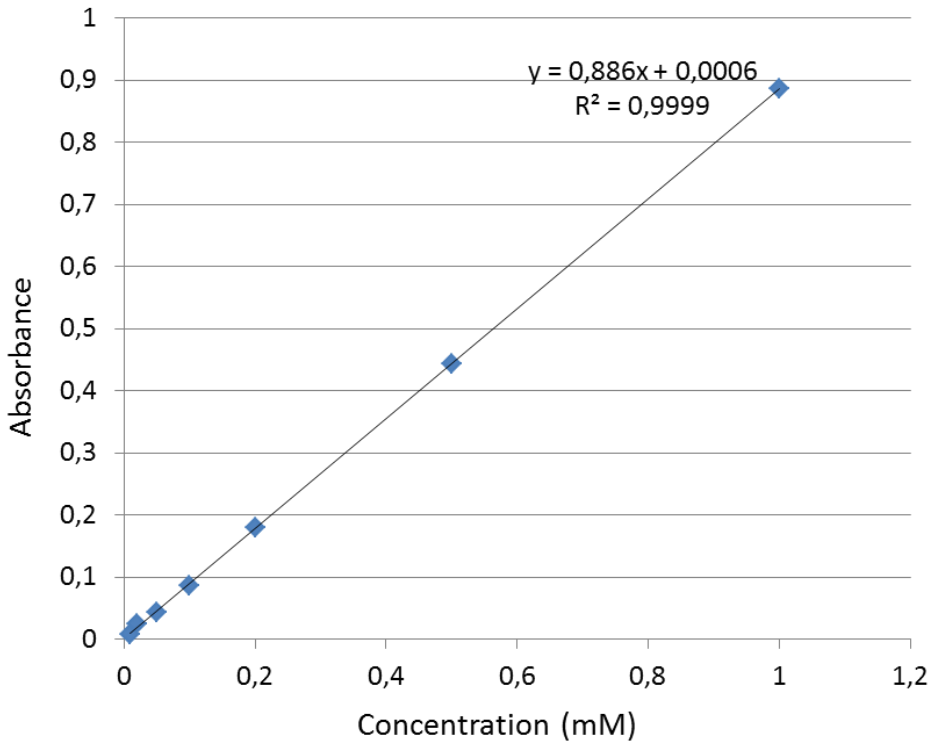

Figure 5-12: Calibration curve for UV/vis absorbance of ferricyanide at flow rate of 1 $\boldsymbol{\mu L/min}$.

Next, the test solution is oxidized at 1V or reduced at -1 V on the chip at a flow rate of 1$\mu L/min$. The concentration of ferricyanide product is measured by the UV/vis setup. At oxidation potential, ferrocyanide is converted to ferricyanide which is indicated by increasing of the absorbance (Figure 5-13 (a)). At reductive potential, ferricyanide is reduced to ferrocyanidewhich corresponding to decreasing of absorbance (Figure 5-13 (b)). The measured absorbance of the solution before conversion, during oxidation and reduction is given in Table 5-1 and in appendix [A]. From the measured data, the conversion efficiency at both oxidation potential and reduction potential are 93%.

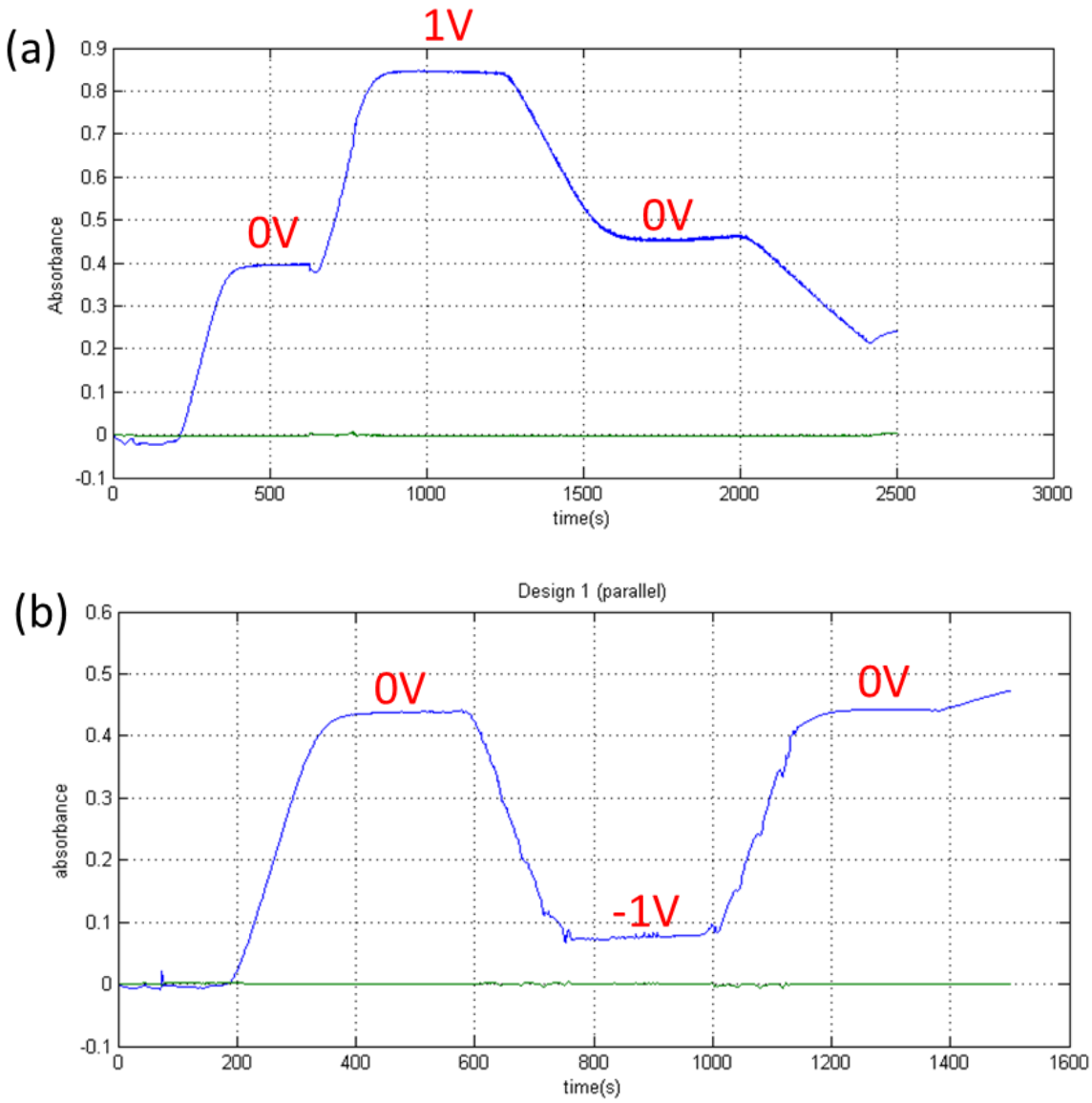

Figure 5-13: Absorbance measurements of chip design 1 in a solution of 0.5 mM/0.5 mM ferrocyanide/ferricyanide, 0.1 M KNO_3 and 10 mM phosphate buffer at flow rate of 1 $\mu L/min$.

Table 5-1: UV/vis absorbance measurement of ferricyanide in chip design 1.

U(V)	Absorbance
0	0.38
1	0.846
-1	0.075

5.2.2 Second chip design

The second chip design with antiparallel working electrode and counter electrode, thus with different frit channels pattern (Figure 5-14) was tested with the same protocols.

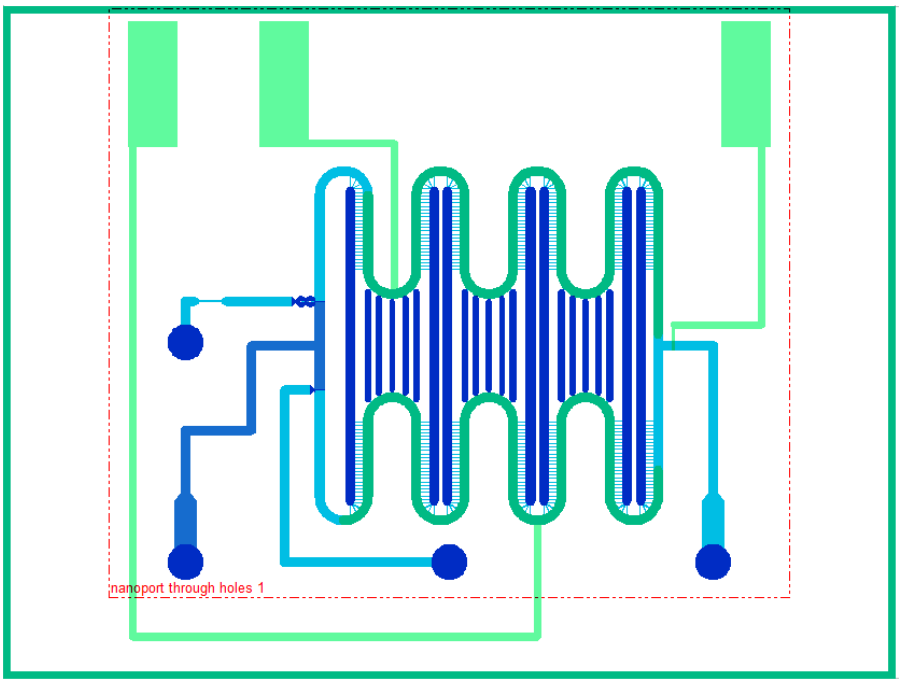

Figure 5-14: Layout of the chip with antiparallel working electrode and counter electrode.

Figure 5-15 shows the cyclic voltammograms of chip design 2 at flow rate of 0 at different scan rates (10 mV/s, 30 mV/s, 100 mV/s). Similar as chip design 1, all three cyclic voltammograms show clear oxidation and reduction peaks. The peak current at scan rate of 10 mV/s is similar with that measured of chip design 1. However, the peak current increases dramatically when the scan rate increases. At scan rate of 10 mV/s, the peak separation is approximately 80 mV which is similar with chip design 1. However, as the scan rate increases from 10 mV/s to 100 mV/s, the increase of peak separation is larger than that of chip design 1.

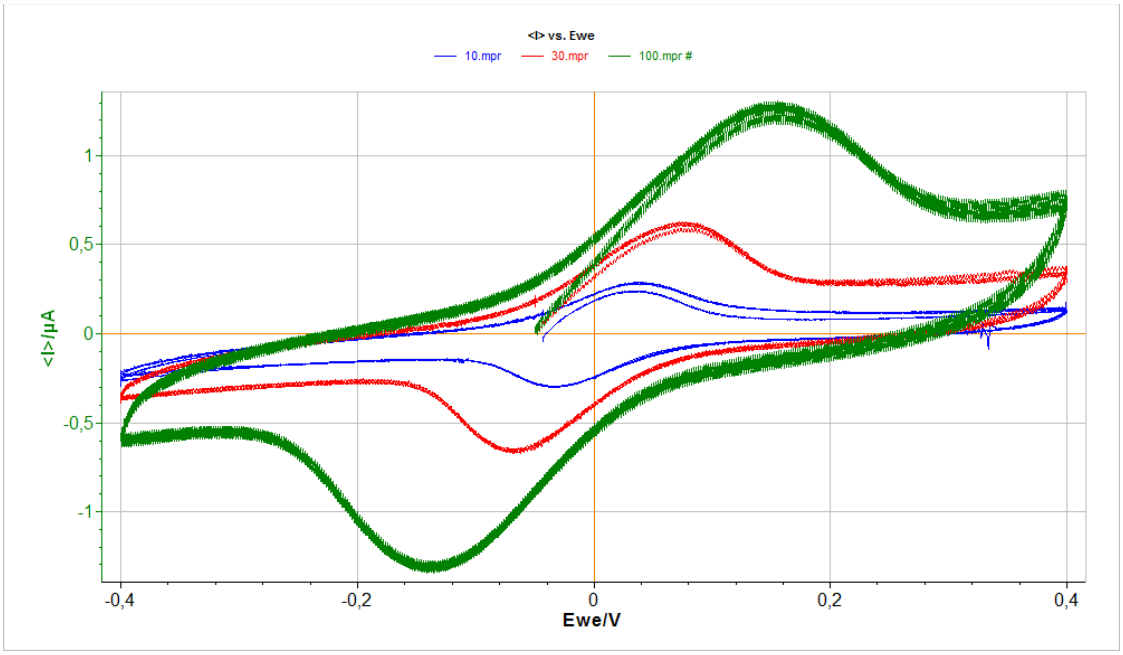

Figure 5-15: Cyclic voltammogramsof the chip design with antiparallel working and counter electrode at a flow rate of 0 $\boldsymbol{\mu L/min}$ at scan rates of 10 mV/s (blue) , 30 mV/s (red), and 100 mV/s (green).

The differential pulse voltammogram of chip design 2 which was recorded using the same protocol for the first chip design is shown in Figure 5-16. Compared with the DPV of chip design 1, the peak current is lower and the peak shape is unsymmetrical, with the peak potential shifts towards more negative potential compared with the DPV of design 1 which is an indication of uncompensated IR-drop[52]. In a system absent of ohmic drop, the peak of DPV is located near the standard potential of the redox couple, according to Nernst equation:

$$E - E_0 = \frac{RT}{nF} \ln \frac{c_O}{c_R} \quad (40)$$

Where E is the potential applied by the potentiostat, E_0 is the standard potential, c_O and c_R are the concentrations of oxidant and reductant. When an additional IR term is added to the left of the equation, the peak of the curve will shift negatively.

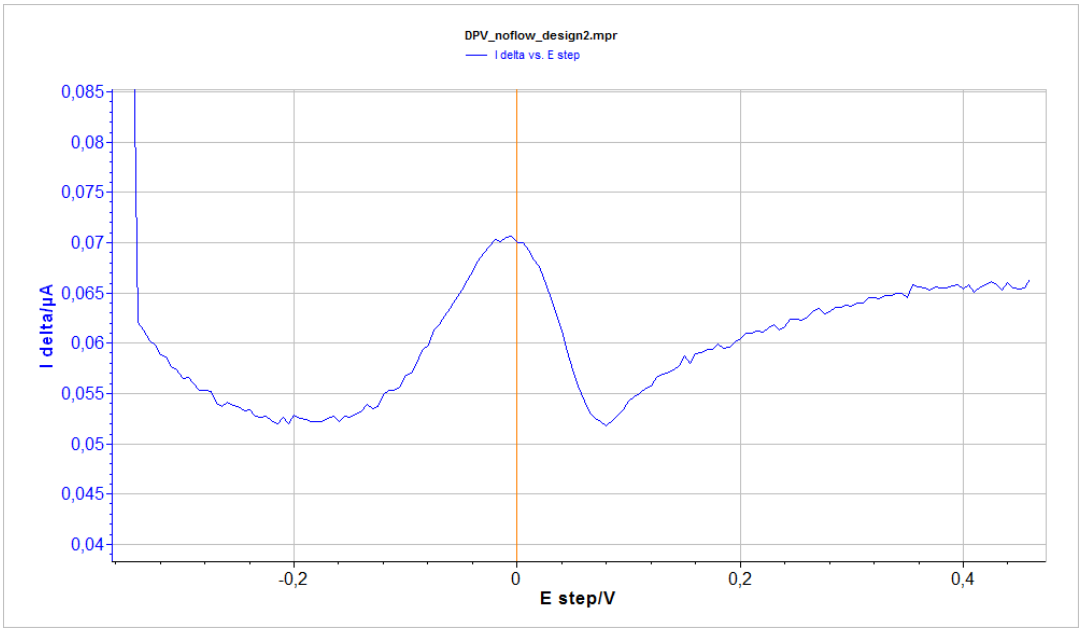

Figure 5-16: Differential pulse voltammetry measurement of chip design 1 with pulses width of 100 ms.

The electrolyte resistance between the working electrode and the counter electrode is 145$k\Omega$, that between the working electrode and the reference electrode is 316$k\Omega$, and that between the counter electrode and the reference electrode is 501 $k\Omega$. The impedance measurements are shown in appendix [A].

The result of the conversion efficiency is shown in table 5-2. The measurement graph is shown in appendix [A]. According to the measured absorbance, the oxidation efficiency is 94%, while the reduction efficiency is 84%.

Table 5-2: UV/vis absorbance measurement of ferricyanide in chip design 2.

U(V)	Absorbance
0	0.437
1	0.848
-1	0.068

5.2.3 Third chip design

The working electrode and the counter electrode in the third design is also antiparallel, but in a different arrangement, in which the distant part between WE and CE is larger than that in chip design 2. Thus, the frit channel system and the resistance between the three electrodes differ from that of chip design 2. The layout of chip design 3 is shown in Figure 5-17.

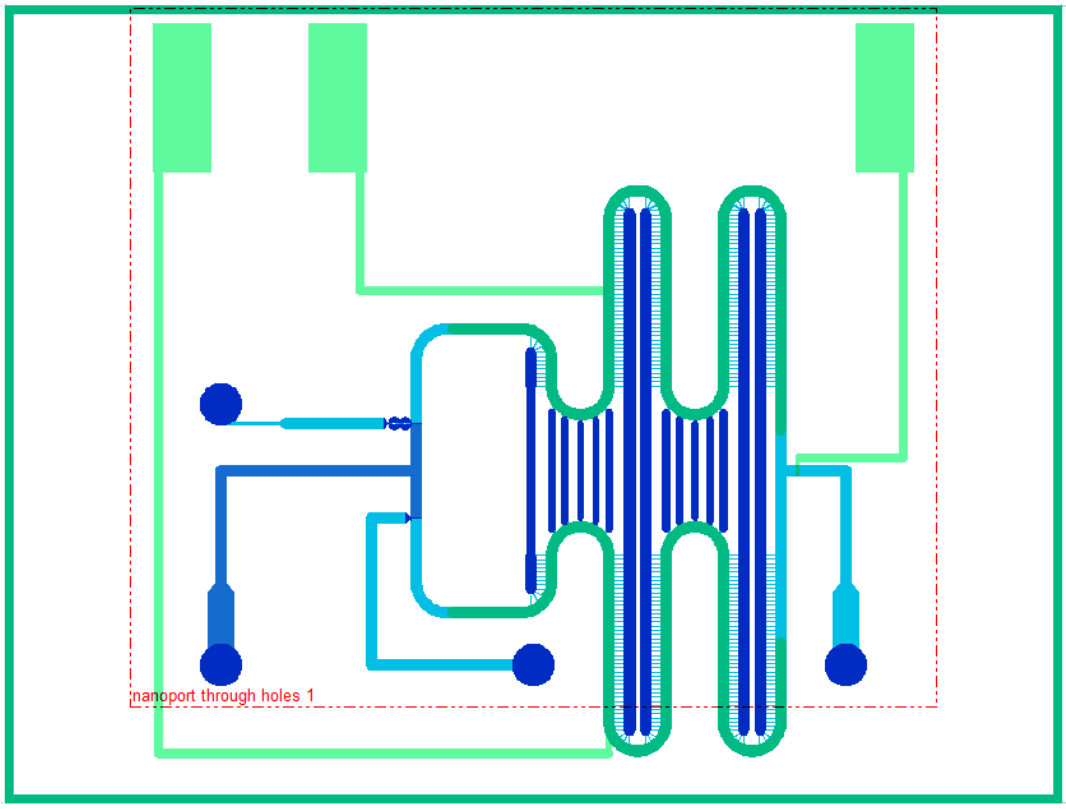

Figure 5-17: Layout of the chip with antiparallel working electrode and counter electrode, but in a different footprint with Figure 11.

Figure 5-18 shows the cyclic voltammograms of chip design 3 at flow rate of 0 at different scan rates (10 mV/s, 30 mV/s, 100 mV/s). The currents measured are in the similar range as chip design 1, and less than half of the currents measured of chip design 2. However, the cyclic voltammograms do not show clear oxidation and reduction peaks, but a more ohmic behavior. At scan rate of 10 mV/s, the peak separation is approximately 80 mV which is similar with chip design 1. The peak separations are also larger than that of chip design 1 as the scan rate increases.

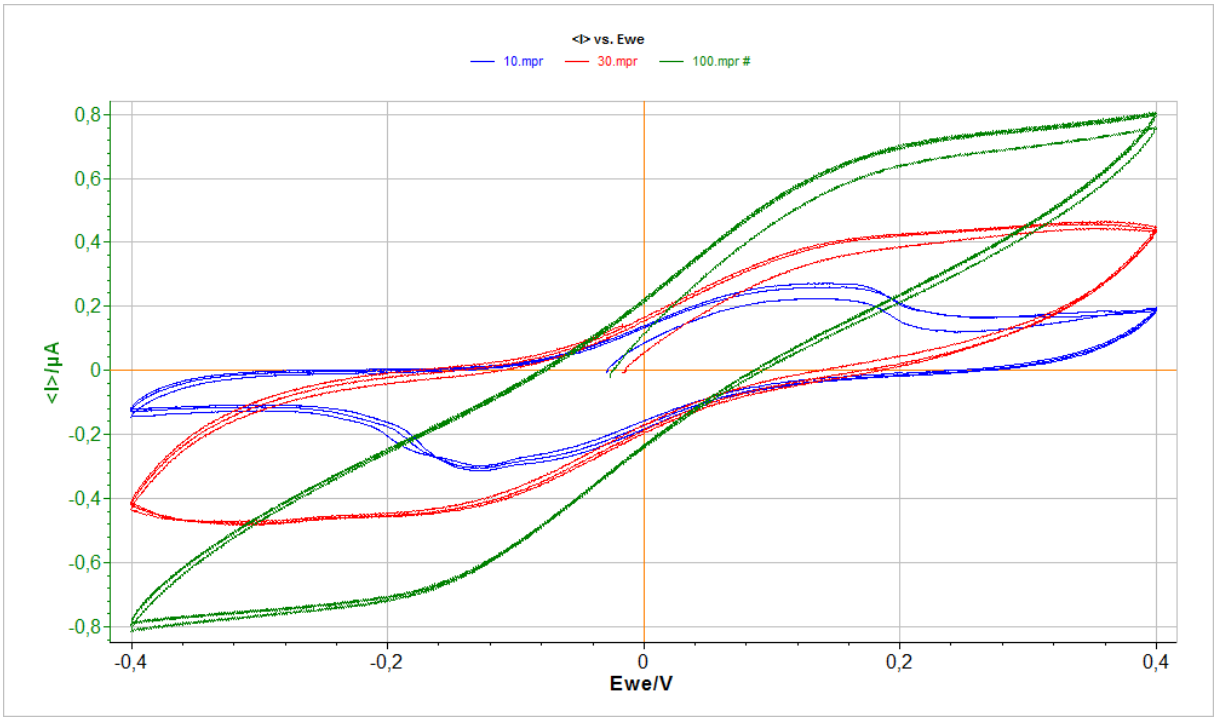

Figure 5-18: Cyclic voltammograms of chip design 3 at a flow rate of 0 $\boldsymbol{\mu L/min}$ at scan rates of 10 mV/s (blue) , 30 mV/s (red), and 100 mV/s (green).

The differential pulse voltammogram is shown in Figure 5-19. The peak height in the DPV, as well as the peak current in the cyclic voltammograms are comparable to that in the measurement of chip design 1.

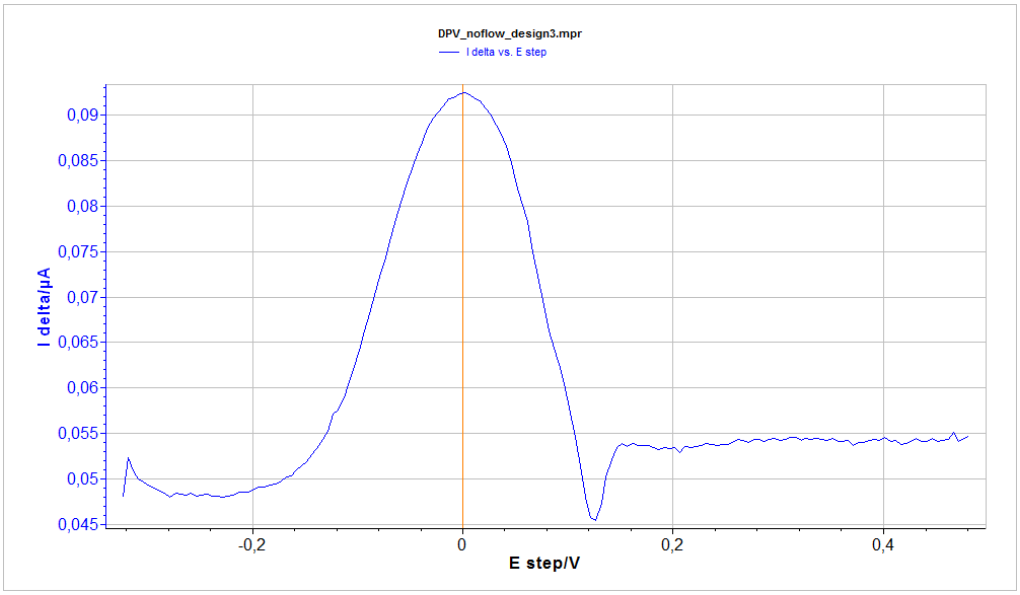

Figure 5-19: Differential pulse voltammetry measurement of chip design 1 with pulses width of 100 ms.

The electrolyte resistance between the working electrode and the counter electrode is $794k\Omega$, that between the working electrode and the reference electrode is $631k\Omega$, and that between the counter electrode and the reference electrode is $1.26M\Omega$. The measurements are attached in appendix [A].

The UV/vis absorbance is also measured for chip design 3 which are shown in Table 5-3. The oxidation efficiency is 73%, while the reduction efficiency is 79%.

Table 5-3:UV/vis absorbance measurement of ferricyanide in chip design 3.

U(V)	Absorbance
0	0.497
1	0.861
-1	0.105

5.2.4 Discussion

In chapter 5.2.1-5.2.3 measurements on three chip designs with different frit channel layout were presented and discussed. The measurements of the three designs will be compared with each other, and with the theoretical calculations as well.

By comparison the cyclic voltammograms of all three chip designs, chip 3 shows most severe ohmic behavior indicated by lacking of redox peaks. Although chip 2 shows larger peak separation than chip 1 at the same scan rates, the peak currents are almost twice of chip 1 which makes it difficult to compare the uncompensated resistance which causes the ohmic drop ($E_O = IR_O$) merely from the cyclic voltammograms. Thus, the equivalent circuits of the electrochemical cell are analyzed and the resistances between either two of the three electrodes are measured. During a cyclic voltammetry measurement, the EC cell can be simplified into the circuitry shown in Figure 5-20. The current flow through the whole system (i_C) is measured in the cyclic voltammograms. While the current flow between the WE and RE (i_{WR}) is only part of i_C. The theoretical value of the resistances can be used to deduct the relation between i_C and i_{WE}. For example in chip 2, the calculated value of the three electrodes shown in Figure 20 are: $R_1 = 345\ k\Omega, R_2 = 2.07\ M\Omega, R_{frit} = 72\ k\Omega$ in which R_2 is almost 28 times of R_{frit}. Thus, i_{WR} can be derived as:

$$i_{WR} = \frac{R_{frit}}{R_1 + R_2} i_C \qquad (41)$$

Because R_2 is extremely large compared with R_{frit}, current flow from WE to RE is negligible which will greatly reduce the ohmic behavior of the system.

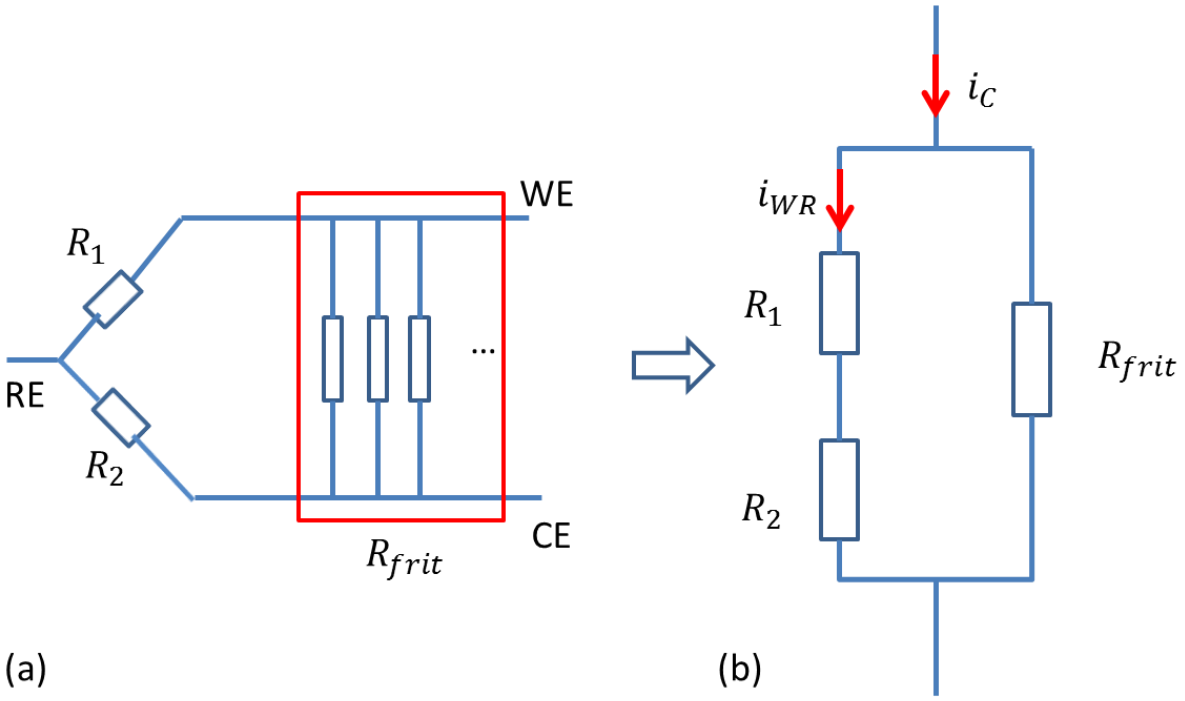

Figure 5-20: The equivalent circuit (a) and its simplification during cyclic voltammetry measurements (b) of the electrochemical cell.

The real current should be calculated according to the measured resistances. In the impedance measurements, the measured resistance between the WE and RE is R_1 parallel with the sum of R_2 and R_{frit} which is:

$$R_{WR} = R_1 \parallel (R_2 + R_{frit})$$

The resistance between WE and CE, as well as RE and CE also have similar expressions:

$$R_{WC} = R_{frit} \parallel (R_1 + R_2)$$

$$R_{CR} = R_2 \parallel (R_1 + R_{frit})$$

The real values of R_1 and R_2 can be estimated according to the measured values of R_{WR}, R_{WC}, and R_{CR}. Theoretically, R_2 is almost 6 times of R_1, and 28 times of R_{frit}. Accordingly, the above equations can be approximate to:

$$R_{WR} \approx R_1$$

$$R_{WC} \approx R_{frit}$$

$$R_{CR} \approx R_2 \parallel (R_{WC} + R_{WR})$$

i_{WR} can be estimated further. The uncompensated resistance which cause the ohmic drop in the cyclic voltammogram can be calculated by the following equation:

$$\Delta E_{peak} - \Delta E_p^0 = i_{WR} \cdot R_o \qquad (42)$$

Where ΔE_{peak} is the peak separation in the cyclic voltammogram, ΔE_p^0 is the ideal peak separation of a one-electron transferred reversible redox couple. Theoretical value of ΔE_p^0 is 0.059V, while the real value is always influenced by many factors like electrode materials, electrolyte solutions which is larger. In order to determine the ohmic drop, the real value of ΔE_p^0 should be measured in the future.

Table 5-4 shows the measured resistance and the theoretical calculations between the three electrodes of different chip designs which can be utilized to compare the ohmic drop in the three designs in the future.

Table 5-4: Comparison of the resistance between three electrodes and the theoretical calculations

Design	R_{WE-CE} (practical)	R_{WE-CE} (theoretical)	R_{WE-RE} (practical)	R_{CE-RE} (practical)
1	251 $k\Omega$	176 $k\Omega$	891 $k\Omega$	794 $k\Omega$
2	145 $k\Omega$	70 $k\Omega$	316 kΩ	501 $k\Omega$
3	794 $k\Omega$	187 $k\Omega$	631 $k\Omega$	1.26 $M\Omega$

Furthermore, the real resistance measured between the working electrode and the counter electrode is larger than the calculated values. Especially for chip design 3, the measured value is more than four times than the calculated value. The calculated resistances between WE and RE is comparable, while the measured value of chip 1 is much larger than chip 2. These may be caused by the variations in fabrication process which make the cross-section of the frit channels smaller, so that the real resistance will be larger. The simplified network model of the frit channel system may also be a reason of the inconsistency.

The conversion efficiency forferrocyanide/ferricyanide are shown in Table 5-5 for the three different chip designs. Chip design 1 and 2 which all show clear oxidation and reduction peaks in their cyclic voltammograms both have conversion efficiencies higher than 90%. On the other hand, chip design 3 which shows the most ohmic behavior in the cyclic voltammogram has a lower conversion efficiency of less than 80%, which suggest not all part of the WE surface participated in the conversion reactions. Compared with the layout of design 3 (Figure 5-17), about 1600 μm length WE channel is not connected with frit channels. Thus, the lower conversion efficiency may be caused by this part of electrode or the relatively high ohmic drop which leads to only parts of the WE participated in the reactions.

Table 5-5: Comparison of the conversion efficiency of three chip designs.

Design	Oxidation efficiency	Reduction efficiency
1	93%	93%
2	94%	84%
3	73%	79%

5.3 Measurement results of the mixer

The performance of the mixer was tested with fluorescein using the setup and protocols in appendix [A] by Linda. Van der Hout. The fluorescence intensity across the channel width at the end of the mixer is measured to calculate the mixing efficiency. The mixing efficiency at different flow rate is shown in Table 6. The experiments show the mixer can realize an almost complete mixing at flow rate from 0.5 $\mu L/min$ up to 4 $\mu L/min$ which is consistent with the simulation result.

Table 5-6: Mixing efficiency of the mixer at different flow rates.

Inlet 1-Fluorescein ($\mu L/min$)	Inlet 2-Water ($\mu L/min$)	Efficiency (%)
0.5	0.5	97.221
1	1	99.512
2	2	99.800
4	4	96.626

6. Conclusions and recommendations

6.1 Conclusion

In the introduction part of this report, three research goals were formulated. Most work under the three research goals were finished and satisfying results were achieved.

Different components used to realize on-chip phase I and phase II drug metabolism are designed and fit in a microchip of 2 cm × 1.5 cm area. Electrochemical cell used for phase I drug metabolism is designed in three different patterns, with different geometries of frit channel system which aimed to reduce the ohmic drop and increase the conversion efficiency of the chip. A 3D split-recombine mixer is designed downstream the working electrode for study of phase II reactions. Flow resistors used to realize equal flow speed of the working electrode and the counter electrode, as well as microfilters for preventing channel blockage are also integrated in the chip.

The chips based on both platinum electrodes and boron-doped electrodes were fabricated. The platinum electrodes were sputtered on Borofloat glass wafer, while the BDD electrodes were shaped by reactive ion etching on a commercial available BDD-on-insulator-silicon wafer. The three-dimensional structure of the microfluidic components on the chip are realized by taking advantage of two fluidic layers. One of the fluidic layer is dry etched on glass wafer, while the other one is made of SU8-5 by lithography and development. The two fluidic layers were bonded to seal the channels. The platinum chips are fabricated to fully functional devices, while only the electrode fabrication step is processed for BBD chips due to the limited time. Reactive ion etching of BDD electrodes are successful which is proved by resistivity measurements.

The electrochemical behavior of the platinum chip in all three designs were tested via cyclic voltammetry, and differential pulse voltammetry. The impedances between each two of the three electrodes were measured to explain the cell behavior, compared with the theoretical calculations. UV/vis measurements were also conducted for studying the chemical conversion efficiency of the cell. Chip design 1 (with parallel working electrode and counter electrode) and design 2 (with anti-parallel WE and CE) all show the typical behavior of a reversible redox couple, while design 3 shows more ohmic behavior in the system. Both chip 1 and chip 2 have a conversion efficiency higher than 90%, while, design chip 3 has a conversion efficiency lower than 80% which indicates only part of the working electrode took part in the reactions. An almost complete mixing up to flow rate of 4 $\mu L/min$ is realized by the 3D split-recombine mixer which is proved both in COMSOL simulation and fluorescence microscopy measurements.

6.2 Recommendations for future research

Due to the limited project time, the equivalent circuits and ohmic drops are not fully analyzed in all three designs. In the future work, more precise equivalent circuits of three different EC cells can be studied. The different values of R_1, R_2 and R_{frit} in three designs should be considered in finding the approximation of the circuit and the ohmic drop. An calibration measurement of the peak separation in the cyclic voltammogram of ferro/ferricyanide redox couple on platinum working electrode with platinum pseudo-reference electrode using the same test solution is needed for determination of the ohmic drop.

As discussed in Chapter 5.1.1, the variations in fabrication processes, like the reactive ion etching of the glass channels may influence the dimensions of the frit channels, causing a disparity between the real resistance and the calculated resistance of the frit channels which may undermine the function of the EC cell. The height of the SU8 channels should also be measured in the future fabrication. Although the theoretical height of SU8 coated at a specific spin speed is know from the manual, the real height after development may be influenced by many environmental factors like baking temperatures which will further influence the channel dimensions. According to these variations in the fabrication, the dimensions of the frit channels can be adjusted in the design phase to compensate for these factors.

Another issue countered is that although the platinum chip performs well at the beginning of the experiments, the performance of the chip degraded after days of working with odd peaks and extremely high peak current as shown in appendix [A] which may be caused by fouling on the electrode surface or delamination of titanium layer under platinum. Chips made of boron-doped diamond electrodes will be a promising alternative as BDD shows less adsorption and fouling than platinum electrodes[53]. The larger potential window of BDD will also give possibility to test more drug compounds in the future. However, the surface termination groups of BDD electrode will influence the electrochemical performance of BDD as discussed in chapter 2. Study on the pre-treatment of BDD electrodes is another main issue in the future work.

7. References

1. Shukla, S.J., et al., *The future of toxicity testing: a focus on in vitro methods using a quantitative high-throughput screening platform.* Drug Discovery Today, 2010. **15**(23–24): p. 997-1007.
2. Odijk, M., et al., *Improved Conversion Rates in Drug Screening Applications Using Miniaturized Electrochemical Cells with Frit Channels.* Analytical Chemistry, 2012. **84**(21): p. 9176-9183.
3. Guengerich, F.P., *Common and uncommon cytochrome P450 reactions related to metabolism and chemical toxicity.* Chemical research in toxicology, 2001. **14**(6): p. 611-650.
4. Jakoby, W. and D. Ziegler, *The enzymes of detoxication.* J Biol Chem, 1990. **265**(34): p. 20715-20718.
5. Slaughter, R.L. and D.J. Edwards, *Recent advances: the cytochrome P450 enzymes.* The Annals of pharmacotherapy, 1995. **29**(6): p. 619-624.
6. Phillips, K.A., et al., *Potential role of pharmacogenomics in reducing adverse drug reactions: a systematic review.* Jama, 2001. **286**(18): p. 2270-2279.
7. Pelkonen, O., et al., *Prediction of drug metabolism and interactions on the basis of in vitro investigations.* Basic & clinical pharmacology & toxicology, 2005. **96**(3): p. 167-175.
8. Roeser, J., et al., *Electrochemical Oxidation and Cleavage of Tyrosine- and Tryptophan-Containing Tripeptides.* Analytical Chemistry, 2010. **82**(18): p. 7556-7565.
9. Odijk, M., et al., *Lab-in-a-suitcase for drug screening and proteomics applications*, in *14th International Conference on Miniaturized Systems for Chemistry and Life Sciences, ¦ÌTAS 2010*, S. Verpoorte, et al., Editors. 2010, Chemical and Biological Microstystems Society: Groningen, the Netherlands. p. 399-401.
10. Bard, A.J. and L.R. Faulkner, *Electrochemical Methods: Fundamentals and Applications*. 2000: Wiley.
11. Allen J. Bard, L.R.F., *Electrochemical Methods: Fundamentals and Applications.*
12. Wang, J., *Analytical electrochemistry*. 2006: John Wiley & Sons.
13. Linear Sweep and Cyclic Voltammetry: The principle. www.ceb.cam.ac.uk
14. Mark, D., et al., *Microfluidic lab-on-a-chip platforms: requirements, characteristics and applications.* Chemical Society Reviews, 2010. **39**(3): p. 1153-1182.
15. Squires, T.M. and S.R. Quake, *Microfluidics: Fluid physics at the nanoliter scale.* Reviews of modern physics, 2005. **77**(3): p. 977.
16. Santini Jr, J.T., et al., *Microchips as controlled drug-delivery devices.* Angewandte Chemie International Edition, 2000. **39**(14): p. 2396-2407.
17. Nguyen, N.-T. and Z. Wu, *Micromixers—a review.* Journal of Micromechanics and Microengineering, 2005. **15**(2): p. R1.
18. elveflow, Microfluidic mixers: a short review.www. elveflow.com
19. *Split and recombination micromixer based on PDMS three-dimensional microstructure.* Transducers'05: IEEE Int. Conf. on Sensors and Actuators Tech. Digest, 2005: p. 1533.
20. Ottino, J.M., *The kinematics of mixing: stretching, chaos, and transport*. Vol. 3. 1989: Cambridge University Press.
21. Wang, H., et al., *Numerical investigation of mixing in microchannels with patterned grooves.* Journal of Micromechanics and Microengineering, 2003. **13**(6): p. 801.
22. Wong, S.H., et al., *Investigation of mixing in a cross-shaped micromixer with static mixing elements for reaction kinetics studies.* Sensors and Actuators B: Chemical, 2003. **95**(1): p. 414-424.
23. Liu, Y.Z., B.J. Kim, and H.J. Sung, *Two-fluid mixing in a microchannel.* International journal of heat and fluid flow, 2004. **25**(6): p. 986-995.
24. Pletcher, D. and R.S.o. Chemistry, *A First Course in Electrode Processes*. 2009: Royal Society of Chemistry.

25. Santos da Silva, I., et al., *Strategies to avoid electrode fouling for nimesulide detection using unmodified electrodes.* Analytical Methods, 2013. **5**(14): p. 3546-3551.
26. Bard, A.J. and L.R. Faulkner, *Electrochemical methods: fundamentals and applications*. 1980: Wiley.
27. Haenni, W., et al., *Industrial applications of diamond electrodes.* Semiconductors and Semimetals, 2004. **77**: p. 149-196.
28. Swain, G.M., A.B. Anderson, and J.C. Angus, *Applications of Diamond Thin Films in Electrochemistry.* MRS Bulletin, 1998. **23**(09): p. 56-60.
29. Panizza, M. and G. Cerisola, *Application of diamond electrodes to electrochemical processes.* Electrochimica Acta, 2005. **51**(2): p. 191-199.
30. Kraft, A., *Doped Diamond: A Compact Review on a New, Versatile Electrode Material.* International Journal of Electrochemical Science, 2007.
31. Kraft, A., *Doped diamond: a compact review on a new, versatile electrode material.* Int. J. Electrochem. Sci, 2007. **2**(5): p. 355-385.
32. Martin, H.B., et al., *Voltammetry Studies of Single‐Crystal and Polycrystalline Diamond Electrodes.* Journal of the Electrochemical Society, 1999. **146**(8): p. 2959-2964.
33. M.Odijk, *Ph.D thesis*, 2011, University of Twente.
34. E.Oosterbroek, *Ph.D thesis*, 1999, University of Twente.
35. Davis, M.L. and S.J. Masten, *Principles of Environmental Engineering and Science*. 2004: McGraw-Hill Higher Education.
36. Mengeaud, V., J. Josserand, and H.H. Girault, *Mixing Processes in a Zigzag Microchannel: Finite Element Simulations and Optical Study.* Analytical Chemistry, 2002. **74**(16): p. 4279-4286.
37. Kirby, B.J., *Micro- and Nanoscale Fluid Mechanics: Transport in Microfluidic Devices*. 2010: Cambridge University Press.
38. Erickso, D. and D. Li, *Microscale Flow and Transport Simulation for Electrokinetic and Lab-on-Chip Applications*, in *BioMEMS and Biomedical Nanotechnology*, M. Ferrari, R. Bashir, and S. Wereley, Editors. 2007, Springer US. p. 277-300.
39. Panton, R.L., *Incompressible Flow*. 1996: Wiley.
40. Jeon, N.L., et al., *Generation of Solution and Surface Gradients Using Microfluidic Systems.* Langmuir, 2000. **16**(22): p. 8311-8316.
41. Wang, W. and S.A. Soper, *Bio-MEMS: Technologies and Applications*. 2006: Taylor & Francis.
42. *MicroChemical TI 35ES technical data sheet.* 10/2003.
43. Franssila, S., *Introduction to Microfabrication*. 2004: Wiley.
44. GUIDINI, V.O., S.A. MOSHKALYOV, and P.J. TATSCH. *Deep dry etching of silicon using Bosch type process*. in *Proceedings-Electrochemical Society*. 2004. Electrochemical Society.
45. Bilenberg, B., et al., *PMMA to SU-8 bonding for polymer based lab-on-a-chip systems with integrated optics.* Journal of Micromechanics and Microengineering, 2004. **14**(6): p. 814.
46. Feng, R. and R.J. Farris, *Influence of processing conditions on the thermal and mechanical properties of SU8 negative photoresist coatings.* Journal of Micromechanics and Microengineering, 2003. **13**(1): p. 80.
47. Wiemer, M., et al. *Wafer bonding with BCB and SU-8 for MEMS packaging*. in *Electronics Systemintegration Technology Conference, 2006. 1st*. 2006. IEEE.
48. Serra, S., et al. *A simple bonding process of SU-8 to glass to seal a microfluidic device*. in *Proc. 3rd Int. Conf. on Multi-Material Micro Manufacture (Borovets, 3–5 Oct. 2007)*. 2007.
49. Hout, L.v.d., *De karacterisatie van een microfluidische mixer, voor het nabootsen van fase 2 medicijnmetabolisme.* Bacheloropdracht, 2014.
50. Vielstich, W., *Cyclic voltammetry*. 2010: Wiley Online Library.
51. Odijk, M., et al., *A microfluidic chip for electrochemical conversions in drug metabolism studies.* Lab on a Chip, 2009. **9**(12): p. 1687-1693.
52. Mirčeski, V. and M. Lovrić, *Ohmic drop effects in square-wave voltammetry.* Journal of Electroanalytical Chemistry, 2001. **497**(1–2): p. 114-124.

53. Roeser, J., et al., *Boron-Doped Diamond Electrodes for the Electrochemical Oxidation and Cleavage of Peptides.* Analytical Chemistry, 2013. **85**(14): p. 6626-6632.

8. Appendix

A. Measurements

A.1 Electrochemical measurements of chip design 1.

On the first day of measurements, the chip shows a clear redox behavior in CV

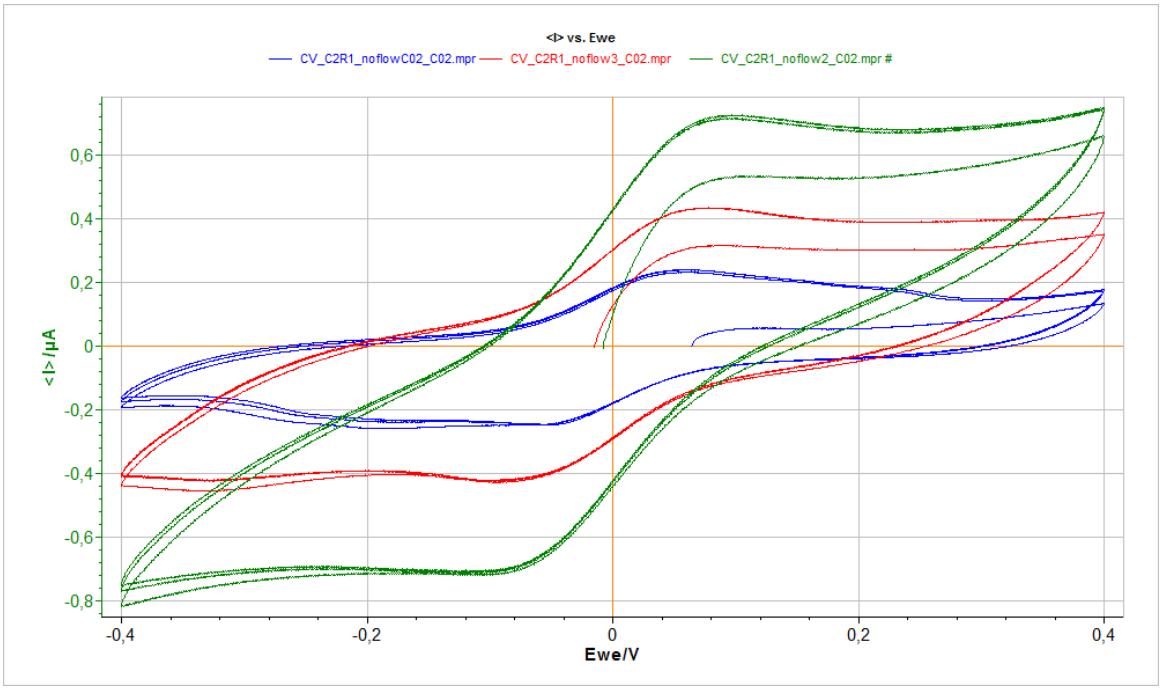

Figure 8-1: Cyclic voltammetry measurement of the chip design 1 at a flow rate of 0 $\mu L/min$ at scan rates of 10 mV/s (blue) , 30 mV/s (red), and 100 mV/s (green)

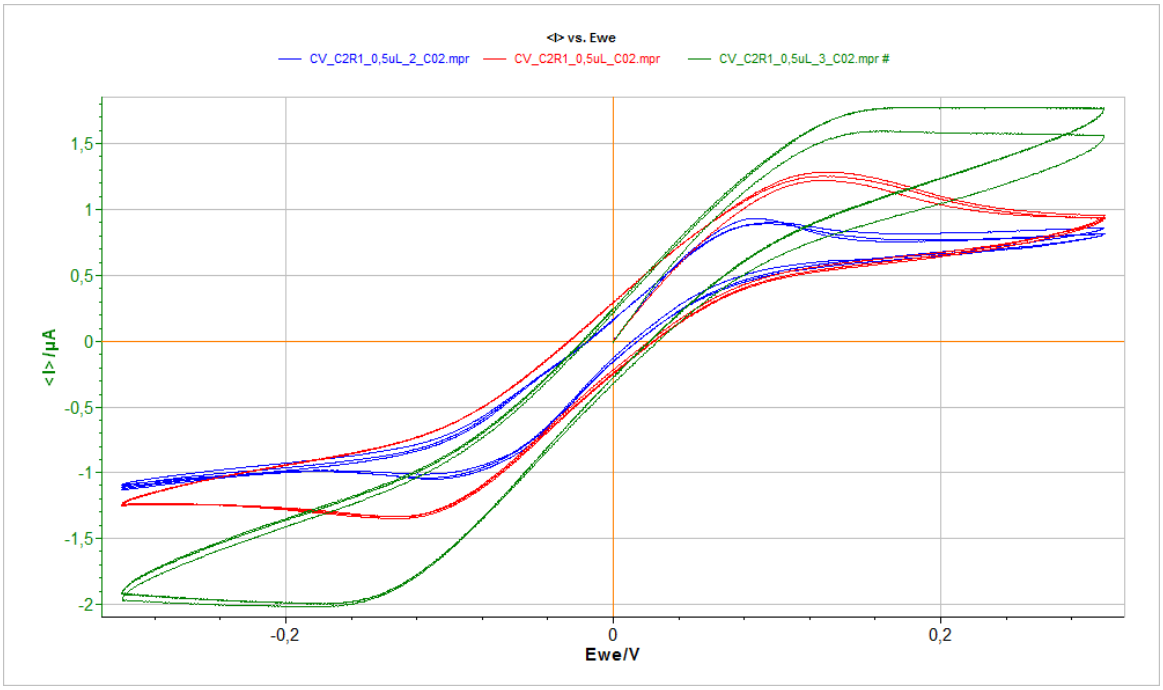

Figure 8-2 Cyclic voltammetry measurement of the chip design 1 at a flow rate of 0.5 $\mu L/min$ at scan rates

of 10 mVs (blue) , 30 mV/s (red), and 100 mV/s (green)

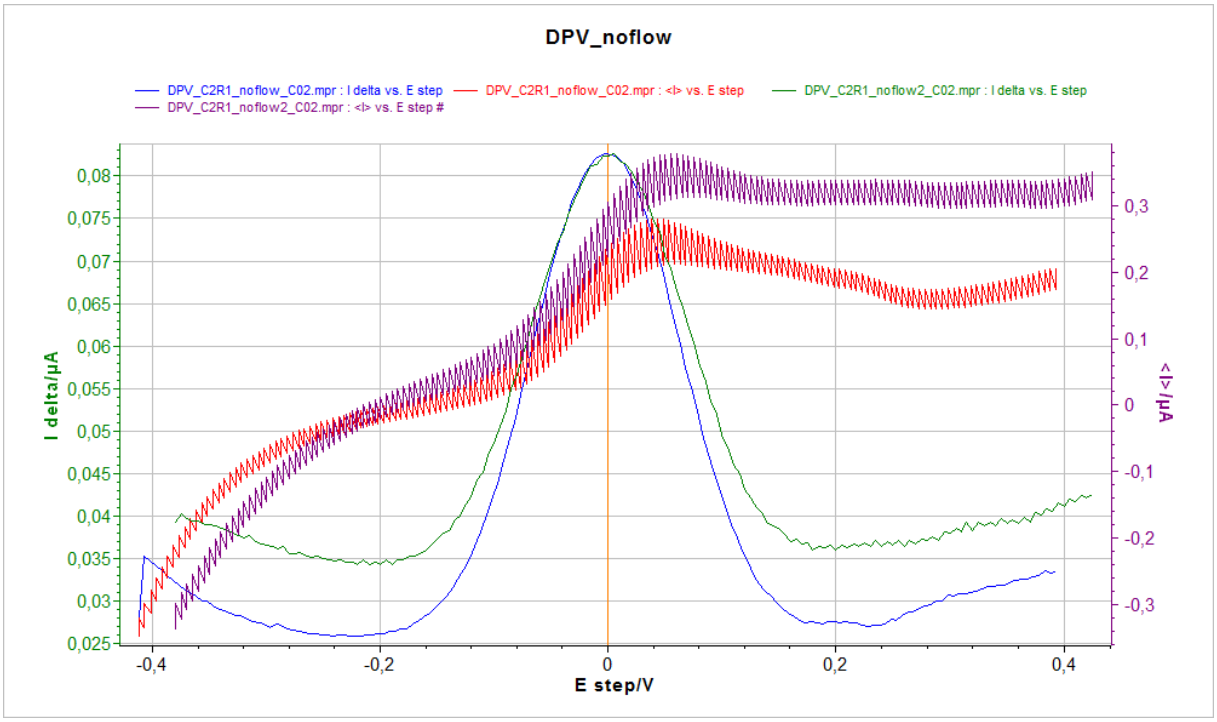

Figure 8-3: Differential pulse voltammetry measurement of design 1 with pulses width of 100 ms (blue) and 50 ms (green).

On the second day of measurements, the measuring result is not consistent with what measured in the first day.

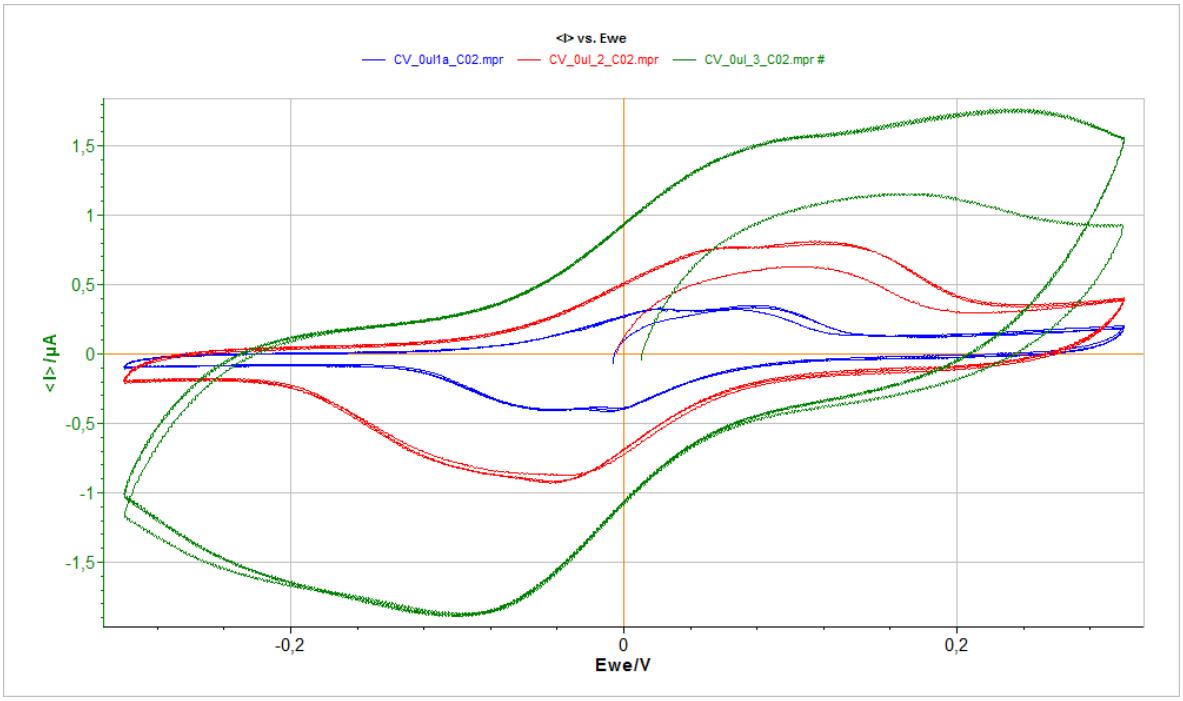

Figure 8-4 Cyclic voltammetry measurement of design 1 at a flow rate of 0 $\mu L/min$ at scan rates of 10 mV/s (blue) , 30 mV/s (red), and 100 mV/s (green) on Day2

The DPV measurements is also worse than the first day.

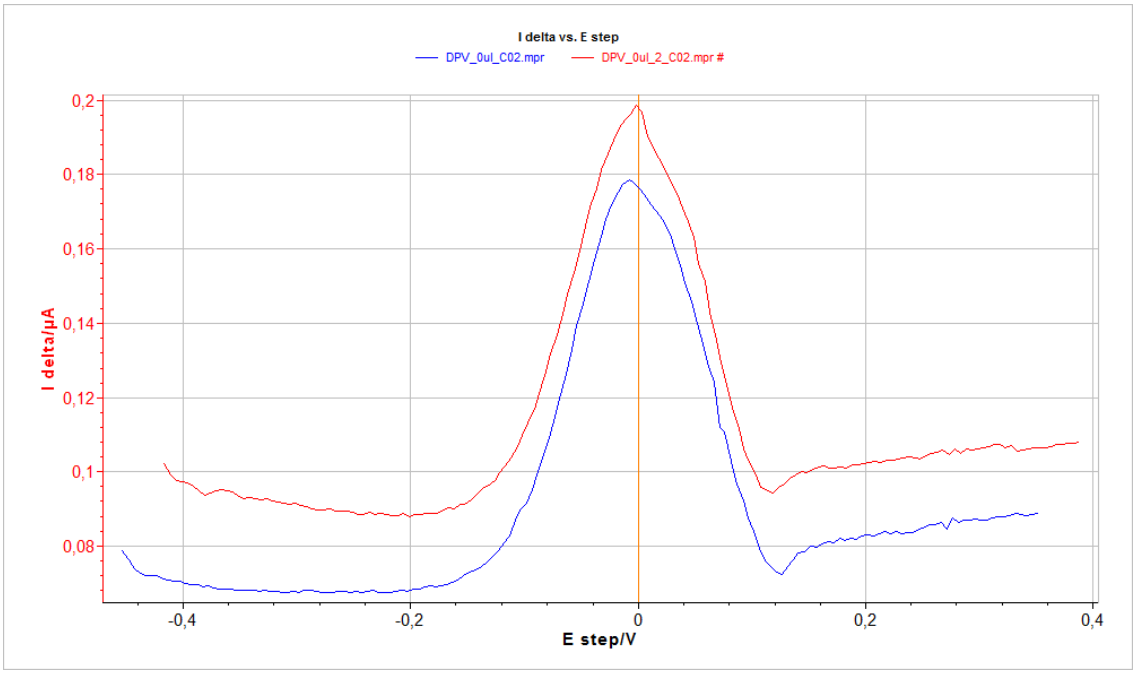

Figure 8-5 Differential pulse voltammetry measurement of design 1 with pulses width of 100 ms (blue) and 50 ms (green) at flow rate of 0 $\mu L/min$ on Day 2.

Impedance measurement results are shown below.

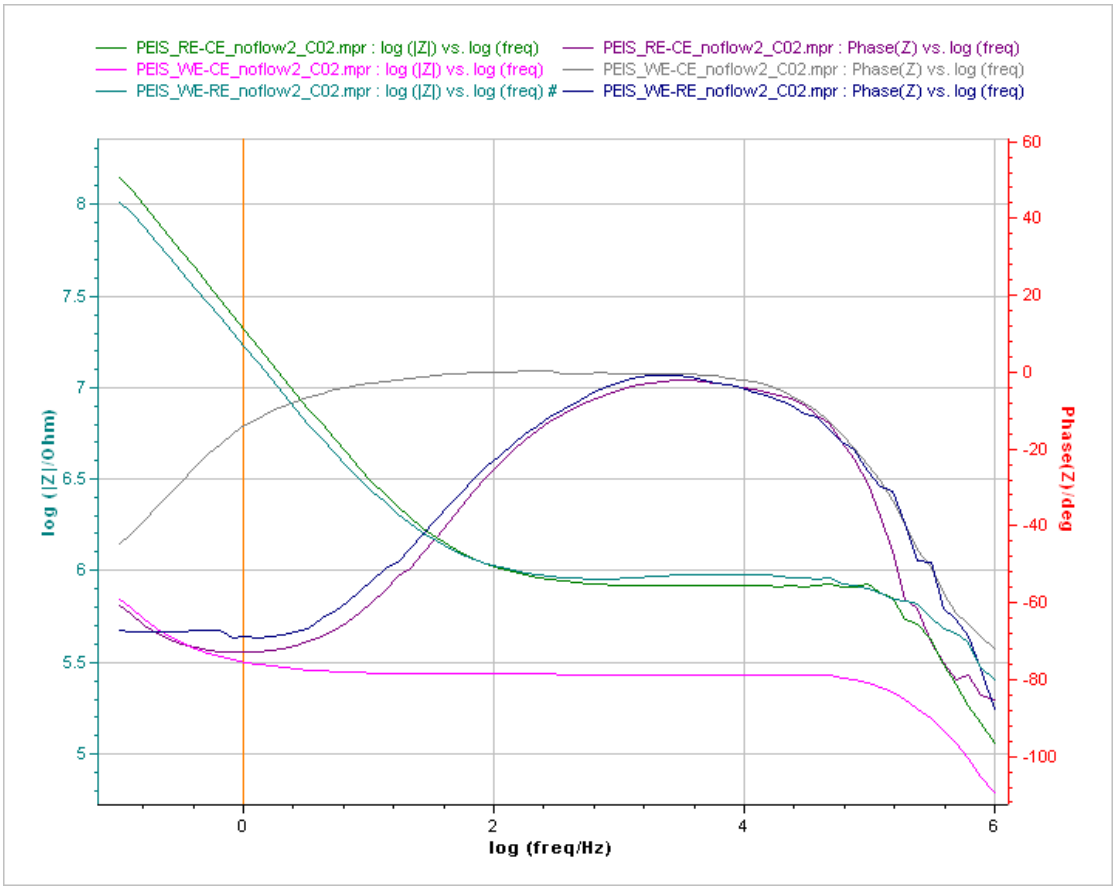

Figure 8-6 Impedance measured between WE/CE, WE/RE, and WE/CE of design 1

A.2 Electrochemical measurements of chip design 2

Cyclic voltammetry measurements of two new chips on the first day

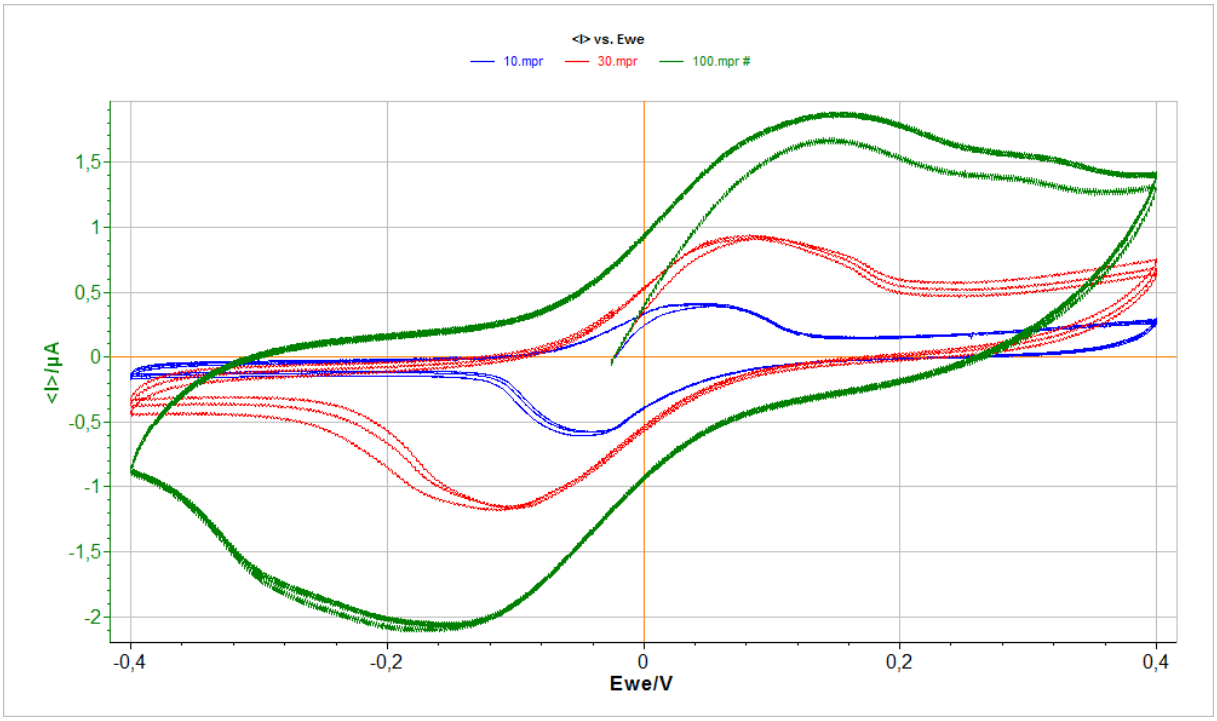

Figure 8-7 Cyclic voltammetry measurement design 2 chip A at a flow rate of 0 $\mu L/min$ at scan rates of 10 mV/s (blue) , 30 mV/s (red), and 100 mV/s (green) on Day1

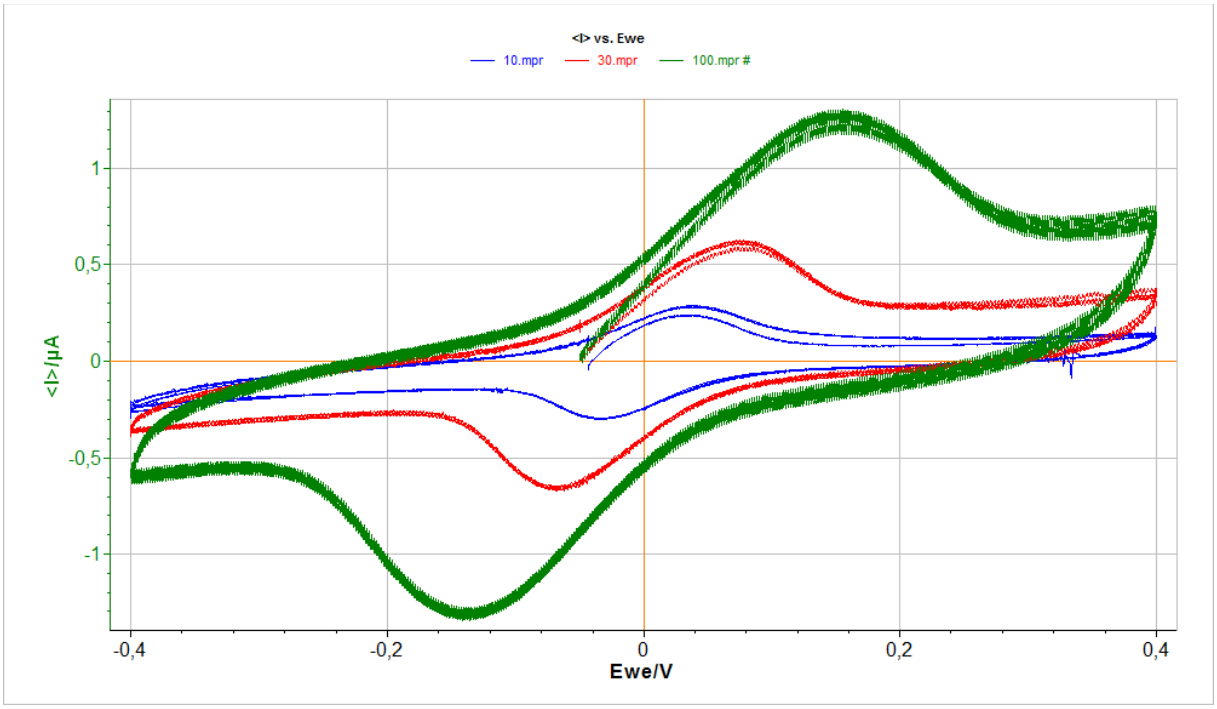

Figure 8-8 Cyclic voltammetry measurement design 2 chip B at a flow rate of 0 $\mu L/min$ at scan rates of 10 mV/s (blue) , 30 mV/s (red), and 100 mV/s (green) on Day1

On the fifth day of measuring, the result is strange.

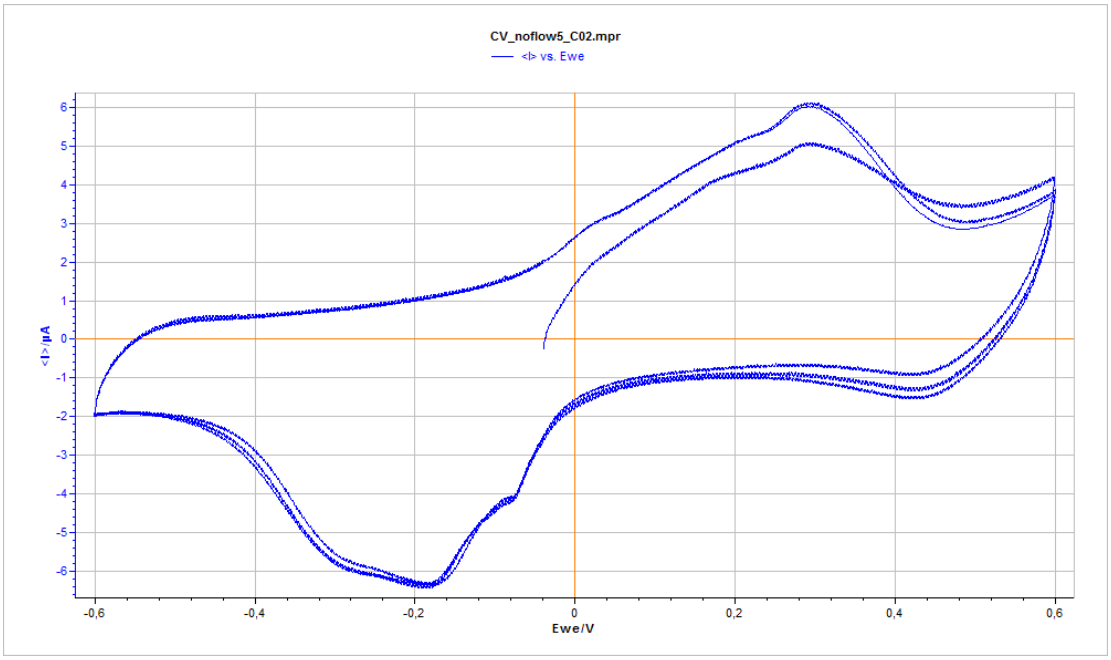

Figure 8-9 Cyclic voltammetry measurement of the chip design 2 at a flow rate of 0 $\mu L/min$ at scan rate of 100 mV/s on the fifth day. Two reduction peaks are observed. The potential at oxidation peak is extremely large.

Differential pulse voltammetry measurements are shown below.

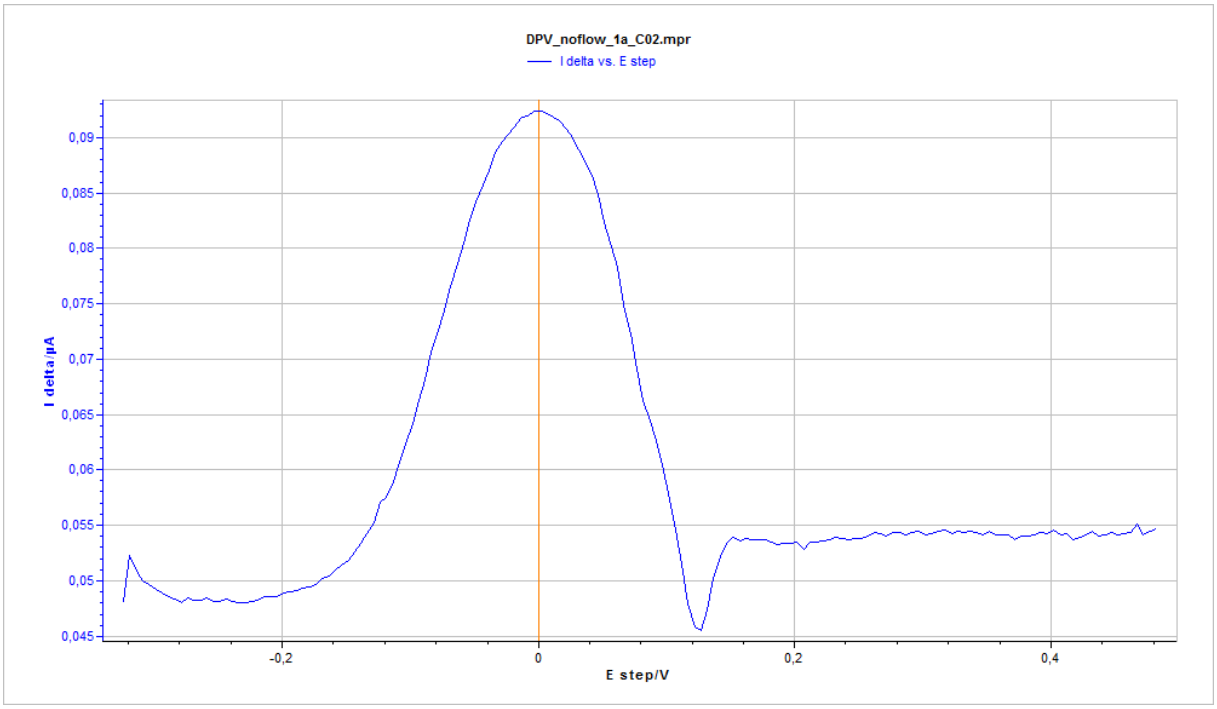

Figure 8-10 Differential pulse voltammetry measurement of design 2 with pulses width of 100 ms at flow rate of 0 $\mu L/min$.

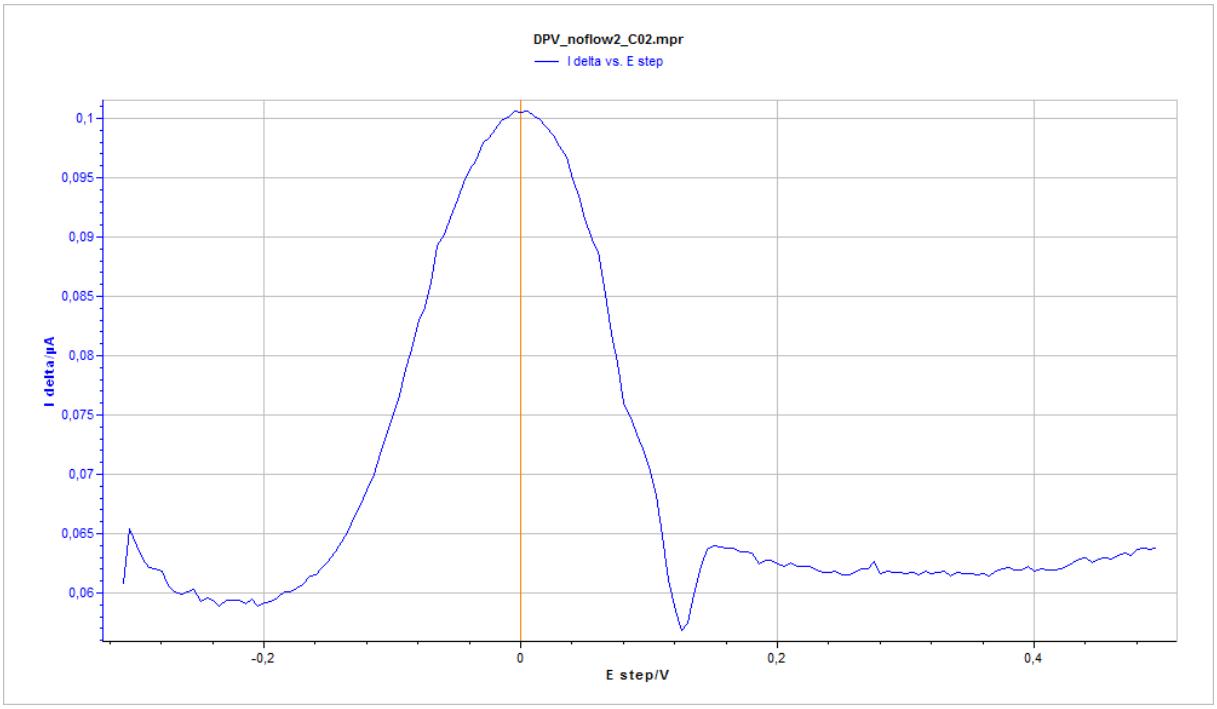

Figure 8-11 Differential pulse voltammetry measurement of design 2 with pulses width of 50 ms at flow rate of 0 $\mu L/min$.

Impedance measurements are shown below.

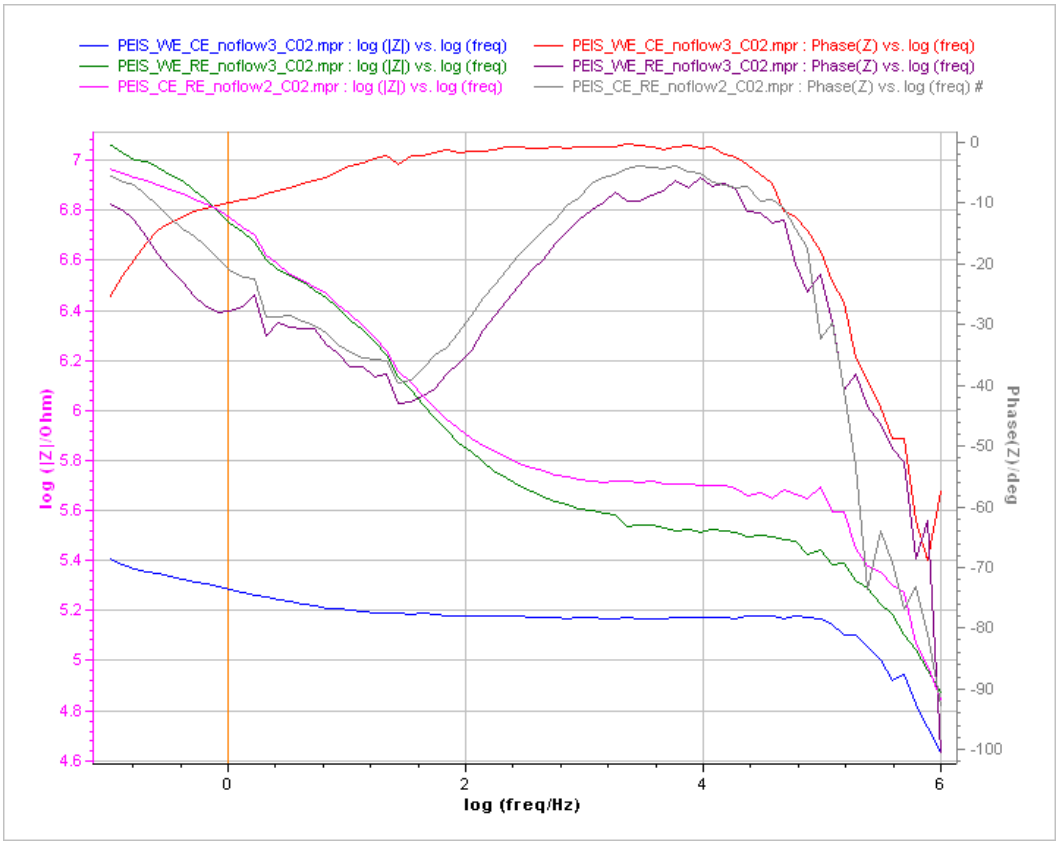

Figure 8-12 Impedance measured between WE/CE, WE/RE, and WE/CE of design 2.

A.3 Electrochemical measurements of chip design 3

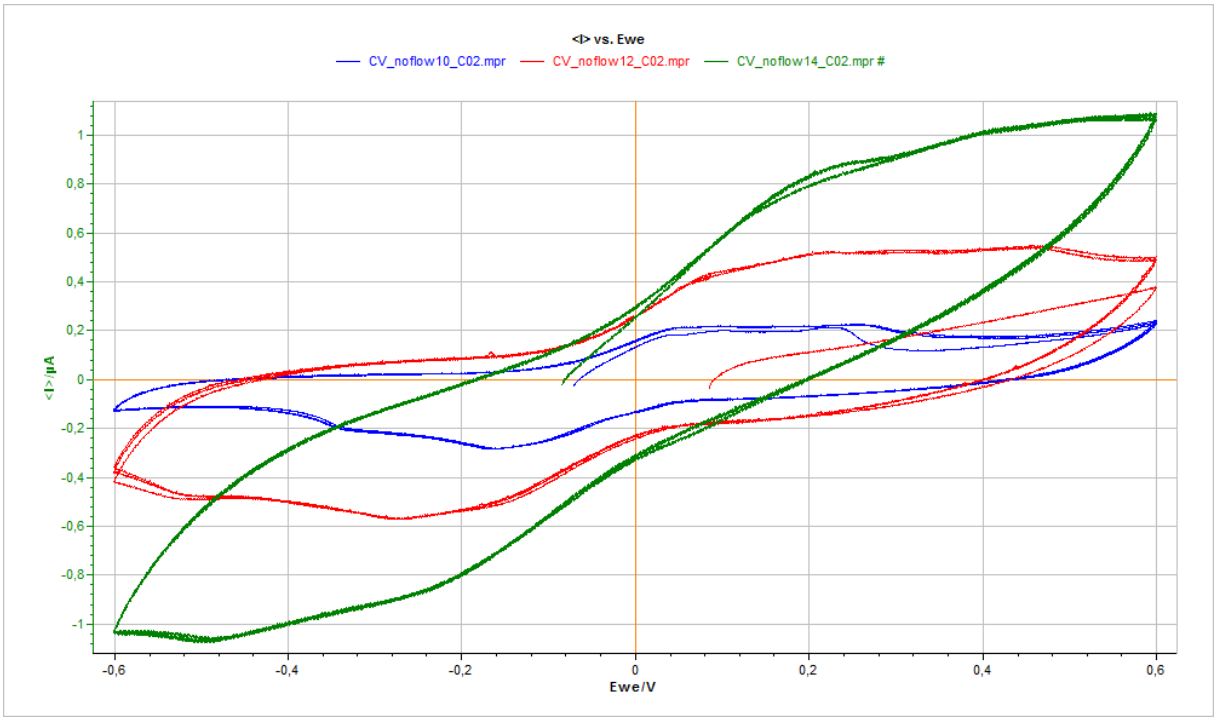

Figure 8-13 Cyclic voltammetry measurement design 3 chip A at a flow rate of 0 $\mu L/min$ at scan rates of 10 mV/s (blue) , 30 mV/s (red), and 100 mV/s (green) on Day1

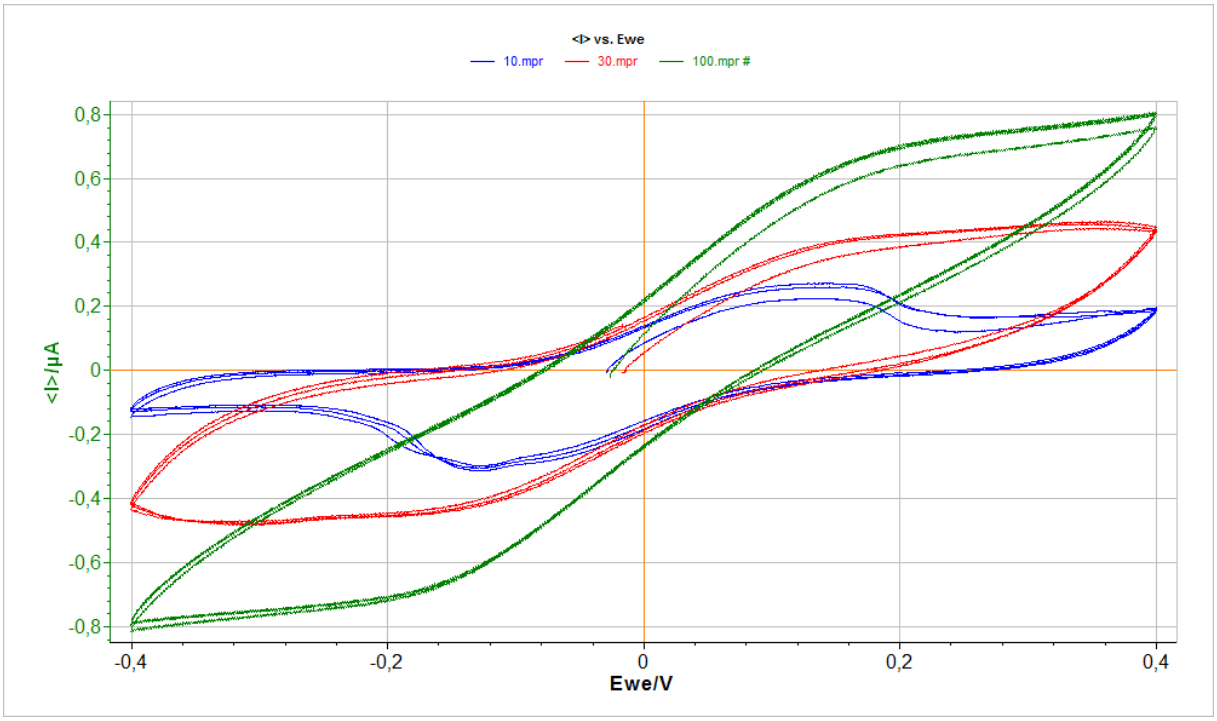

Figure 8-14 Cyclic voltammetry measurement design 3 chip B at a flow rate of 0 $\mu L/min$ at scan rates of 10 mV/s (blue) , 30 mV/s (red), and 100 mV/s (green) on Day1

Impedance measurements are shown below:

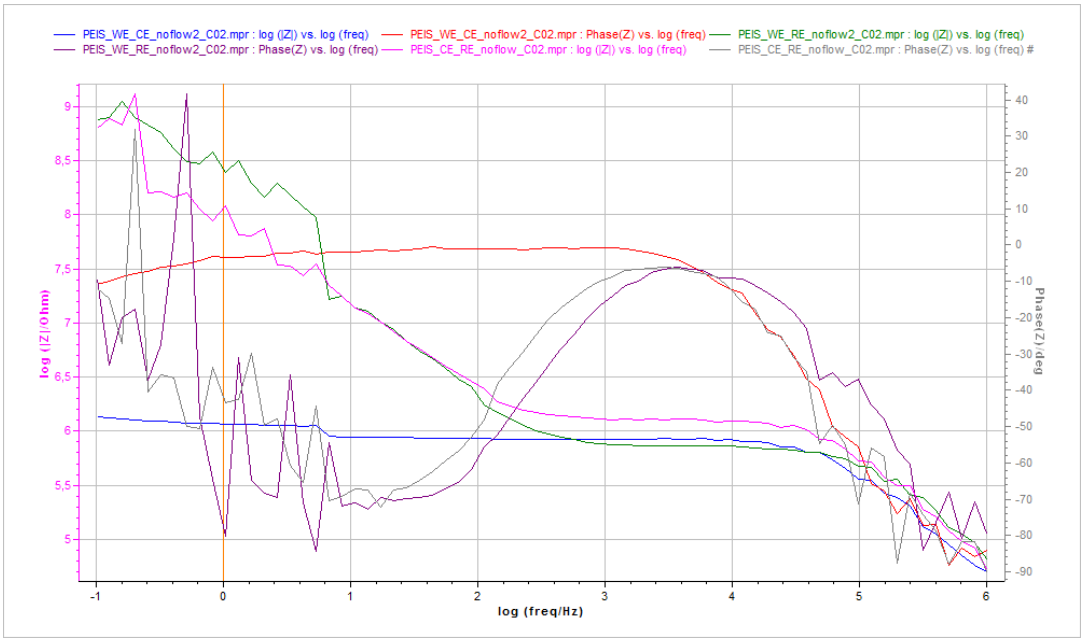

Figure 8-15 Impedance measurement between WE/CE, WE/RE,CE/RE of design 3.

A.4 Conversion efficiency measurements

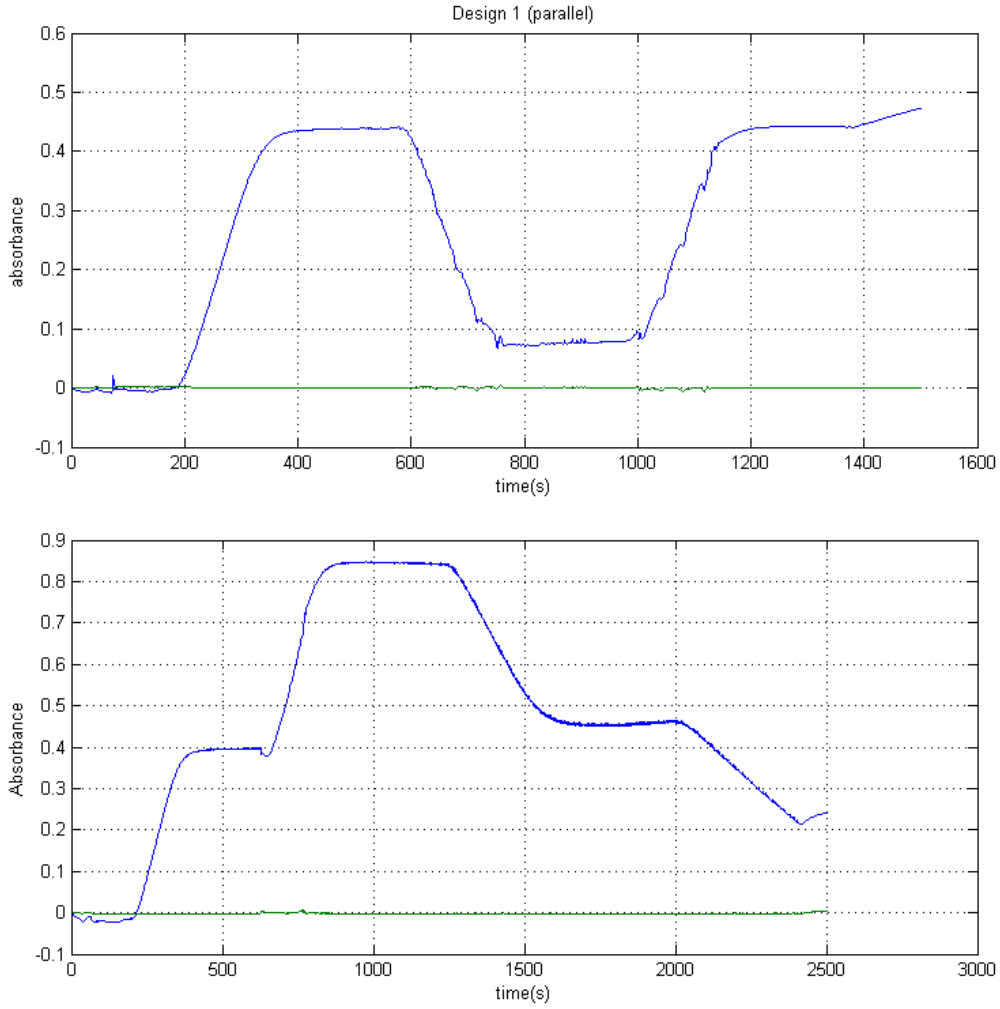

Figure 8-16 Absorbance of design 1. (top) applying reduction current, (bottom) applying oxidation peak.

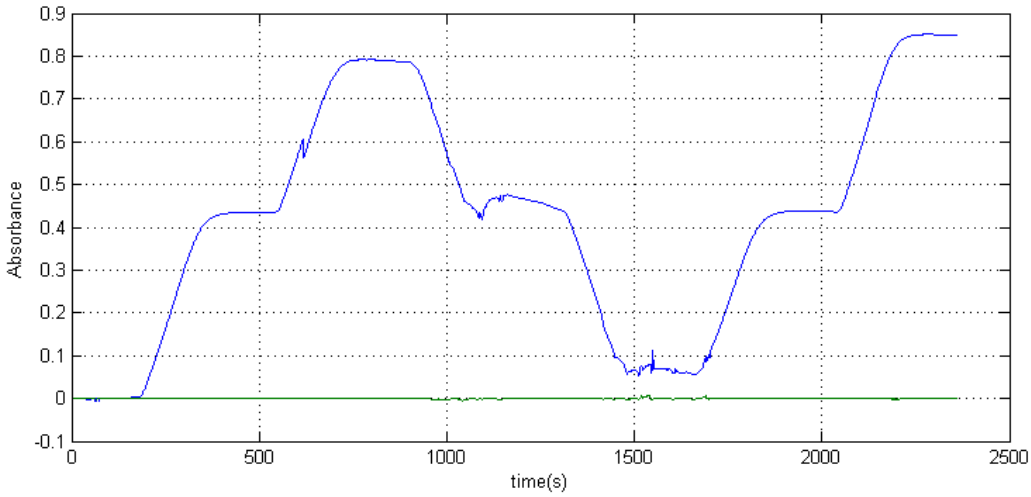

Figure 8-17 Absorbance of design 2.

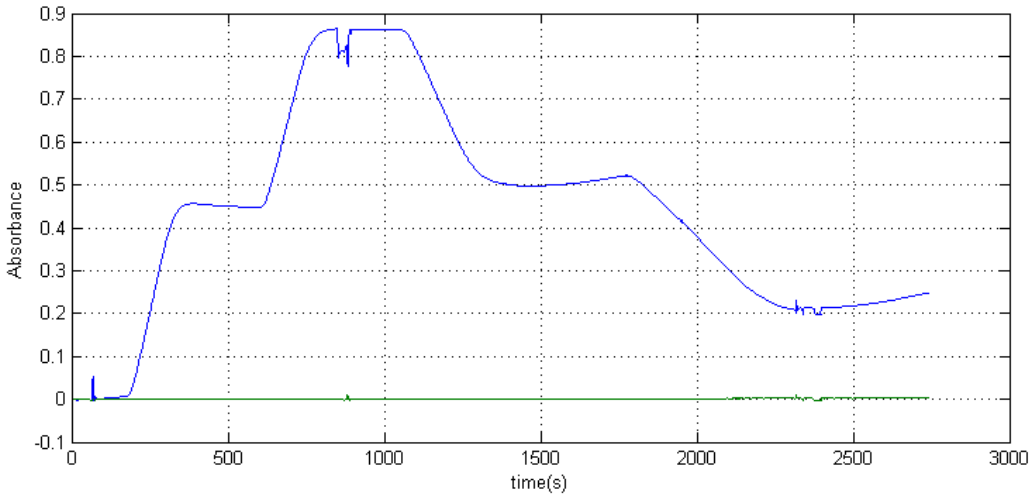

Figure 8-18 Absorbance of design 3.

B. Characterization of the mixer

The experiment is operated on a fluorescence microscope (Leica DMI 5000M) equipped with filter (Leica BGR). The chip is put on the working stage of the microscope where illuminated by a lamp. The light emitted from the lamp goes through the fluidic channels of the chip and the filter sequentially. Only a specific wavelength of light which is emitted by the fluorescence can transmit through the filter and thus be further analyzed. The microscope is connected with a camera (Colorview II) which captures the fluorescence intensity over the channel width. Fluorescence solution of 10 mM concentration and deionized water (MilliQ) are used in the experiment. The fluidic connections for testing the mixer are shown in Figure 6.

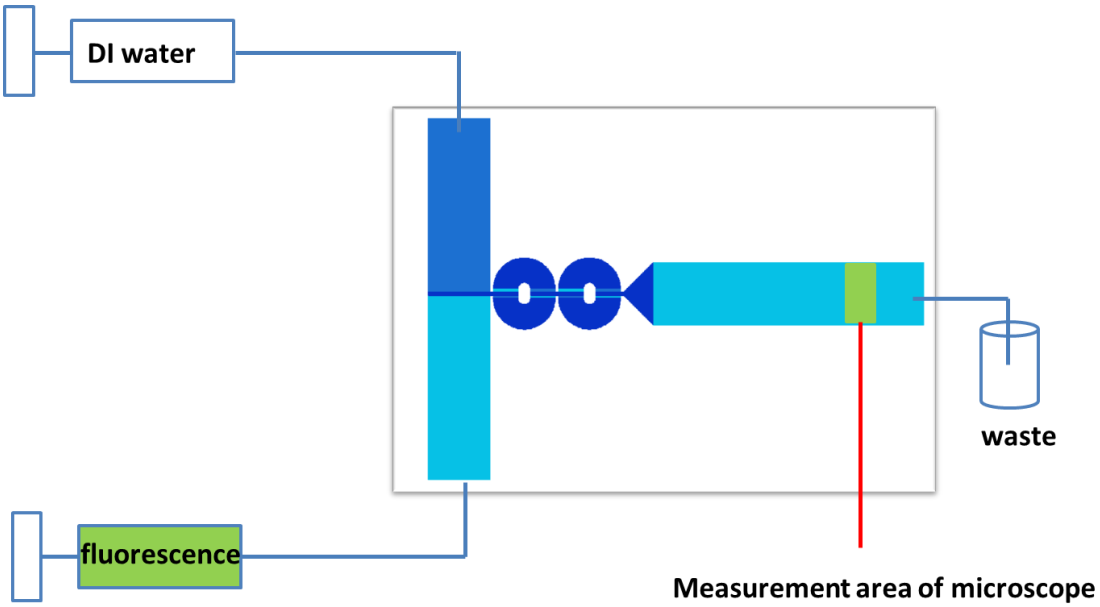

Figure 8-19 Measurement setup for characterization of the mixer.

At the beginning, both two inlets of the mixer are flowed with water for a reference measurement. After that, the measurements are performed, in which one inlet of the mixer is flowed with fluorescence solution, while the other inlet is flowed with water at the same flow rate. A group of measurements are conducted at flow rates of $0.1\mu L/min$, $0.5\mu L/min$, $1\mu L/min$, $2\mu L/min$, and $4\mu L/min$.Between each measurement, the mixer is rinsed with acetone and water to remove the remaining fluorescence in the channel.

The intensity of the light goes through the filter is determined by the fluorescence concentration across the channel width. When the mixer is only flowed with water, the light which is at a certain wavelength transmits through water and retains the same wavelength. The light is filtered out by the filter. Thus, the intensity of light captured by the camera is 0. When the mixer is flowed with fluorescence solution, fluorescence absorbs the light and emits it at a different wavelength which can transmit through the filter and captured by the camera. The different intensities of light show the different fluorescence concentrations across the channel. If the two solutions flow into the mixer are total mixed, the fluorescence concentration across the channel width is even, thus there will be no difference in intensity.

C. Processing steps

C.1 Introduction

Design description

The goal of designing and fabricating this electrochemical microfluidic chip is for use in testing the feasibility of chemical conversion and protein cleavage. The chip itself is for electrochemical oxidation of drugs which mimic the metabolic process in human body; or an alternative way of traditional enzymatic or chemical ways to cleavage proteins. The oxidized chemicals and cleaved peptides will be test in liquid chromatography or mass spectrometry in the following steps. Previous electrochemical microfluidic chips for this purpose are usually fabricated on glass platform and integrated with platinum working and counter electrodes, for its electrochemical inertness and ease of fabrication. However, the larger potential window of boron-doped diamond in aqueous electrolytes compared with platinum makes BDD promising for the purpose of our project.

The design of this chip is based on an unpublished design of Dr. Mathieu Odijk. In his design, The 30mm length working electrode and counter electrode channels are folded and well arranged in a chip of only 2cm ×1.5 cm area.

This new version of design is still based on the same chip dimension because of the limitation of the chip holder which is going to be used. Besides electrochemical electrodes used for drug conversion, new fluidic components are added to the design. Microfilters which consist of 50 ×30 5μm diameter micropillars are put in a broaden part of channel near the two chip inlet. A mixer is designed and arranged at the end of working electrode channel, so that new chemicals can be added and react with the byproducts of drugs after oxidation at the working electrode. The design of the mixer utilizes two layers of channels and was proved to be highly efficient, so that more space on the chip can be saved for the electrodes. The frit channels connecting WE and CE are redesigned to reduce the Ohmic drop between working electrode and reference electrode and realize an equal current density over WE and CE. The frit channels utilize two fluidic channels. The frit channels where two fluidic layers are used and have channel width in hundred nano meter are designed to reduce the electric resistance between WE and CE. On the other hand, the frit channels which only take use of one fluidic layer and much narrower in width are designed to realize approximately equal current density on electrodes and to prevent direct flow from WE channel to CE channel. Three different designs are going to be fabricated on one wafer. The length of the WE and CE channels of the three chips are approximately the same, but the footprint of how they arranged on chip are different which result in different length and arrangement of frit channels.

Masks

There are four masks needed in total:
Mask 1(BE): Bottom electrode etched by Reactive Ion Etching.
Mask 2(BC): Bottom channel layer
Mask 3(TC): Top channel layer
Mask 4(CP): Contact pads for BDD wafer
Mask powderblast 1(PB): Inlet and outlet in glass wafer by powder blasting.

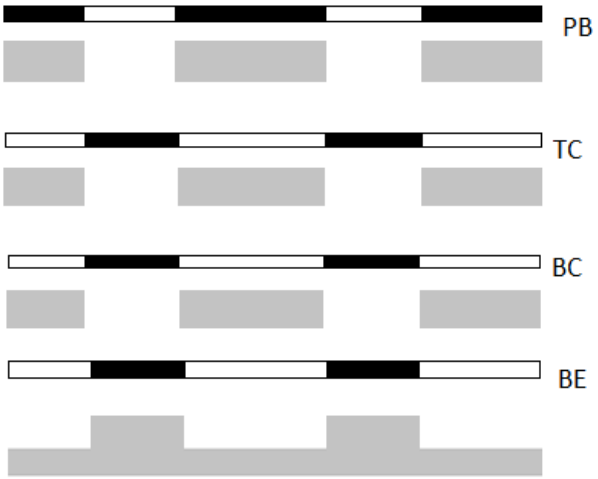

Figure 1: Illustration of the functions of all five layers in fabrication.

C.2 Mask layout(overview)

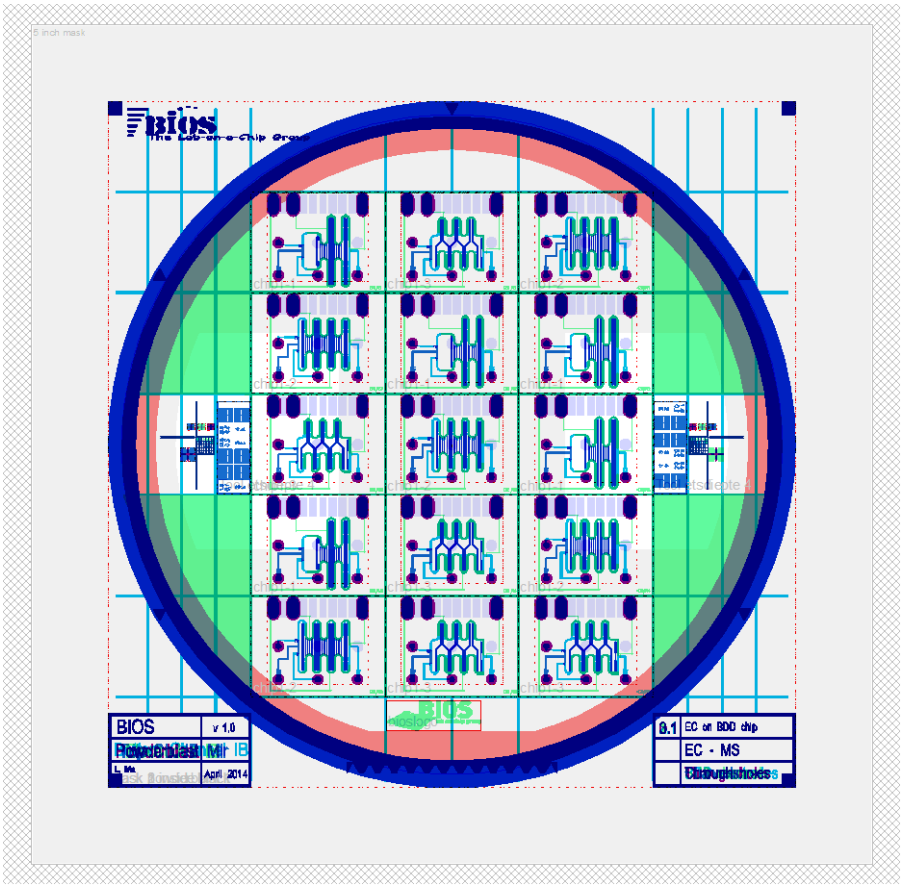

Figure 2: Overview of the total wafer including all wafers

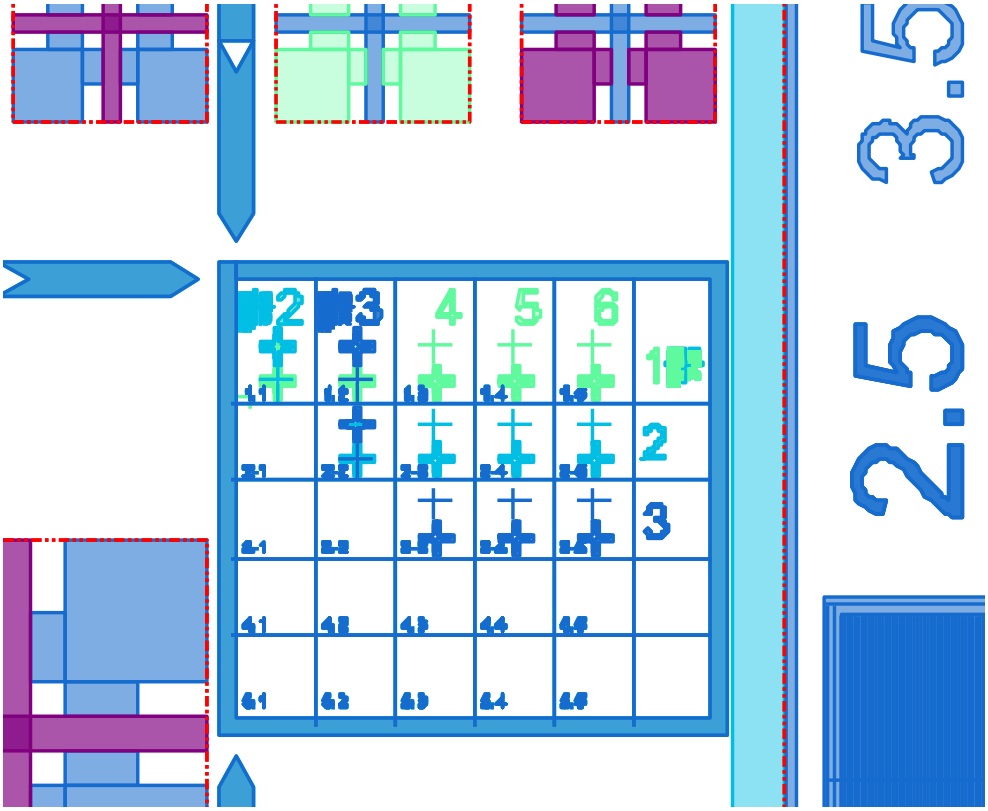

Figure 4: Zoomed view of the lithographic alignment marks.

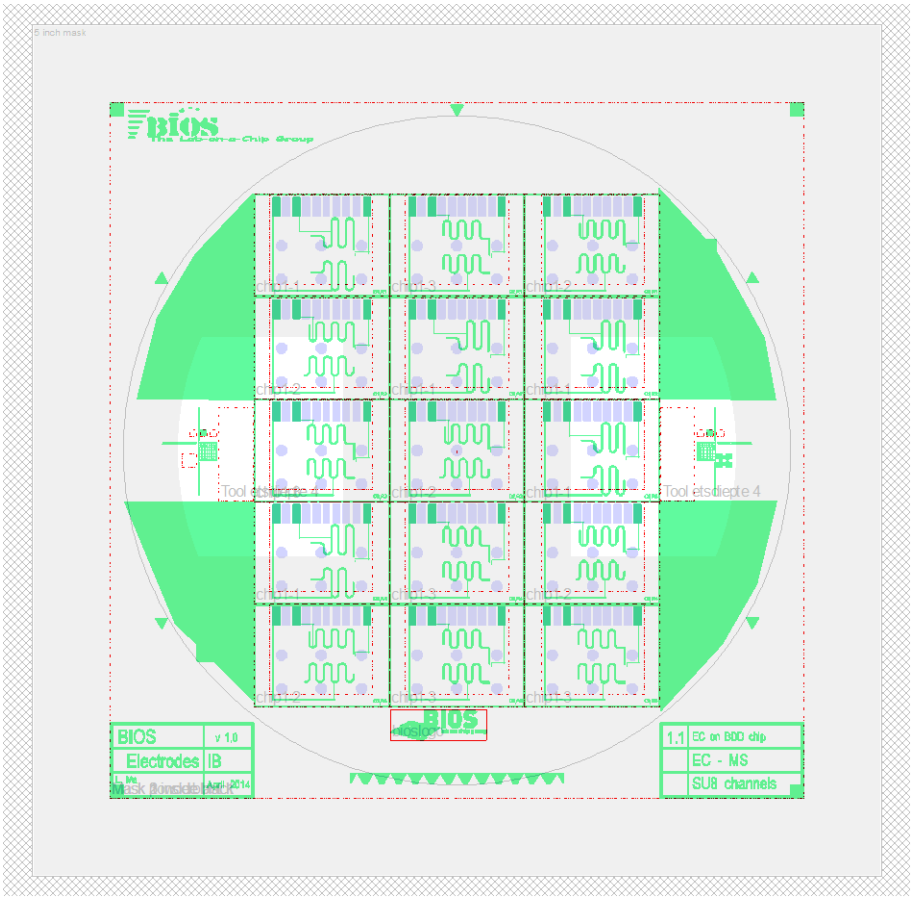

Figure 5: Mask 1; BDD electrode

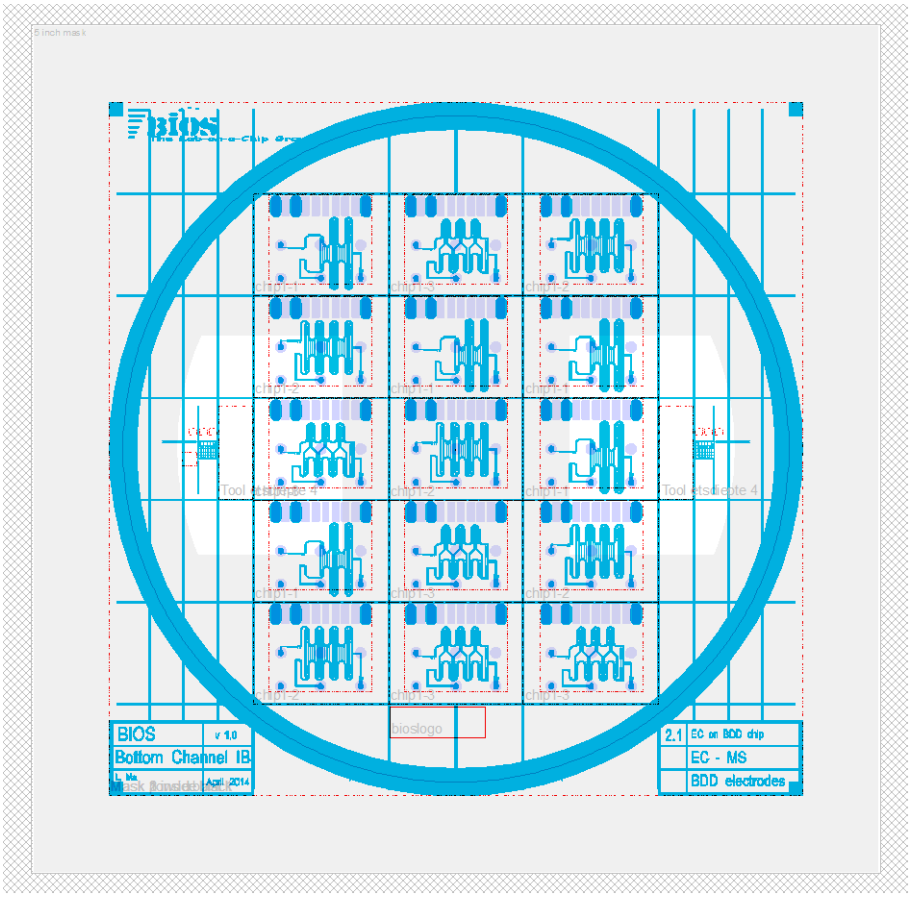

Figure 6: Mask 2; Bottom fluidic channels

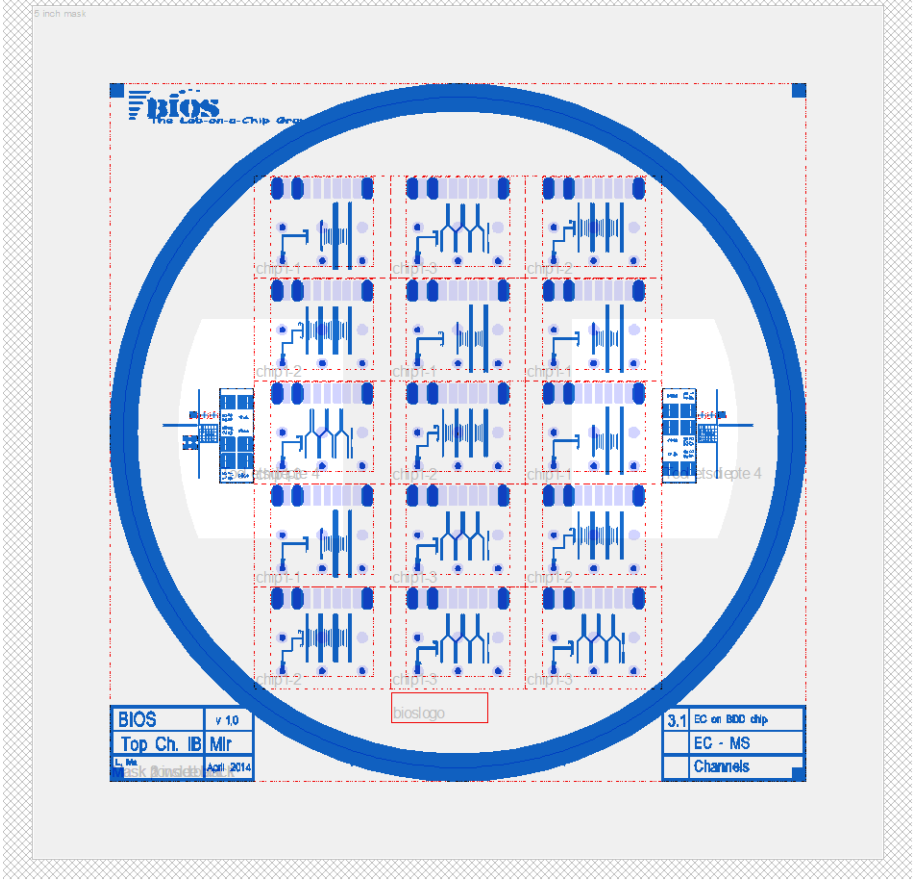

Figure 7: Mask 3; Top fluidic channels.

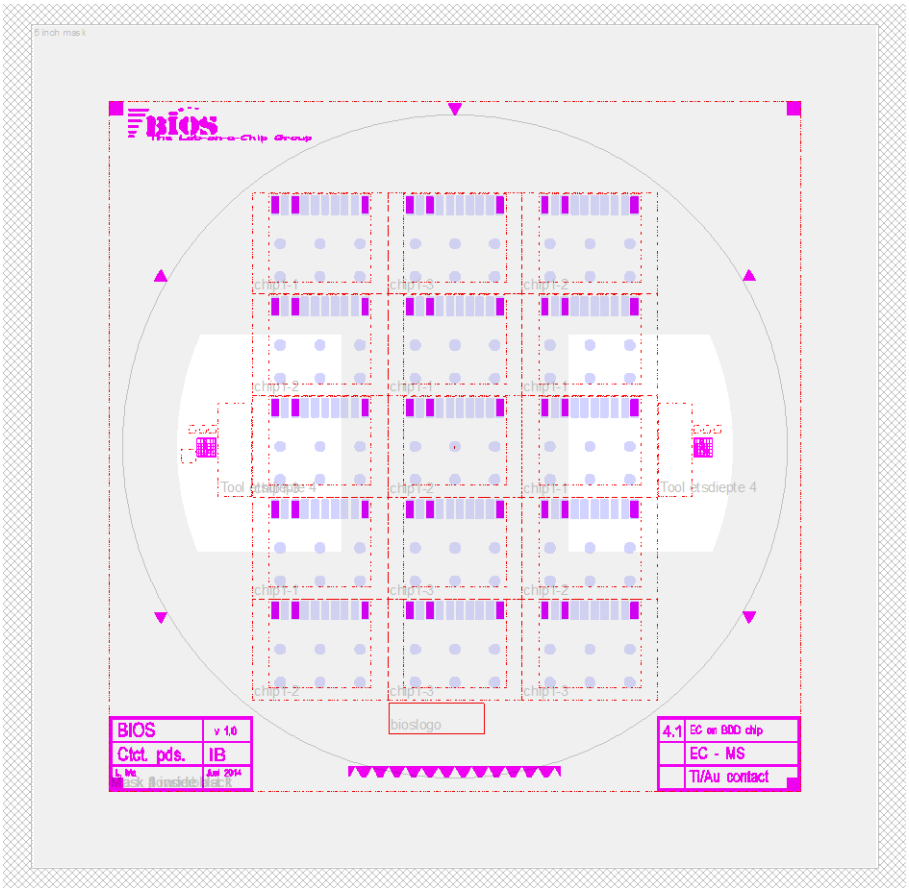

Figure 8: Mask 4;Contact pads

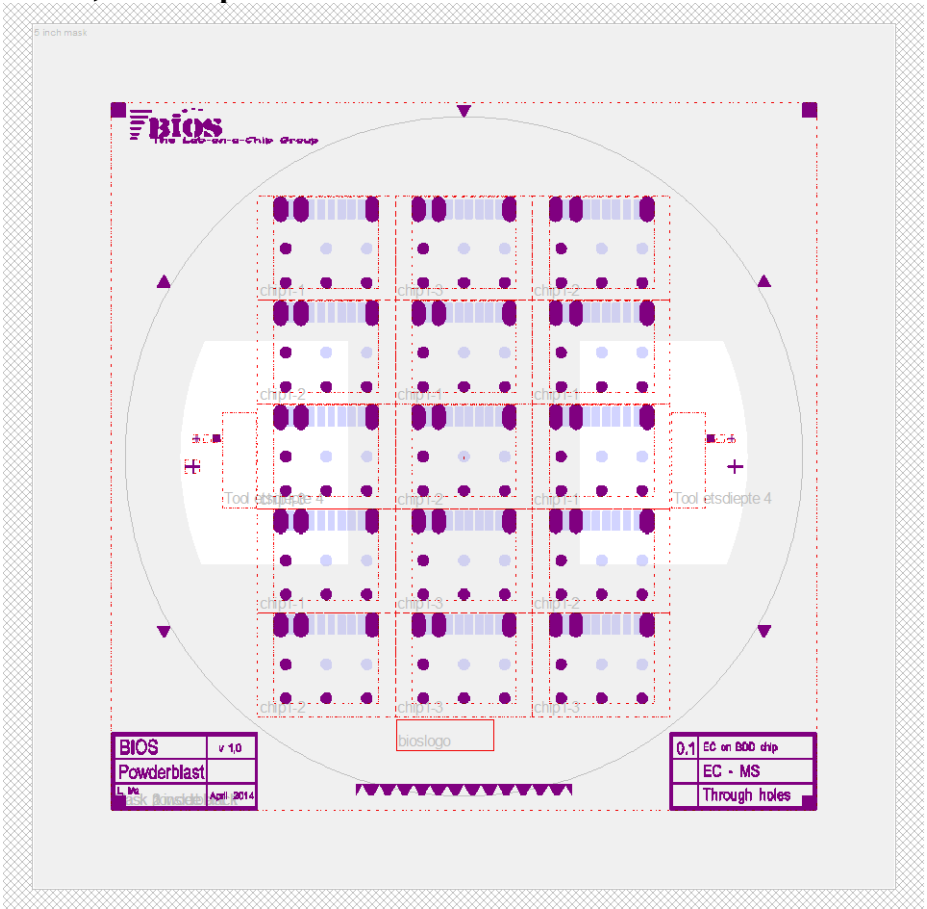

Figure 9: Mask powderblast 1; through holes.

position	description	code	layer	inside white / black
Mask 1	BDD Electrode layer etching from topside	BE	12	black
Mask 2	Bottom channel layer	BC	11	black
Mask 3	Top channel layer	TC	8	black-mirror
Mask 5	Inlets, outlets and contact pads through holes	PB	21	black
Mask 4	Contact pads for BDD wafer	CP	13	black

C.3 Process parameters

Top wafer: Borofloat33 (1100um)
Bottom wafer: Boron-doped diamond on insulator-Si
Borofloat33 (550um)

TOP glass wafer+glass channel

Step	Process		Comment
1	**Substrate Borofloat BF33** (#subs107)	Not standard available! info Jan v. NieuwKasteele Supplier: Schott Glas www.schott.com/borofloat • Type: Borofloat 33 • C.T.E.: 3.25 X 10^{-6} K^{-1} • Tglass: 525°C • T anneal: 560°C • Tsoftening: 820 °C • Diameter: 100.0 mm ± 0.5 mm • Thickness: 1.1mm • Etch rate HF 25%: 1µm/min • Etch rate BHF (1:7): 20-25 nm/min • Etch rate HF 1%: 8.6 nm/min • Smoo h side: second flat on the left side	1100um thickness
2	**Clean HNO3 1**	NL-CLR-WB16 • Beaker 1: HNO_3 (99%) 2min	
3	**Quick Dump Rinse (QDR)** (#clean119)	NL-CLR-Wet benches Recipe 1 QDR: 2 cycles of steps 1 till 3, 1- fill bath 15 sec 2- spray dump 15 sec 3- spray-fill 40 sec 4- end fill 500 sec Recipe 2 cascade rinsing: continuous flow Rinse till the DI resistivity is > 10 ΩM	
4	**Clean in KOH**	NL-CLR-WB17 25% KOH @75℃ dip: 10sec	
5	**Ultrasonic clean**	NL-CLR-WB16 Ultrasonic in the rinse water beaker: 10min	

6	**Quick Dump Rinse (QDR)** (#clean119)	NL-CLR-Wet benches Recipe 1 QDR: 2 cycles of steps 1 till 3, 1- fill bath 15 sec 2- spray dump 15 sec 3- spray-fill 40 sec 4- end fill 500 sec Recipe 2 cascade rinsing: continuous flow Rinse till the DI resistivity is > 10 ΩM	
	Clean in HNO3	NL-CLR-WB16 Beaker 1: HNO3(99%) 1min Beaker 2:HNO3(99%) 2min	
4	**Substrate drying** (#clean120)	NL-CLR-WB Single wafer dryer • speed: 2500 rpm, 60 sec with 30 sec N_2 flow	
5	**Dehydration bake** (#lith102)	NL-CLR-WB21/22 dehydration bake at hotplate • temp. 120°C • time: 5min	Continue immediately with priming the step!
6	**Priming (liquid)** (#lith101)	NL-CLR-WB21/22 Primer: HexaMethylDiSilazane (HMDS) use spincoater: • program: 4000 (4000rpm, 30sec)	
7	**Lithography - Coating Ti-35 XR**	NL-CLR-WB21 **Procedure for 3.5 µm thickness** • dehydration bake: 10 min @120℃ • priming HMDS: 30 sec 4000RPM • coating: Ti35 ES: 3000rpm, 30sec • prebake: hotplate 95°C, 120sec • Exposure parameters: 12sec, hard contact •stabilisation step: room temp.>10 min • reversal bake: 120°C; (3 min) • Flood exposure: Hg lamp/intensity: 12mW/cm^2; 40 sec, *Flood exposure should be carried out without a mask in the mask aligner* • development: OPD 4262, beaker 1:10 sec, beaker 2: 10sec • quick dump rinse, DI, <0.1µS • spin drying • visual microscopic inspection	
12	**Postbake Ti-35 resist** (#lith109)	NL-CLR-WB21 postbake: Hotplate • temp 120°C • time 30min	
14	**Plasma etching of glass**	NL-CLR- Adixon-DE **Program: BFloat Exp 9** • Alumnium electrode	RIE of borofloat33 1100um(81%SiO2, 13%B2O3):

		• Electrode temp.: 20°C • **CHF3: 25 sccm ???** • **02: 5 sccm** • pressure: 20 mTorr • Power: 350 Watt **Mask: Ti-35 XR: 130 nm/min** **BF 33: 500 nm/min(theoretically)** **350-380 nm/min(reality)**	Recipe:SF6/CHF3+O2? Mask:Ti-35 Etch time: 14min Make sure about the recipe and etch rate
16	**Surface profile measurement** (#metro105)	NL-CLR-VeecoDektak 8	
	Cleaning piranha (#clean117)	NL-CLR-WB09 Applications: • For direct wafer bonding use always a fresh solution. • For polymer stripping it is allowed to use "aged" solutions and can be re-used by adding H_2O_2 if necessary. Mixture: H_2SO_4 :H_2O_2 (3:1) vol% • fill beaker with H_2SO_4 • **add slowly H_2O_2 and avoid a temperature rise above 100°C** • adjust hotplate at 85 °C • start heating of hotplate • start cleaning (load wafers) when **solution** temperature is between 85-90°C • cleaning time 15min	
17	**Lamination of BF 410 foil** (#lith145)	NL-CLR-GBC 3500 PRO Laminator Ordyl BF 410 dry resist foil Laminate BF 410 foil on back side • Put two foil layer on back side of the wafer • Remove the protection layer from BF 410 foil • Apply BF 410 foil with roller • Protect carry-paper with plain A4 paper • Put the wafer together with foils and papers into the laminator • Temp: 75 °C (´carry ´preset)??? • Speed: 2 (´carry ´preset) • Remove and cool down wafer • Cut the wafer out of foil	**Double layer** Don't forget to remove the protection layer of first foil
18	**Alignment and exposure BF410** (#lith135)	NL-CLR-EVG 20 Electronic Vision Group 20 Mask Aligner • Hg-lamp: 12 W.cm2 • Exposure time: 20 sec (BF 410) Remark: DSP alignment with foil on both sides • Remove the foil with a "knife" to achieve a clear view of the aligning marks • After development proctect the aligning mask with tape again!	use bottom side, crosshair, soft contact, 40 um separation, 1mm thickness, continuous;

		Protect the side with channels with tape	
19	**Development BF410 foil** (#lith136)	Carre-Bios-ChemistryLab Na_2CO_3: MERCK 1.06392.0500 Na_2CO_3:H_2O = 15g : 7.5liters (+ 1 cup Antifoam) • Temp: 32°C???? • Time: 3min???? Due to non-uniform development turn sample by 180° after half the time - small features might need longer development time	?????
20	**Development BF410 foil**	Carre-Bios-ChemistryLab Rinse with warm tap water to remove the foil above the powderblast holes;????T Rinse with DI water	
21	**Substrate drying** (#clean120)	NL-CLR-WB Single wafer dryer • speed: 2500 rpm, 60 sec with 30 sec N_2 flow	
22	**Powderblasting of glass** (#etch120)	NL-Carre-BIOS Powderblaster For feature size >100µm • Particles: 30µm Al_2O_3 • Pressure: 4.6bar • Massflow: 3-12 g/min • Etch rate appr. 91µm per g/cm^2	Pressure 5bar Mass flow 0.4g/s???
23	**Removal of foil and particles after powderblasting**(#clean139)	**Outside cleanroom - use own facility** Start with removal of foil • remove dicing foil manually • remove powderblast foil manually • rinse wafer with water (by spraying) to remove powderblast particles • strip foil in Na2CO3[1] solution @hotplate T????, time >30 min • rinse wafer with water time > few minutes • **ultrasonic cleaning** in water, time >10 min • drying of substrate by spinning or N2 gun	Cleaning @Bios; Ultrasonic cleaning @Cleanroom
25	**Quick Dump Rinse (QDR)** (#clean119)	NL-CLR-Wet benches Recipe 1 QDR: 2 cycles of steps 1 till 3, 1- fill bath 15 sec 2- spray dump 15 sec 3- spray-fill 40 sec 4- end fill 500 sec Recipe 2 cascade rinsing: continuous flow Rinse till the DI resistivity is > 10 ΩM	

Bottom wafer

BDD wafer+ SU8 channel

Step	Process		Comment
1	BDD wafer:0.5mm Si +200nm SiO2 +700nm Si3N4 +450-500nm BDD		
2	**CleanHNO3-1** (#clean102)	NL-CLR-WB14 • beaker 1: HNO_3 (99%) 5min	Standard wafer cleaning
3	**Clean HN03-2** (#clean138)	NL-CLR-WB14 • beaker 2 : HNO_3 (99%) 5min	
4	**Quick Dump Rinse (QDR)** (#clean119)	NL-CLR-Wet benches Recipe 1 QDR: 2 cycles of steps 1 till 3, 1- fill bath 15 sec 2- spray dump 15 sec 3- spray-fill 40 sec 4- end fill 500 sec Recipe 2 cascade rinsing: continuous flow Rinse till the DI resistivity is > 10 ΩM	
5	**Substrate drying** (#clean120)	NL-CLR-WB Single wafer dryer • speed: 2500 rpm, 60 sec with 30 sec N_2 flow	
6	**Dehydration bake** (#lith102)	NL-CLR-WB21/22 dehydration bake at hotplate • temp. 120°C • time: 5min	Continue immediately with priming the step!
7	**Coating Olin Oir 907-17 / or 35** (#lith105)	NL-CLR-WB21 Coating: Primus spinner • olinoir 907-17 • spin Program: 4000 (4000rpm, 30sec) Prebake: hotplate • time 90 sec • temp 95 °C	Time=120s for 35 positive resist
8	**Alignment & Exposure Olin OiR 907-17/or 35** (#lith121)	NL-CLR- EV620 Electronic Vision Group EV620 Mask Aligner • Hg-lamp: 12 mW/cm ^{2} • Exposure Time: 4sec	Exposure time=9s for 35 positive resist
9	**Development Olin OiRresist** (#lith111)	NL-CLR-WB21 After exposurebBake : hotplate • time 60sec • temp 120°C development: developer: OPD4262 • time: 30sec in beaker 1 • time: 15-30sec in beaker 2	
10	**Quick Dump Rinse (QDR)** (#clean119)	NL-CLR-Wet benches Recipe 1 QDR: 2 cycles of steps 1 till 3, 1- fill bath 15 sec 2- spray dump 15 sec 3- spray-fill 40 sec 4- end fill 500 sec Recipe 2 cascade rinsing: continuous flow	

		Rinse till the DI resistivity is > 10 ΩM	
11	**Substratedrying** (#clean120)	NL-CLR-WB Single wafer dryer • speed: 2500 rpm, 60 sec with 30 sec N_2 flow	
12	**Postbake Olin OiR resist** (#lith109)	NL-CLR-WB21 postbake: Hotplate • temp 120°C • time 10min	
13	**Inspection by optical microscope**	NL-CLR	
14	**RIE of BDD+ low power RIE**	NL-CLR-Tetske/Adixon Dirty chamber +Styros electrode **Mask: Olin 907-17 or 907-35** • Electrode temp.: 10°C • **O_2 flow: 50sccm; N_2 flow:20sccm; CHF_3 flow=2 sccm** • pressure: 100mTorr • power: 50 W • Load/Tune: 34/52, Vdc 375 Volt **Etchrate of BDD = 650?nm/min (4");Si_3N_4=?; Resist=?** **Low power RIE: 25w, 100mTorr, 20sec**	Etchrate=? Extra low power RIE step to remove top layer residues of photoresist
15	**Clean HN03-1** (#clean144)	NL-CLR-WB06 • Use only beaker 1 for stripping resist • HNO3 (99%) • time: >10 min or 100% removal of PR	
16	**Quick Dump Rinse (QDR)** (#clean119)	NL-CLR-Wet benches Recipe 1 QDR: 2 cycles of steps 1 till 3, 1- fill bath 15 sec 2- spray dump 15 sec 3- spray-fill 40 sec 4- end fill 500 sec Recipe 2 cascade rinsing: continuous flow Rinse till the DI resistivity is > 10 ΩM	
17	**Etching in 1% HF** (#etch192)multipurpose use dedicated beaker HF 1% • temp.: 20 °C. • time: depends on application	NL-CLR-WB16	
18	**Quick Dump Rinse (QDR)** (#clean119)	NL-CLR-Wet benches Recipe 1 QDR: 2 cycles of steps 1 till 3, 1- fill bath 15 sec 2- spray dump 15 sec 3- spray-fill 40 sec 4- end fill 500 sec Recipe 2 cascade rinsing: continuous flow Rinse till the DI resistivity is > 10 ΩM	
19	**CleanHNO3-1** (#clean102)	NL-CLR-WB14 • beaker 1: HNO_3 (99%) 5min	
20	**Clean HN03-2**	NL-CLR-WB14	

	(#clean138)	• beaker 2 : HNO_3 (99%) 5min	
21	**Clean HNO3-3a/b** (#clean 118)	NL-CR-WB14 beaker 3a/b: HNO_3 (69%), • temp 95°C, • time > 10min	Remove boron residues? Ask Marion
22	**Quick Dump Rinse (QDR)** (#clean119)	NL-CLR-Wet benches Recipe 1 QDR: 2 cycles of steps 1 till 3, 1- fill bath 15 sec 2- spray dump 15 sec 3- spray-fill 40 sec 4- end fill 500 sec Recipe 2 cascade rinsing: continuous flow Rinse till the DI resistivity is > 10 ΩM	
23	**Substratedrying** (#clean120)	NL-CLR-WB Single wafer dryer • speed: 2500 rpm, 60 sec with 30 sec N_2 flow	
24	**Dehydrationbake SU-8** (#lith162)	NL-CLR-WB24 Dehydrationbake •Hotplate: temp 120°C, 10min	20C, 20min; cool down wafer before spining
25	**Coating SU8-5** (#lith163)	NL-CLR-WB24 • SüssMicroTec Spinner Delta 20 • Microchem NANO SU8- 5 • Manufacturer Specs: program: 5 — Thickness (μm): 5.2	Thickness: 5um; program 5(3000rpm)
26	**Softbake SU-8 5** (#lith164)	NL-CLR-WB24 • Hotplate • For spin programs 4-7 • start @ 25 °C • 1 min @ 50 °C • 1 min @ 65 °C • 3 min @ 95 °C • 5°C/2min ramp down to 25°C	
27	**Alignment& Exposure SU-8 5** (#lith165)	NL-CLR-EVG 620 Electronic Vision Group 620 Mask Aligner • Exposure time 10sec	
28	**Post exposure bake SU-8 5** (#lith166)	NL-CLR-WB24 • Hotplate • For spin program 4-7: • Start @ 25 °C • 1 min @ 50 °C • 1 min @ 65 °C • 2 min @ 80 °C • 5°C/2min down to 25°C	
29	**Development SU-8 5** (#lith167)	NL-CLR-WB 24 • TCO Spray Developer • Developer: PGMEA (RER600, ARCH Chemicals)	300s, 3 cycles

		• Time 3:30 min with spray-gun • Rinse with RER600 • Rinse with IPA • Spin dry • Check result and perform extra cycles if not complete	

Glass wafer+ SU8 channel +Pt electrodes

Step	Process		Comment
1	**Substrate Borofloat BF33- 500** µm (#subs114)	**NL-CLR-Cupboard cleanroom** Supplier: Schott Glas: www.schott.com/borofloat • Type: Borofloat 33 • C.T.E.: 3.25 X 10^{-6} K^{-1} • Tglass: 525°C • T anneal: 560°C • Tsoftening: 820 °C • Diameter: 100.0 mm ± 0.3 mm • Thickness: 0.5 mm ± 0.025 mm • Roughness: < 1.0 nm • TTV: < 5 µm • Surface: DSP • Edge: C-edge • Flat: 32.5 mm (Semi) • Sec. Flat: 18 mm (acc to SEMI) • Price 40 euro • Etch rate HF 25%: 1µm/min • Etch rate BHF (1:7): 20-25 nm/min • Etchrate HF 1%: 8.6 nm/min	
2	**CleanHNO3-1** (#clean102)	NL-CLR-WB16 • beaker 1: HNO_3 (99%) 5min	
3	**Clean HN03-2** (#clean138)	NL-CLR-WB16 • beaker 2 : HNO_3 (99%) 5min	
4	**Quick Dump Rinse (QDR)** (#clean119)	NL-CLR-Wet benches Recipe 1 QDR: 2 cycles of steps 1 till 3, 1- fill bath 15 sec 2- spray dump 15 sec 3- spray-fill 40 sec 4- end fill 500 sec Recipe 2 cascade rinsing: continuous flow Rinse till the DI resistivity is > 10 ΩM	
5	**Substrate drying** (#clean120)	NL-CLR-WB Single wafer dryer • speed: 2500 rpm, 60 sec with 30 sec N_2 flow	
6	**Lithography-Olin908-Ti 35 XR**	NL-CLR-WB21 Applications e.g. Lift off of Ti, Pt **Procedure for 3.5 µm thickness** • dehydration bake: 10 min • priming HMDS: 30 sec • coating: Ti35 ES: 4000rpm, 30sec	

		• prebake: hotplate 95°C, 120sec • Exposure parameters: 23sec •stabilisation step: room temp.>10 min • reversal bake: 120°C; (120sec) • Flood exposure: Hg lamp/intensity: 12mW/cm^2; 60 sec, *Flood exposure should be carried out without a mask in the mask aligner* • development: OPD 4262, 120*s* • quick dump rinse, DI, <0.1μS • spin drying • visual microscopic inspection	
7	**Inspection by optical microscope**	NL-CLR	
8	**Cleaning by UV/Ozone** (#clean109)	NL-CLR-UV PRS 100 reactor -To improve wetting for wet chemical etching of chromium and oxide layers coated with olinoir resist. -To remove resist residues Time: variable	5 min
9	**Etching glass BHF (1:7)** (#etch125)	NL-CLR-WB9 or 10 Use private beaker with BHF (1:7) • temp.: 20°C Etchrates: •thermal SiO2: 60-80nm/min • PECVD Si02: 125/nm/min • TEOS SiO2: 180/nm/min • TEOS **H3 (new):** 242 nm/min • Pyrex #7740: 20nm/min • **Borofloat BF33: 20-25 nm/min** • Si3N4-H2: 0.64 nm/min	150nmdeep 6 min
10	**Quick Dump Rinse (QDR)** (#clean119)	NL-CLR-Wet benches Recipe 1 QDR: 2 cycles of steps 1 till 3, 1- fill bath 15 sec 2- spray dump 15 sec 3- spray-fill 40 sec 4- end fill 500 sec Recipe 2 cascade rinsing: continuous flow Rinse till the DI resistivity is > 10 ΩM	
11	**Substrate drying** (#clean120)	NL-CLR-WB Single wafer dryer • speed: 2500 rpm, 60 sec with 30 sec N_2 flow	Remove foil afterwards
12	**Cleaning by UV/Ozone** (#clean109)	NL-CLR-UV PRS 100 reactor -To improve wetting for wet chemical etching of chromium and oxide layers coated with olinoir resist. -To remove resist residues Time: variable	5min
13	**Sputtering of Ti** (#film116)	**NL-CLR-Eq.Nr. 37 / Sputterke** Ta Target (gun #: see mis logbook) • use Ar flow to adjust sputter pressure • Base pressure: < 1.0 e-6mbar	Pre-sputter time=1min, deposition

		• Sputter pressure: 6.6 e-3mbar • power: 200W • Deposition rate = 13 nm/min	time=47sec, layer thickness=10nm (try on dummy wafer first)
14	**Sputtering of Pt** (#film118)	NL-CLR-nr. 37 / Sputterke Pt Target (gun #: see mis logbook) • use Ar flow to adjust sputter pressure • base pressure: < 1.0 e-6mbar • sputter pressure: 6.6 e-3mbar • power: 200W deposition rate = 22-27 nm/min	pre-sputter time=1min, deposition time=around 5min (try on dummy wafer)
15	**Lithography - Lift-off procedure for metals** (#Lith144)	NL-CLR- Wet-Bench 11 Use metal beaker and wafer holder • Beaker 1: Aceton technical, > 10 min • Beaker 2: Aceton VLSI , >10 min • Beaker 3: Isopropanol VLSI > 10min • Spin drying	Soak in aceton for 1 hour without ultrasonic
16	The same as step 15-29 in Pt chip fabrication		

Glass-SU8 bonding

Step	Process		Comment
1	**Clean HNO3 1&2** (#clean105)	NL-CLR-WB16 • Beaker 1: HNO_3 (99%) 5min • Beaker 2: HNO_3 (99%) 5min	glass wafer cleaning before bonding
2	**Quick Dump Rinse (QDR)** (#clean119)	NL-CLR-Wet benches Recipe 1 QDR: 2 cycles of steps 1 till 3, 1- fill bath 15 sec 2- spray dump 15 sec 3- spray-fill 40 sec 4- end fill 500 sec Recipe 2 cascade rinsing: continuous flow Rinse till the DI resistivity is > 10 ΩM	
3	**Substrate transport in DI between WB** (#clean141)	NL-CLR-Wet benches Substrate transport in beaker with Demiwater • use always waferholder of next step/wet bench for transport !	
4	**Etching in KOH standard** (#etch138)	NL-CLR-WB17 use dedicated beaker 1 or 2 • 25wt% KOH (standard recipe) • temp.: 75°C • use stirrer Etchrates: Si <100> = 1µm/min Si <111> = 12.5nm/min SiO2 (thermal) = 180nm/hr	time 10 sec

	SiRN< 0.6nm/hr (LPCVD ??)	
5	**Clean HNO3 1&2** **NL-CLR-WB 16** • Beaker 1: HNO_3 (99%) **1min** • Beaker 2: HNO_3 (99%) **4min**	
6	**Quick Dump Rinse (QDR)** (#clean119) NL-CLR-Wet benches Recipe 1 QDR: 2 cycles of steps 1 till 3, 1- fill bath 15 sec 2- spray dump 15 sec 3- spray-fill 40 sec 4- end fill 500 sec Recipe 2 cascade rinsing: continuous flow Rinse till the DI resistivity is > 10 ΩM	
7	**Substratedrying** (#clean120) NL-CLR-WB Single wafer dryer • speed: 2500 rpm, 60 sec with 30 sec N_2 flow	
8	**Dehydrationbake** (#lith102) NL-CLR-WB21/22 dehydration bake at hotplate • temp. 120°C • time: 5min	20min Cooling down beforebonding???
9	**EV620 Aligning&Prebonding**(#bond104) NL-CLR-EV620 mask aligner Program: xxxxx • SDB Direct Bond tool 4" • Bond chuck SDB • Substrate1 4" • Substrate2 4" • Separation 30 µm • No exposure • SDB Piston • Bond time 60 sec Instructions: • Align alignmarks of of top wafer to crosshairs • Check prebonding by using IR-setup	SU8 to glass
	EV501 Anodic bonding (#bond105) NL-CLR-EVG /EV501 bond tool • Temperature 400°C • Vacuum better then 10^{-1} mbar • High voltage 1000 Volt • Pressure 300 N • Total process time 2 hours • First wafer Silicon • Second wafer Pyrex/Borofloat glass • Alignment can be done with EV620 maskaligner	
10	**Adhesive bonding:** pressure=2-2.5MPa;Temperature=180C;Bonding time=1h;	Obducat 1.Anodicbonding --Anodic bonder EV 501; 2.Press
11	Inspection of bonding area and bonding strength	